



Centro Brasileiro de Pesquisas Físicas
(Brazilian Center for Research in Physics)

DOCTORAL DISSERTATION

**Manganese Oxide Films on Au(111):
Growth and Surface Characterization**

Author: Jade Barreto

Advisor: Prof. Dr. Fernando Loureiro Stavale Junior

Rio de Janeiro, Brazil

July, 2022



Centro Brasileiro de Pesquisas Físicas
(Brazilian Center for Research in Physics)

DOCTORAL DISSERTATION

Manganese Oxide Films on Au(111): Growth and Surface Characterization

Thesis presented at the Brazilian Center for Research in Physics (CBPF), in partial fulfillment of the requirement for the degree of doctor, under adviser of Prof. Dr. Fernando Loureiro Stavale Junior.

Author: Jade Barreto

Advisor: Prof. Dr. Fernando Loureiro Stavale Junior

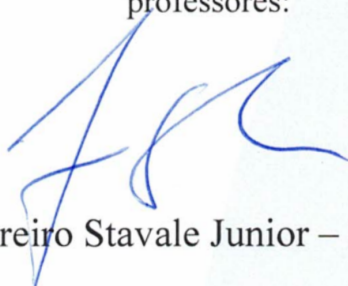
Rio de Janeiro, Brazil

July, 2022

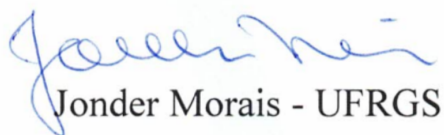
“MANGANESE OXIDE FILMS ON Au (111) GROWTH AND SURFACE CHARACTERIZATION”

JADE BARRETO

Tese de Doutorado em Física apresentada no
Centro Brasileiro de Pesquisas Físicas do
Ministério da Ciência Tecnologia e Inovação.
Fazendo parte da banca examinadora os seguintes
professores:



Fernando Loureiro Stavale Junior – Orientador/CBPF



Jonder Moraes - UFRGS



Maria Luiza Rocco Duarte Pereira - UFRJ



Fabio Souza Toniolo - UFRJ



Eduardo Matzenbacher Bittar - CBPF

As flores resistem à tempestade
E cantam por becos, esgotos e bares
As flores resistem à tempestade
E cantam por becos, esgotos e bares

*Nada Conterá a Primavera
de Francisco, el Hombre*

Acknowledgment

Português

Gostaria de agradecer sinceramente todos os meus familiares, começando pelos meus pais: Nilza e Adelmo Barreto. Ambos sempre me apoiaram demonstrando grande orgulho a cada etapa vencida na acadêmia. Minhas irmãs, Janine e Jessica Barreto, que sempre estiveram do meu lado mesmo que geograficamente distantes. Aos meus tios, Regina e Nei Covas, que sempre me receberam com carinho. As minhas primas Silvia, Cintia e Gabriela Covas e aos primos Vini. e Rick. Ao Xodó, o gato da família que esteve do meu lado (ou em cima do teclado) enquanto eu escrevia esta tese.

Ao Prof. Dr. Fernando Stavale pela orientação e dedicação, por ter me aceitado para o mestrado e tido paciência de me ouvir até aqui. O meu amadurecimento como profissional e também como pessoa se deve as várias criticas, conversa e passeios que tivemos durante esses seis anos. A Prof. Dr. Camilla Codeço, pelos seus conselhos e criticas sobre esta tese, agradeço de coração.

Aos meus queridos amigos do Paraná, são tantos que se eu for tentar nomear vou acabar sendo injusta com alguém. E aos amigos do Rio de Janeiro, que embora também sejam muitos é difícil não citar o Pablo e Maria, Miguel e Luci, Eri, Jô, Dani, Grecia e Cintia.

Aos colegas de laboratório do CBPF, que tiveram paciência e compreensão em cada dia difícil no laboratório. Em especial ao Rub. pelas imagens de STM e conselhos como um amigo mais velho, muito obrigada. E também a Maria I. Ramos do INMETRO, pelas imagens de STEM fornecida.

Agradeço as instalações do Centro Brasileiro de Pesquisas Físicas – CBPF, e as pessoas que fazem o CBPF. A disponibilização dos laboratórios e equipamentos fornecida pelo Laboratório de Superfícies (LabSurf) através do Prof. Dr. Alexandre Mello de Paula Silva.

Por fim, gostaria de agradecer a bolsa de pesquisa que me foi concedida pelo Conselho Nacional de Desenvolvimento Científico e Tecnológico - CNPq. O mundo em que vivemos hoje só é possível graças à ciência, e é ela quem nos levará ao futuro.

English

I thank Prof. Dr. Jörg Libuda (FAU) for kindly accepting me into your research group. Even for a short time, it was special, and part of this thesis is thanks to all of you. The collaboration was wonderful, and all the group people were so lovely to me, so thank you very much. I want to mention Georg and Chantal both collaborated with me in the laboratory which made the days amazing.

I thank Prof. Dr. Paul Bagus (UNT) for providing the theoretical calculations. Thank you for being kind in all our virtual meetings, which greatly improved this thesis.

I kindly thank Dr. Shamil Shaikhutdinov and Prof. Dr. Hans-Joachim Freund for collaborating and providing the laboratory in FHI.

Abstract

Manganese oxide thin films present Mn cations that may take different valence states and structural geometries, exhibiting various properties and applications. Hence, this thesis explores the lattice and electronic structure and the chemical reactivity of MnO and Mn₃O₄ thin films grown onto Au(111) single-crystal. First, the surface lattice structure was determined by Low-Energy Electron Diffraction (LEED) with the support of microscopy techniques. Therefore, we observe that both films have grown at [001] direction and present three domains rotated by 60°. Next, the X-ray Photoelectron Spectroscopy (XPS) spectra were measured to study the surface electronic structure. For that, we fit the high-resolution Mn 2p spectra under the multiplet splitting theory, where the collaborator Professor Paul Bagus performed the calculations of multiplets. The Mn 2p fit was analyzed for three distinct MnO films, which were approximated to be thick, thin, and island films. As a result, we could identify the contributions from bulk, terrace, and edge atoms. Then, the XPS fit analyses proved to be an important tool for observing the low-coordinated Mn cations on the surface, which shows an advance in the observation of the core-level binding energy shift effects (CLS). In addition, adsorptions of carbon monoxide (CO) and water (D₂O) molecules yield insights into the film's chemical reactivity. For that, it mainly uses the Infrared Reflection Absorption Spectroscopy (IRAS) technique to observe the interaction of the surface with the molecules. The CO probes the surface termination of Mn₃O₄(001) and shows that its surface termination is oxygen-rich. Both films dissociate the water molecule into O_wD and O_sD, where the *w* index stands for oxygen from water and the *s* index for oxygen from the surface. However, this water dissociation only occurs in the defects of the oxides. A surface rich in oxygen and the cations at the octahedral sites are known to be unfavorable to dissociating the water.

Key Words: Surface Science, Manganese Oxide, XPS, and IRAS.

Resumo

Filmes de óxido de manganês possuem cátions que podem assumir diferentes estados de valência em estruturas diversas, exibindo assim várias propriedades e aplicações. Por isso essa tese explora a rede cristalina e a estrutura eletrônica assim como a reatividade química dos filmes finos de MnO e Mn₃O₄ crescidos sobre monocristal de Au(111). Primeiro foi determinada a estrutura de rede através da técnica de difração de elétrons de baixa energia (da sigla em inglês *LEED*) e com auxílio de técnicas de microscopias. Dessa forma foi determinado que ambos os filmes crescem na direção cristalográfica [001] e apresentam três domínios rodados de 60° entre si. Depois espectros de fotoelétrons de raios-X (da sigla em inglês *XPS*) foram obtidos para investigar a estrutura eletrônica da superfície. Esse estudo consistiu nas análises dos picos de alta resolução do Mn 2p com o emprego da teoria da separação em multipletos, onde os cálculos teóricos foram realizados pelo colaborador Prof. Paul Bagus da universidade do norte do Texas (da sigla em inglês *UNT*). Para três diferentes filmes de MnO, aproximados para filme espesso, fino e ilha, pudemos identificar os átomos em baixa coordenação identificados como contribuição no espectro de átomos internos, terraço e extremidades. Assim foi realizado um avanço na observação do efeito de deslocamento da energia de ligação em nível de caroço (do acrônimo em inglês *CLS*). Além disso, a reatividade química da superfície dos filmes foram observadas com adsorção de moléculas de água (D₂O) e monóxido de carbono (CO). Para realizar esse estudo a técnica de espectroscopia de absorção e reflexão infravermelha (da sigla em inglês *IRAS*) foi empregada, nela é possível observar a interação das moléculas com a superfície. Os experimentos com as moléculas de CO indicam que a superfície do Mn₃O₄(001) é terminada com os cátions de manganês 3+ rica em oxigênio. Os dois filmes dissociam a água nas contribuições de oxigênio da água com o deutério (O_wD) e oxigênio da superfície com o deutério (O_sD). Porém, a água só dissocia nos defeitos da superfície, superfície rica em oxigênio como a do Mn₃O₄ não irá facilitar a dissociação das moléculas de água.

Palavras-Chaves: Ciência de Superfície, Óxido de Manganês, XPS and IRAS.

Contents

Introduction	14
1 Literature Review	16
1.1 Manganese Oxide Properties	16
1.2 MnO and Mn ₃ O ₄ Thin Films	17
2 Experimental Procedure	19
2.1 Low Energy Electron Diffraction (LEED)	19
2.2 X-Ray Photoelectron Spectroscopy (XPS)	21
2.3 Thermal Desorption Spectroscopy (TDS)	25
2.4 Infrared Reflection Absorption Spectroscopy (IRAS)	28
2.5 UHV Systems	33
2.5.1 Procedures	34
2.5.2 Au(111) Substrate	35
3 Results	38
3.1 Core-level BE Shifts in MnO(001) Thin Films	38
3.1.1 Introduction	38
3.1.2 Results and Discussion	39
3.1.3 Conclusions	48
3.2 Chemical Reactivity of MnO(001) Thin Films	50
3.2.1 Introduction	50
3.2.2 Results and Discussion	50
3.2.3 Conclusions	58
3.3 Probing Surface Structure of Mn ₃ O ₄ (001) Film with CO and D ₂ O Adsorptions	59
3.3.1 Introduction	59
3.3.2 Results and Discussion	59
3.3.3 Conclusions	65
Conclusions	66
A Appendix	68
A.1 Master Thesis Summary	68
A.2 Curriculum	70
Bibliography	73

Abbreviations list

BE	<i>Binding Energy</i>
CBPF	<i>Centro Brasileiro de Pesquisas Físicas</i>
DLD	<i>Delay Line Detector</i>
EBE	<i>Electron Beam Evaporation</i>
FHI	<i>Fritz Haber Institute</i>
FAU	<i>Friedrich Alexander Universität</i>
HSA	<i>Hemispherical Spherical Analyser</i>
IR	<i>InfraRed</i>
IRAS	<i>Infrared Reflection Absorption Spectroscopy</i>
INMETRO	<i>Instituto Nacional de Metrologia, Qualidade e Tecnologia</i>
LEED	<i>Low Energy Electron Diffraction</i>
MBE	<i>Molecular Beam Epitaxy</i>
MCT	<i>Mercury Cadmium Telluride</i>
PES	<i>PhotoElectron Spectroscopy</i>
QMS	<i>Quadrupole Mass Spectrometer</i>
STEM	<i>Scanning Transmission Electron Microscope</i>
STM	<i>Scanning Tunneling Microscopy</i>
TDS	<i>Thermal Desorption Spectroscopy</i>
TPD	<i>Temperature-Programmed Desorption</i>
UHV	<i>Ultra High Vacuum</i>
UNT	<i>University of North Texas</i>
VB	<i>Valence Band</i>
XPS	<i>X-Ray Photoelectron Spectroscopy</i>

List of Figures

1.1	Manganese oxide phase diagram for high temperature, extracted from [33].	16
1.2	Ideal unit cell representation for the MnO and Mn ₃ O ₄ , and the octahedral and tetrahedral coordination sites, performed with VESTA software [34].	17
1.3	XPS Mn 2p spectrum for two angles, 0° and 80°, for the MnO thin film grown onto Ag(100) [adapted from [24]].	18
2.1	Left side is the scheme of the LEED experiment (extracted from [44]) and the right side is the graphical construction of the Ewald sphere (based on [44]).	19
2.2	LEED pattern simulation of a hexagon with 2.88 Å of lattice parameter by side of Au(111) diffraction pattern (46 eV) (extracted from [46]).	20
2.3	Scheme of PES experiment for three different sources (X-Ray, Ultra-Violet, and Synchrotron) that extract the photoelectrons which pass by an energy analyzer until it reaches the electron detector (extracted from [47]).	21
2.4	Relation between the energy levels of a sample and the electron energy distribution observed at spectrum obtained from a light energy of $\hbar\omega$ (extracted from [47]).	22
2.5	Mn 2p theory of multiplets for an MnO ₆ cluster, table inside with the intensities and position of each multiplet of Mn 2p _{3/2} peak (adapted from [32]).	23
2.6	TDS experiment scheme: The temperature of the sample is varied with the time while the quadrupole mass spectrometer (QMS), which is in front of the surface sample, measures the concentration of desorbing species (extracted from [51]).	25
2.7	Coverage-spectra simulation for second-, first- and zero-order performed by Badan (2016). $E = 60kJ/mol$; $\nu = 10^{13}s^{-1}$; coverages of 0.2, 0.4, 0.6, 0.8 and 1.0 ML. Adapted from [52].	26
2.8	Three TDS data of coverage dependence, where the surfaces were previously charged with molecules. (Adapted from [53, 54]).	27
2.9	Representation drawing of vibration normal modes of OH group bonded to a Si atom on a silica lattice framework (adapted from [57]).	28
2.10	The image dipole theory of surface selection rule was drawn (Adapted from [57]).	30
2.11	Representation of incident and reflected IR light by the surface, the phase shift in function of incidence angle ϕ and the surface electrical field (Adapted from [58]).	30
2.12	The total adsorption intensity and the absorption function A obtained from the spectrum. Extracted from [57].	31
2.13	IRAS survey spectra of water on Au(111) substrate.	31

2.14	Example of IRAS setup (adapted from [57])	32
2.15	Photo of SPECS equipment from the Laboratory of Surfaces and Nanostructures (CBPF/Rio de Janeiro) (adapted from [31]).	33
2.16	(a) Picture of the IRAS equipment with others facilities from the laboratory of Structure and Reactivity (FHI/Berlin) (b) Picture of the IRAS equipment with others facilities from the laboratory of Interface Research and Catalysis (FAU/Erlangen)	34
2.17	(a) Diffraction pattern by LEED picture and (b) real lattice representation of Au(111). Spectra (Al K_{α} source) of Au(111) for (c) survey (d) $4f$ and (e) $4p_{1/2}$ peaks.	36
2.18	Procedure to remove the Au $4p_{1/2}$ peak contribution inside of Mn $2p$	37
3.1	(a) LEED image by the side of LEEDpat simulation (b) and the corresponding STM image of the film (1×1) MnO(001). The corresponding (c) LEED image, simulation and (d) STM image of $c(2\times 2)$ MnO(001) film. STM images by Rubem Caetano (CBPF).	39
3.2	(a) STEM image of the thick (1.77 nm) film of (1×1) MnO(100). (b) High-resolution image of film structure (c) and the corresponding LEED. STEM image by Maria Ramos (INMETRO).	40
3.3	Series of LEED pictures for the Au(111) substrate and the surfaces (1×1) -Thick, (1×1) -Thin and $c(2\times 2)$ from the MnO(001) thin film.	41
3.4	MnO(001) atomic-level structure of thick, thin, and island thin films observed with LEED, STEM, and STM techniques.	42
3.5	Two Mn $2p$ spectra, the black dash line is the (1×1) -Thin structure and the green continuous line is the $c(2\times 2)$ -Island reconstruction.	43
3.6	Mn $2p$ multiplet deconvolution for two different surface structure of MnO: (a) (1×1) -Thin and (b) $c(2\times 2)$ -Island.	43
3.7	Mn $2p$ multiplet deconvolution for (a) (1×1) thick film and (b) O $1s$ peak deconvolution for the three films.	44
3.8	Mn $2p$ multiplet fit for the three films with the average BE position.	47
3.9	Mn $2p$ multiplet fit for thick, thin and island films with the corresponding microscopies images.	49
3.10	Coverage-dependence spectra of D_2O on (a) Au(111) surface and (b) MnO(001) thin film.	51
3.11	(a) IRAS spectra showing the temperature effect after D_2O dose on the MnO(001) thin film. (b) Illustration of interpretation with ball-model. (c) TDS measurement for three initial doses on the MnO(001)/Au(111) surface, and one dose on the Au(111) clean surface.	53
3.12	(a) CO Dosing from 0.05 L until 1.4 L. (b) Temperature rise from 100 K until 200 K.	55
3.13	TDS data for two CO exposure on MnO(001) surface.	56
3.14	Co-adsorption of (a) D_2O on CO/MnO. (b) CO on D_2O /MnO.	57
3.15	XPS fitting of Mn $2p$ spectrum and the calculations for the Mn $^{2+}$ and the Mn $^{3+}$ cations (Calculations performed by Prof. Dr. Paul Bagus).	59
3.16	Diffraction pattern (at 40 eV) of Mn $_3$ O $_4$ (001)/Au(111) by the side of the diffraction pattern simulation.	60

3.17	STEM images of two domains from the same Mn_3O_4 film. The first domain is the $\text{Mn}_3\text{O}_4(100)$ without rotation and the second is the plane rotated by 60° , as presented by the ball-models below the two STEM images. STEM images obtained by Maria Ramos (INMETRO), and interpreted by this thesis.	61
3.18	(a) IRAS spectra ($2200\text{ cm}^{-1} - 2000\text{ cm}^{-1}$) of CO coverage from 0.003 L until 49 L and (b) TP-IRAS color plot from 112 K until 200 K with step of 2 K.	62
3.19	TP-IRAS spectra ($2200\text{ cm}^{-1} - 2000\text{ cm}^{-1}$) from 160 K until 185 K of the oxide surface with CO partial pressure of 5×10^{-8} mbar.	63
3.20	(a) D_2O coverage-dependent spectra ($2800\text{ cm}^{-1} - 1800\text{ cm}^{-1}$) from 0.05 L until 10 L of exposure. (b) TP-IRAS ($2750\text{ cm}^{-1} - 2650\text{ cm}^{-1}$) keeping a partial water pressure of 2×10^{-8} mbar, from 165 K until 250 K with 5 K of steps.	64
A.1	The film thickness was determined by TEM image (performed by Prof. Dr. André Luiz Pinto). Interface of Mn on $\text{Mn}_3\text{O}_4(001)$ film of 5 nm onto Au(111).	69
A.2	Thickness calibration by Atomic Force Microscopy (AFM) image (image obtained by the master thesis). (a) Picture of Si sample (b) AFM Image - 20 μm and (c) cross-section.	70

List of Tables

2.1	Values applied to fit the experimental data of MnO spectra (based on [32]).	24
3.1	Fit experimental values of $2p_{3/2}$ and $2p_{1/2}$ peaks. For each film is presented the total area of intern, terrace and edge components.	46
3.2	Fit experimental values of O $1s$ spectra for the thick, thin, and island films.	46
3.3	Fit experimental values of $2p_{3/2}$ peak with the average of BE positions, relative energy and relative intensity ($\pm 10\%$). The area, A, for each multiplet is present, at the end is presented the sum and the core-level shift is presented.	47
A.1	Parameters to perform the Sputtering and Annealing procedures to clean the Au(111) single-crystal.	68
A.2	Manganese oxide films dependence of film thickness and partial oxygen pressure.	69

Introduction

The surface of bulk material is the plane that interacts with other materials, which can be another solid surface, gas molecules, or a liquid. At a determined crystalline direction, the surface atoms can present a reconstruction or relaxation concerning the bulk structure to minimize the surface free energy [1]. As an example, the Au(111) single-crystal presents a complex surface structure regarding the bulk atoms, known as herringbone reconstruction [2]. Such different arrangements of atoms can also occur on a film surface grown on a substrate, as in the case of MnO(111) film grown onto Rh(111), which presents a (2×2) reconstruction [3]. However, the same film on Rh(100) substrate does not reconstruct, presenting a (1×1) structure [4]. Since it is through the surface that interactions with molecules happen, surface structure investigation is essential for applications such as catalysis. Catalysis is the process that enhances the rate of a specific reaction by adding a substance. The substance is a catalyst that does not participate in the products at the end of the reaction [5]. This process is applied in several fields and is present in our daily lives. For example, yeast is a catalyst in the reaction that converts sugar into alcohol in the fermentation process of wine and beer [6, 7].

One approach to catalysis investigation is surface science, which generally employs techniques that operate in ultra-high vacuum (UHV) conditions (pressure below 10^{-9} mbar) [8]. Under this pressure condition, it is possible to perform the surface study at an atomic scale and controlled environment, which facilitates understanding of the chemical process between a surface and molecules. Furthermore, the surface science approach is a model system that can find a good agreement with the same reaction under realistic conditions [9, 10]. As a result, much research focuses on this approach for many surfaces which exhibit an interesting chemical reaction, such as metal oxide semiconductors that present complex structures with distinct metal oxidation states [11, 12]. However, the surface study of these materials is difficult because, generally, conductive samples are necessary to perform the experimental techniques [1]. Due to that, the growth of oxide semiconductors on metallic surfaces to charge compensation is typically employed [13].

Manganese oxide (MnO_x) exhibits a versatile crystalline structure due to its multivalent cation nature, among various metal oxides [12]. Its chemical activity with distinct molecules, such as NO, benzene, and toluene, has been explored in the literature for quite some time [14, 15]. Research on water splitting by MnO_x indicates that its interaction depends on the crystalline structure. The α - MnO_2 exhibits moderate water splitting, while the γ - MnO_2 does not present activity at all. An important factor observed is the metal oxidation state, where the Mn^{3+} plays an important role in this reaction [16]. Another relevant research is the thin films of MnO grown on Au(111), which indicated that the film activates the carbon monoxide (CO) through the edges of the oxide islands [17].

Therefore, film morphology is important for the investigation of chemical reactions. In short, a film can be approximate to form islands or "wet" the substrate surface. For instance, MnO films were grown on Pt(111), where thin films wet the surface and islands are observed for the thick films [18,19]. Manganese oxide film grown onto distinct metallic substrates can result in different morphology and termination structures. For example, the MnO grown on Pd(100) [20] is [111]-oriented and on Au(111) [21] is [100]-oriented. This can be associated, among others, to the lattices mismatches, which can vary from 9.0 % for MnO(110)/Au(110) [22] and for MnO(001)/Ag(001) [23–27] until 21.6 % for Mn₃O₄(110)/Cu(111) [28, 29].

A few studies are found on manganese oxide grown on gold single-crystal; we only know the MnO onto Au(110) [22]. The Au(111) substrate can be an interesting material for the growth of thin films, first because it is known to be very inert, which will avoid oxidation of substrate surface as happened to the Cu(111) substrate [30]. Second, if the film follows the substrate orientation, the MnO(111), which is a polar surface, can be obtained. Moreover, its herringbone reconstruction could influence the film structure due to the substrate surface structure. Therefore, this study begins with the master thesis, where we discover how to grow well-oriented manganese oxide thin films onto Au(111) substrate [31]. In appendix A.1 is presented the master thesis summary, which comprises the growth of MnO(001) and Mn₃O₄(001) thin films.

Therefore, this doctoral thesis proposes detailed research on these films' atomic-level structure and electronic properties by surface science techniques. Further, aim to explore its surface chemical properties as a water and carbon monoxide model system. Then, this thesis is organized with a short manganese oxide literature review in the first chapter; note that more literature review is provided in the introduction of each section in the result chapter. The second chapter explains the techniques employed, mainly the spectroscopies as X-Ray Photoelectron Spectroscopy (XPS) and Infrared Reflection Absorption Spectroscopy (IRAS). Finally, in the third chapter are the results, where the first result extrapolates the core-level binding energy shifts for different cation sites on the surface MnO(001) thin films. A surface comprises many sites such as terraces, edges, vacancies, kinks, steps, and others. Identifying, through the XPS spectra, the amount of low-coordination cations present on a surface material is an advance in investigations of thin films and nanomaterials. The following results comprise the chemical reactivity of the MnO(001) thin film and the Mn₃O₄(001) film for water and carbon monoxide. It aims to understand the surface termination of both films and how their surfaces interact with the gas molecules. This thesis performed the experimental data and its interpretation. It will be indicated in the text when the data and/or its interpretation were performed by someone else.

Chapter 1

Literature Review

1.1 Manganese Oxide Properties

Manganese is a transition metal with the $3d$ orbital half-filled, which has the electronic configuration of $[\text{Ar}]3d^54s^2$. When bonded to oxygen, two electrons from the $4s$ are shared. Where the Mn^{2+} is the cation and O^{2-} is the anion, which is the first oxide state of manganese, MnO , which has a strong ionic character [32]. Manganese oxide has a variety of oxidation states such as MnO (Mn^{2+}), Mn_3O_4 (Mn^{2+} , Mn^{3+}), Mn_2O_3 (Mn^{3+}) and MnO_2 (Mn^{4+}) [12]. Among them, the MnO and Mn_3O_4 are the materials under investigation in this thesis. Besides their interesting properties, these two films are relatively easy to obtain in UHV conditions. Figure 1.1 exhibits a manganese oxide phase diagram, where a determined manganese oxide state is obtained at a range of temperature and oxygen partial pressure. In the UHV chamber, the oxygen partial pressure achievable is from 10^{-9} mbar until 10^{-5} mbar. This range corresponds to -12 atm until -8 atm in the log graphic, in which the MnO and Mn_3O_4 is the manganese oxide phase obtained.

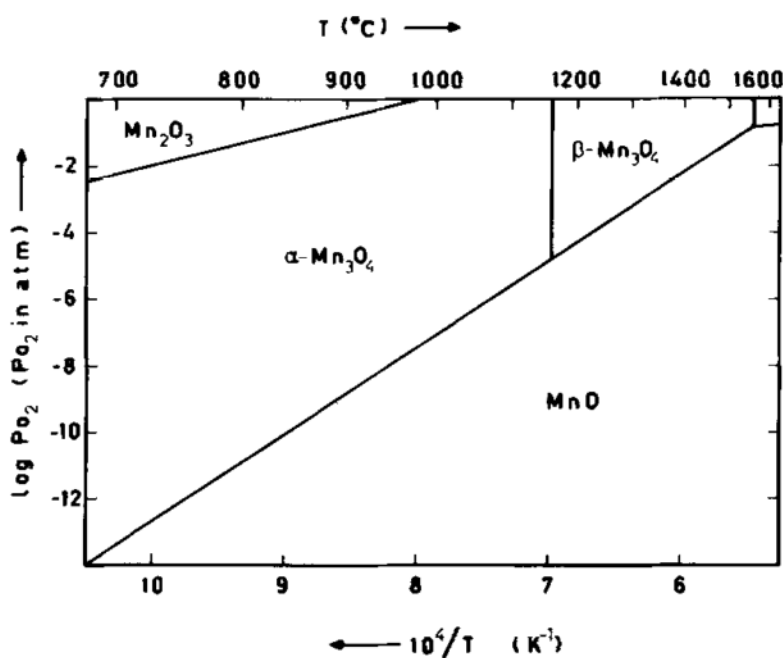


Figure 1.1: Manganese oxide phase diagram for high temperature, extracted from [33].

Figure 1.2 shows the ideal unit cell representation for the MnO and Mn₃O₄, as a ball-model performed with VESTA software [34]. The MnO is a face-centered cubic (rock-salt) with the Mn²⁺ cations at octahedral coordination sites. Its lattice parameter is 4.44 Å with the shorter distance between the cations (Mn-Mn) 3.15 Å [12,35]. This material presents a large bandgap of 3.6 eV with the high-spin antiferromagnetic type-II ordering [36,37]. The Mn₃O₄ presents a more complex structure than the MnO, whose crystalline structure is a tetragonal spinel with a Jahn-Teller effect (a distortion). It presents an edge size of 9.44 Å, where the top and bottom of the unit cell is a square of 5.76 Å distance performed by Mn²⁺ cations [12,35]. This oxide has a mix of cations, with the Mn²⁺ at tetrahedral sites and Mn³⁺ at octahedral sites. Its bandgap is 2.5 eV, which is not as large as the MnO [38].

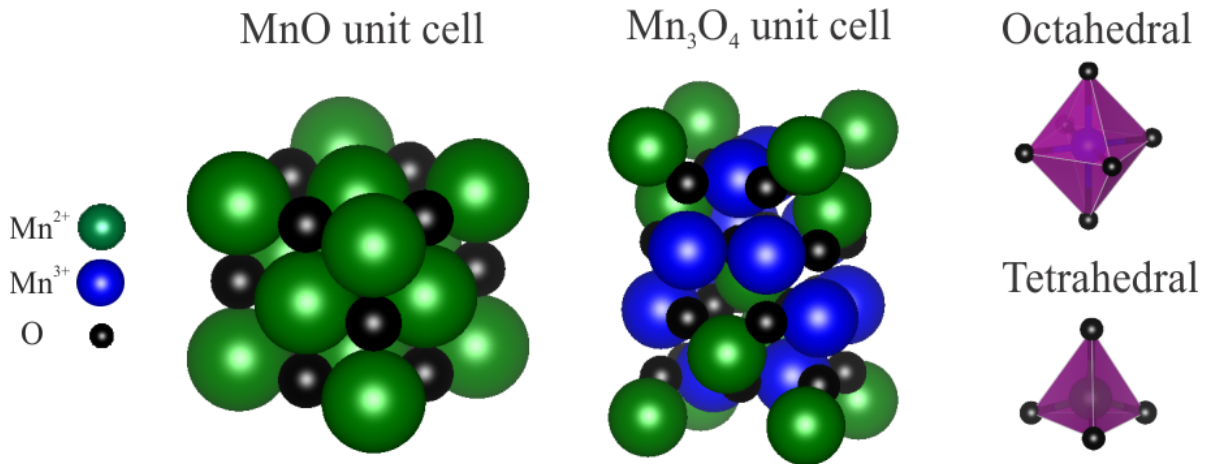


Figure 1.2: Ideal unit cell representation for the MnO and Mn₃O₄, and the octahedral and tetrahedral coordination sites, performed with VESTA software [34].

1.2 MnO and Mn₃O₄ Thin Films

Among the several deposition techniques used to fabricate well-ordered thin films, the molecular beam epitaxy (MBE) is one of the methods to obtain a clean surface in UHV conditions. In the MBE, the material is evaporated from an electrically heated filament or sublimated from a crucible (please see more about the electron-beam evaporator in the section 2.5). Then, the manganese metallic was evaporated onto Au(111) substrate surface in an O₂ environment by MBE technique. Therefore, the film thickness, oxygen partial pressure, and temperature are important parameters. In the literature, several growths of manganese oxide thin films onto metallic substrates by MBE result in the MnO and Mn₃O₄. The film growth can be performed with the substrate at room temperature, avoiding an alloy between the metals. Which is the case for the MnO obtained at Au(110) [22], where an Mn-Au alloy is possible even at room temperature [39]. Therefore, an annealing post-growth is performed to promote film crystallization. The temperature for the post-annealing is limited to the substrate melting point, where the surface can suffer damage with a near temperature.

The MnO thin films show a variety of surface, presenting a (2×2) reconstruction when its grown onto Rh(111) [3], and (1×1) bulk-like when its grown onto Pt(111) [18,19]. In

both cases, the MnO film follows the substrate lattice orientation, but this is not necessarily. The MnO(111) grown onto Rh(100) [4] and present two domains rotated by 90° . In the same substrate, it is possible to obtain a distinct MnO surface, as in the case of the MnO films grown onto Pd(100). Whereby adjusting the parameters, it is possible to obtain the well-ordered MnO(100), the polar MnO(111), and the mix of two surface structures [20].

Many research explored the MnO thin film onto Ag(100) substrate [23–27], in particular, the XPS Mn 2p spectrum has been observed for two different angles, sample surface perpendicular (0°) and with 80° to the analyser (Figure 1.3). It is observed that the peak shape changes from the bulk-sensitive (0°) to the surface-sensitive (80°). The authors do not explore the small change in the Mn 2p line shape, which is found with different asymmetries in the literature. This thesis will be studying the Mn 2p peak shape with the Prof. Bagus theory support (please see the section 2.2).

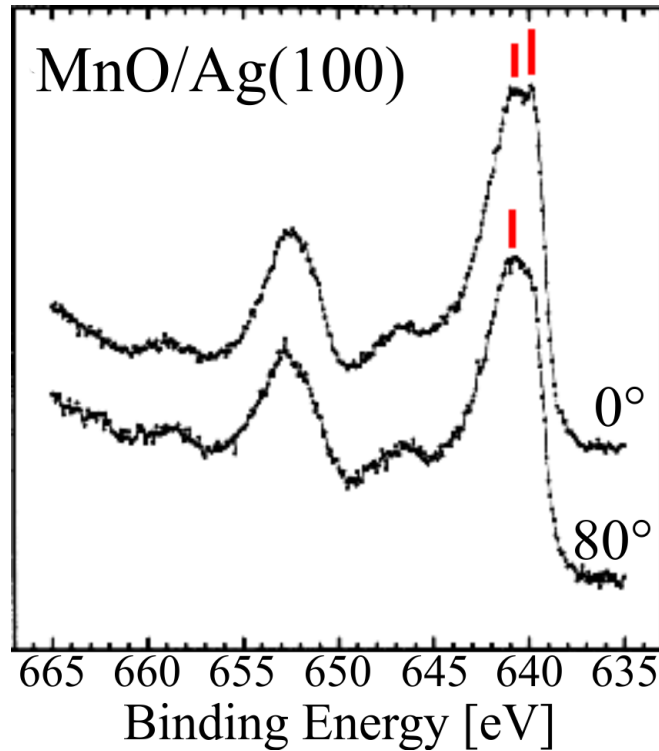


Figure 1.3: XPS Mn 2p spectrum for two angles, 0° and 80° , for the MnO thin film grown onto Ag(100) [adapted from [24]].

Different from MnO, the well-ordered Mn_3O_4 films were grown in a few substrates, such as Ag(001) [40], Cu(111) [28, 29], Pd(100) [41], and Au(111) [21, 42]. Beyond the growth on metallic substrates, it also obtains Mn_3O_4 through the MnO film oxidation [43]. It will be grown onto Au(111) and explored its electronic, lattice structure, and chemical reactivity (section 3.3).

It presented the general literature review for both oxides. Then, in each section of the result chapter, the specific literature review will be introduced, showing the research motivations, results and conclusions.

Chapter 2

Experimental Procedure

2.1 Low Energy Electron Diffraction (LEED)

Figure 2.1 presents the LEED experiment scheme, where an incident beam is scattered by the sample surface (diffracted beam) and results in a diffraction pattern on the screen (behind the electron gun). The sample is grounded, and the LEED apparatus has different lenses to allow the formation of diffraction patterns on the screen. The free mean path determines the electron path length without loss of energy. For many elements, the free mean path is at the minimum of a "universal" curve for low-energy electrons (which is about 10 \AA). Besides that, the electrons do not have a significant penetration on the surface, so the LEED is a surface technique. The incident electron beam can be accelerated from 0 to 300 eV; hence it is low-energy [44].

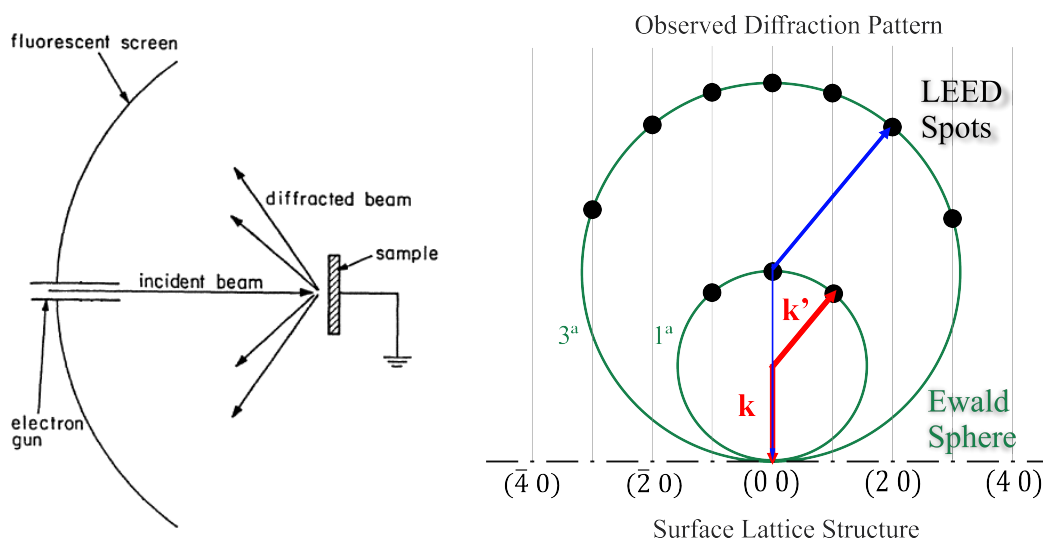


Figure 2.1: Left side is the scheme of the LEED experiment (extracted from [44]) and the right side is the graphical construction of the Ewald sphere (based on [44]).

A crystalline surface is defined by its real and reciprocal lattices. The real lattice is defined by the position of atoms at real space, which the two dimensional position vector is

$$\mathbf{r} = u\mathbf{a}_i + v\mathbf{a}_j, \quad (2.1)$$

where (u, v) are integers and $(\mathbf{a}_i, \mathbf{a}_j)$ are the base vectors. The reciprocal lattice is defined

by the real lattice periodicity at momentum space, which the two dimensional reciprocal lattice vector is

$$\mathbf{g} = h\mathbf{b}_i + k\mathbf{b}_j, \quad (2.2)$$

where (h, k) are integers and $(\mathbf{b}_i, \mathbf{b}_j)$ are the base vectors. Those two vectors must satisfy the following properties

$$\mathbf{a}_i \cdot \mathbf{b}_i = 2\pi, \quad \mathbf{a}_i \cdot \mathbf{b}_j = 0. \quad (2.3)$$

Therefore, the equation 2.3 introduces a relation between the lattice parameters of reciprocal and real spaces.

When electron-beams interact with the sample surface, multiple scattering shall be considered and the scattering beam vector is

$$\mathbf{k}' = \mathbf{k} + \mathbf{g}, \quad (2.4)$$

where \mathbf{k} is the incident beam vector whose module is

$$k = \frac{\sqrt{2mE}}{\hbar}. \quad (2.5)$$

The equation 2.4 is the Bragg law that must be satisfied for the diffracted electron beam to result in a diffraction pattern on the screen. Therefore, the LEED technique scans the reciprocal space of a determined crystalline surface. This can be observed graphically through the Ewald sphere presented in Figure 2.1, on the right side, where the sphere radius is given by the incident vector. Imaginary lines perpendicular to each surface atom are drawn and each spot that the circumference crosses is a diffraction maximum. For an initial electron beam, a few spots are obtained which characterize the first diffraction order. And for a greater electron beam, a bigger sphere is constructed and more orders of diffraction are obtained, as the third order is represented in Figure 2.1 [1, 44].

The diffraction pattern can be reproduced through a simulation by LEEDpat software, developed by Hermann and Van Hove [45]. Where the lattice parameters and angles of real lattice are applied to obtain the correspondent diffraction pattern on the simulation. Although is not unequivocal this can give insights into the crystalline structure. For example, Figure 2.2 shows the Au(111) diffraction pattern by side of the simulation [45, 46].

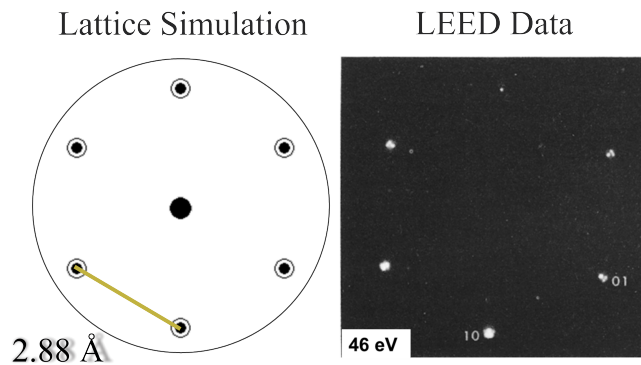


Figure 2.2: LEED pattern simulation of a hexagon with 2.88 Å of lattice parameter by side of Au(111) diffraction pattern (46 eV) (extracted from [46]).

2.2 X-Ray Photoelectron Spectroscopy (XPS)

X-Ray Photoelectron Spectroscopy (XPS) is a technique among others from Photoelectron Spectroscopy (PES). Where a light, in this case, the X-ray, is employed to emit electrons from material to obtain information about the electronic energy distribution. Figure 2.3 schematic of the experiment structure, where different lights (X-Ray, Ultra-Violet, and Synchrotron) extract photoelectrons from the sample that travel through an energy analyzer until it reaches the electron detector. The X-ray source has the energy to excite electrons from the core-level energy of many materials. While the analyzer scans the energies the detector counts the electrons that arrive. Thus, the spectra are composed of the counts of electrons in the function of their binding energy [47].

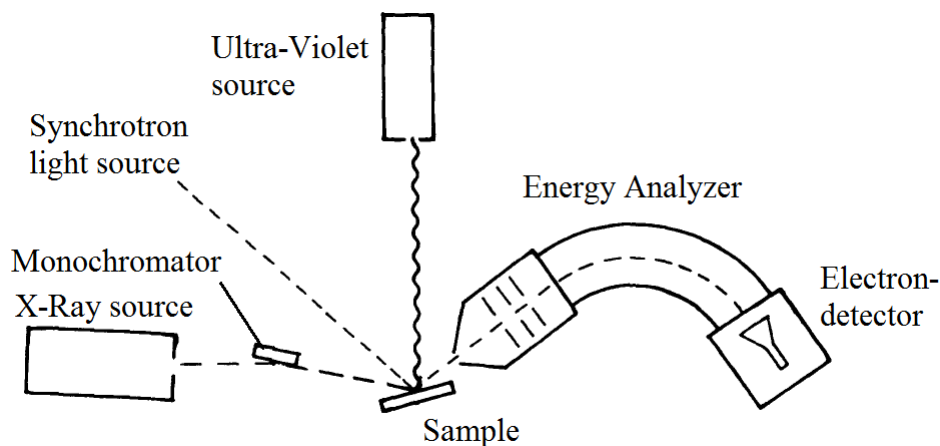


Figure 2.3: Scheme of PES experiment for three different sources (X-Ray, Ultra-Violet, and Synchrotron) that extract the photoelectrons which pass by an energy analyzer until it reaches the electron detector (extracted from [47]).

The binding energy can be obtained by the photoelectric effect equation, which depends on the light energy ($\hbar\omega$), the work function (ϕ) and the electrons kinetic energy (E_{kin}) as a follow:

$$E_B = \hbar\omega - \phi - E_{kin}. \quad (2.6)$$

Work function is the energy necessary to remove an electron from the Fermi level to the vacuum level, this is specific for each material. As the sample is grounded with the equipment the Fermi-level is the same for both, and the equipment work function is previously known through a calibration sample [47].

Several features can be observed on photoelectron spectra, mostly related to the secondary and primary electrons. Whereas the former refers to the electrons that lose energy and contribute to the background, the latter originates the peaks. It also observed the Auger-Meitner peaks, which come from the decay process of excited atoms to go back to the initial state. Metals samples often present the plasmon lines, which occur due to system-hole interaction, the electron-hole pairs can lead to collective oscillations and this is observed as an asymmetric line on the peak. The response of the system to the positive potential performed by the core-hole can lead to satellite peaks, these also can result from the interactions of photoelectron with valence band electrons (known as shake up and

shake off) [47].

The theoretical interpretation of the spectra can be obtained by the three-step model, which describes the experimental situation. This model divides the effect of photoemission into three steps which are: the probability of the photoelectric effect happening; the path of ejected electrons; and the photoelectron escape without losing energy. The evaluation of each step is performed under the *frozen-orbital approximation*, which assumes that the orbitals after and before the photoemission process are the same. Thus, in a first approximation, the peaks on spectra will refer to the orbitals of the determined present element, *i. e.*

$$E_{B,k} \simeq -\varepsilon_k \quad (2.7)$$

often known as a Koopmans' binding energy [47].

The relation between the energy levels of material and the electron energy distribution in the spectrum is performed by the equations 2.6 and 2.7. Figure 2.4 exhibits this relation, where the light energy ($\hbar\omega$) can remove electrons that pass the vacuum level and still has enough kinetic energy to be collected by the spectrometer [47].

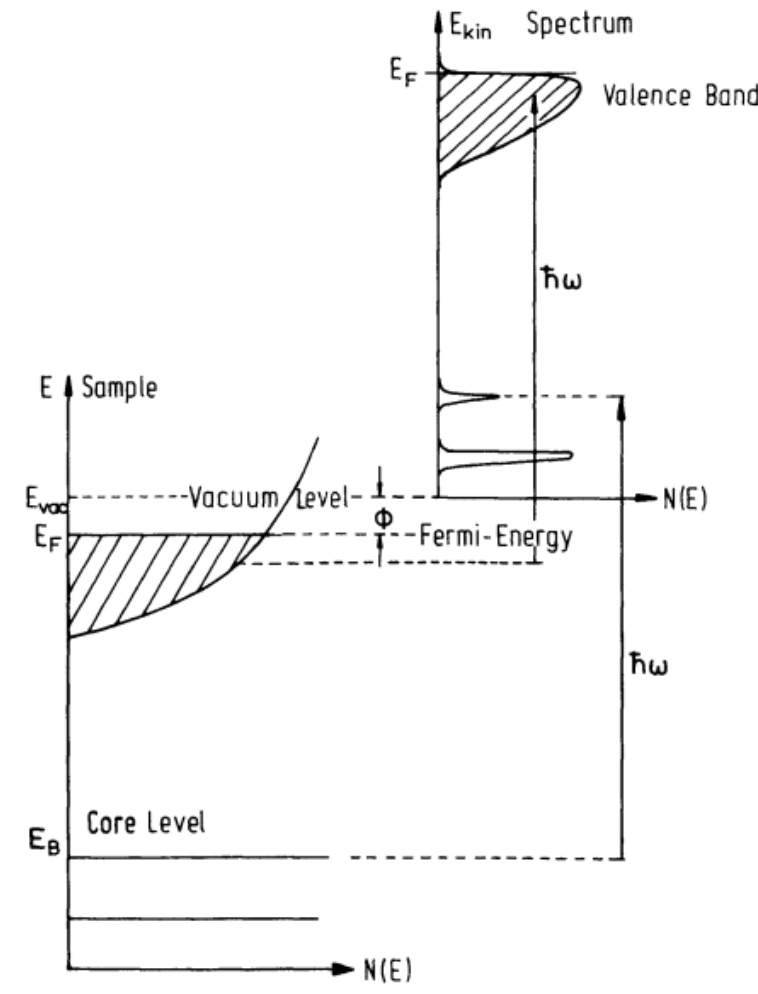


Figure 2.4: Relation between the energy levels of a sample and the electron energy distribution observed at spectrum obtained from a light energy of $\hbar\omega$ (extracted from [47]).

Spectra Analysis

The peaks at XPS spectra are labeled as $X nL_J$, where the X is the symbol of the element from which electrons were ejected, followed by the principal (n), orbital (L), and total (J) quantum numbers. Principal quantum number assumes the values of 1, 2, 3 and so on; the orbital angular momentum is represented by the letters s , p , d and f with the values of 0, 1, 2 and 3 respectively; and the total angular momentum is the sum of spin ($1/2, -1/2$) with the orbital angular momentum, $J = |L + S|$, for example the Mn $2p_{3/2}$. The spin-orbit coupling leads to a peak split, except for the s orbital ($L = 0$), and the peaks intensity is proportional to the electrons' occupation in the orbitals [47].

The frozen-orbital approximation provides information such as the spectrum shape, peak position, and the presence of satellites. Although, it is necessary to consider the response of a system with a core hole for further electronic structure analyses. When the X-ray source illuminates the sample, electrons are ejected from the atom and leave a hole. The core-hole exists for about 10^{-15} s until a decay process happens. Meanwhile, the Coulomb interaction between the core-hole and the valence-electrons changes the electronic states to a final state. The XPS spectrum obtained results from these final states, which can be many for the Mn $2p$ peak. This peak reveals the spin-orbit splitting that results in a complex spectrum, which will be explored forward [47, 48].

The Mn $2p$ peak will be fitted following the theory developed and presented by Bagus et al. (2006) [32]. Figure 2.5 shows the result of calculations for an MnO_6 cluster embedded in a point-charge environment, where the lattice structure of MnO were considered. Therefore, the Madelung potential were reproduced what not happen when it is calculated for the isolated cation (Mn^{2+}). The multiplet contributions arise from the angular momentum coupling of the open $2p_{3/2}$ shell with the open valence $3d$ shell of the Mn^{2+} coupled to high spin 6S [32, 49]. Thus, the experimental data fit for the MnO spectra were performed with the constraints ± 0.2 eV of energy and $\pm 10\%$ of intensity, as presented by Table 2.1. However, the calculated values are presented only for the Mn $2p_{3/2}$ peak.

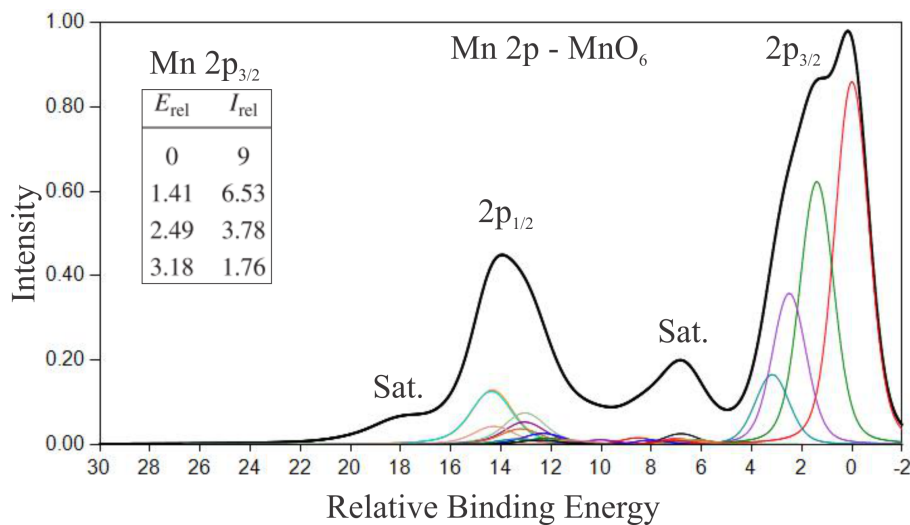


Figure 2.5: Mn $2p$ theory of multiplets for an MnO_6 cluster, table inside with the intensities and position of each multiplet of Mn $2p_{3/2}$ peak (adapted from [32]).

It is a challenge to perform the fit of the whole Mn $2p$ peak due to the angular momentum coupling of the $2p_{1/2}$ shell with the $3d^5(^6S)$ is different from that of the $2p_{3/2}$, and also the satellite peak which is near at this region. However, once the whole peak is fitted, information about the $2p_{1/2}$ can be obtained. Therefore, the $2p_{1/2}$ region was fitted with the same number of $2p_{3/2}$ multiplets but decreased the binding energy. Although the deconvolution might not be exactly like that, the components should be in accordance with the theory by the constraints to fit the spectrum, hence, this should be reasonable.

	Mn $2p_{3/2}$		Mn $2p_{1/2}$
Multiplet	E_{rel} (± 0.2 eV)	I_{rel} (± 10 %)	E_{rel} (± 0.2 eV)
1	0	1	0
2	1.4	0.7	- 1.4
3	2.5	0.4	- 2.5
4	3.2	0.2	- 3.2

Table 2.1: Values applied to fit the experimental data of MnO spectra (based on [32]).

2.3 Thermal Desorption Spectroscopy (TDS)

Thermal Desorption Spectroscopy (TDS), or Temperature-Programmed Desorption (TPD), is one of the techniques in which a chemical reaction on the surface is monitored, while the sample temperature increases linearly in time. After covering the sample with a determined gas-phase molecule, at a constant temperature, desorption spectroscopy is performed by raising the temperature. When the surface temperature increases with time, $\beta(t) = dT/dt$, the adsorbed molecules start to leave the surface. The spectrometer measures the concentration of desorbing species in the function of temperature. Due to the experimental conditions, the re-adsorption can be disregarded [50,51]. Figure 2.6 presents the TDS experiment scheme, where the quadrupole mass spectrometer (QMS) stands in front of the sample surface.

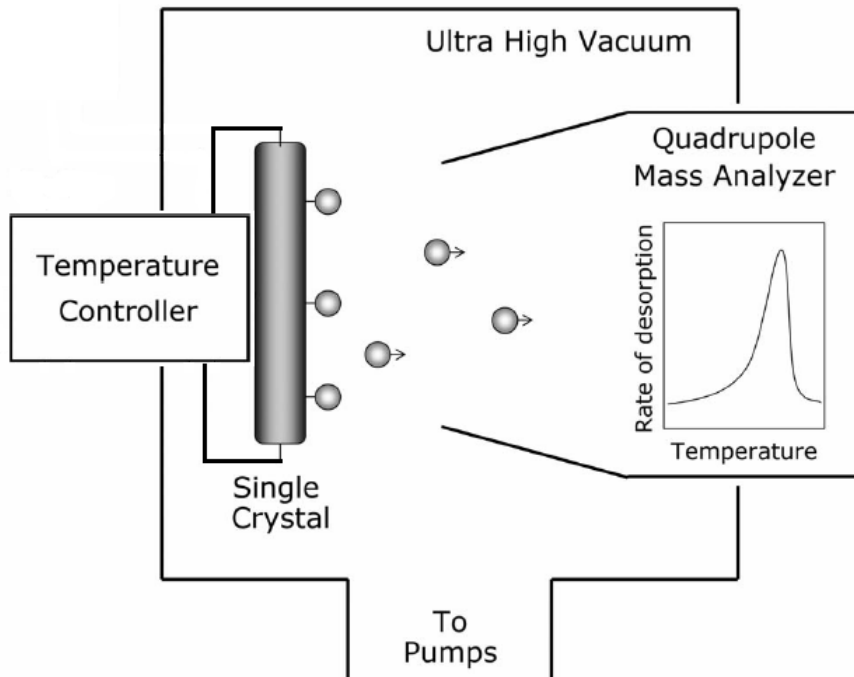


Figure 2.6: TDS experiment scheme: The temperature of the sample is varied with the time while the quadrupole mass spectrometer (QMS), which is in front of the surface sample, measures the concentration of desorbing species (extracted from [51]).

The rate of desorption (r_d) is proportional to the surface coverage (θ) described by the Polanyi-Wigner equation,

$$r_d = -\frac{d\theta}{dt} = k_d \cdot \theta^x. \quad (2.8)$$

Where x is the order of desorption, k_d is the rate constant that depends on activation energy (E) since desorption it is always an active process. Defining the rate constant by the Arrhenius equation,

$$k_d = \nu(\theta) \cdot \exp\left(-\frac{E(\theta)}{RT}\right), \quad (2.9)$$

where the R is the ideal gas constant, T is the temperature, and $\nu(\theta)$ is the pre-exponential factor. The Arrhenius (2.8) and Polanyi-Wigner (2.9) equations combined to give the

equation that describes the rate of desorption, *i.e.* change in adsorbate coverage per unit of time:

$$r_d = -\frac{d\theta}{dt} = \nu(\theta) \cdot \exp\left(-\frac{E(\theta)}{RT}\right) \cdot \theta^x. \quad (2.10)$$

That equation can be rewritten as a function of temperature, which describes the desorption signal intensity [50]:

$$r_d(T) = -\frac{d\theta}{dT} = \frac{\nu(\theta)}{\beta(t)} \cdot \exp\left(-\frac{E(\theta)}{RT}\right) \cdot \theta^x. \quad (2.11)$$

Figure 2.7 shows the coverage-spectra simulation using 2.11 performed by Badan [52]. These curve trends are a fingerprint for each order of desorption, which will be treated individually forward.

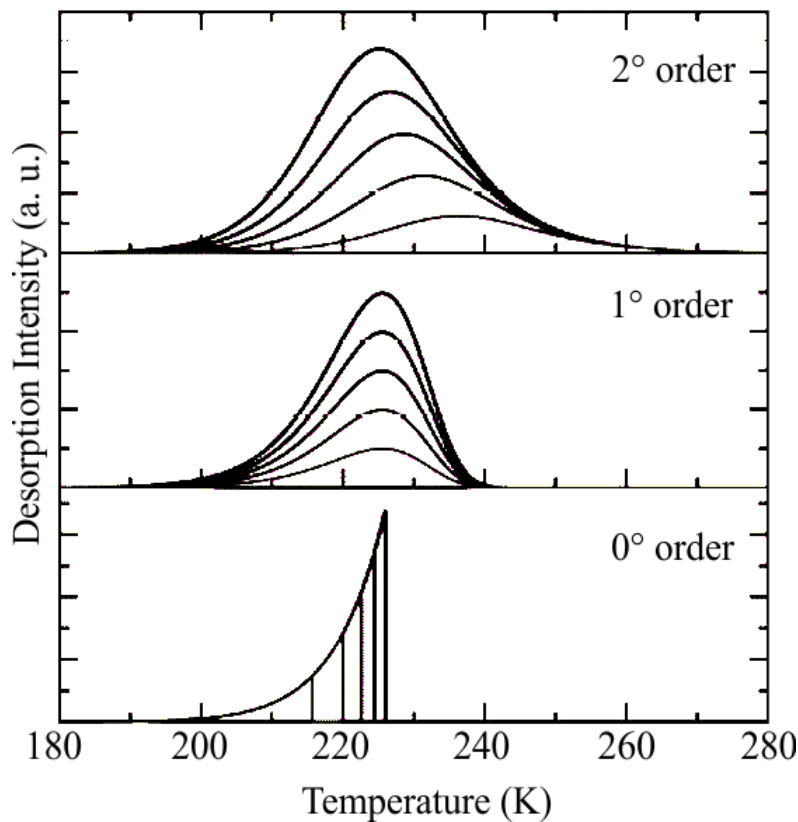


Figure 2.7: Coverage-spectra simulation for second-, first- and zero-order performed by Badan (2016). $E = 60\text{kJ/mol}$; $\nu = 10^{13}\text{s}^{-1}$; coverages of 0.2, 0.4, 0.6, 0.8 and 1.0 ML. Adapted from [52].

The zero-order, $x = 0$, presents a desorption rate independent of coverage and increases exponentially with T,

$$r_d(T) = \frac{\nu}{\beta} \cdot \exp\left(-\frac{E}{RT}\right). \quad (2.12)$$

A family of curves with a common leading edge and maximum desorption is expected, which shift to high temperature with coverage increase. The spectra of water desorption from the FeO(111) surface, presented in Figure 2.8(a), exhibit the same curve trend observed in Figure 2.7 [53].

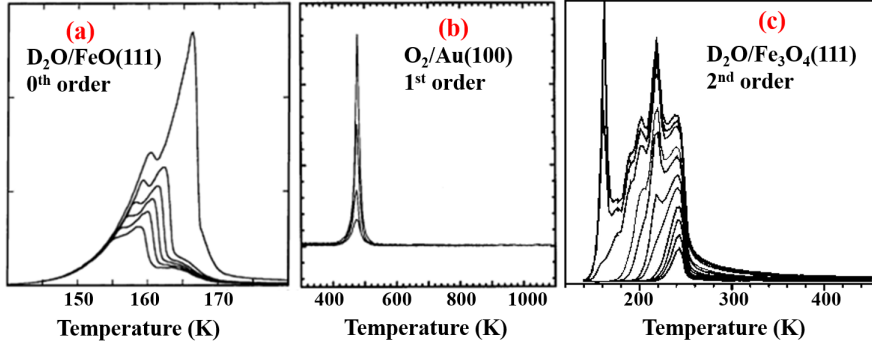


Figure 2.8: Three TDS data of coverage dependence, where the surfaces were previously charged with molecules. (Adapted from [53, 54]).

The first order, $x = 1$, represent many molecular desorption events,

$$r_d(T) = \frac{\nu}{\beta} \cdot \exp\left(-\frac{E}{RT}\right) \cdot \theta(T). \quad (2.13)$$

Equation 2.13 enables analysis at maximum desorption peak, *i.e.* $dr_d/dT = 0$,

$$E = RT_m \cdot \ln\left(\frac{\nu RT_m^2}{\beta E}\right). \quad (2.14)$$

The temperature receives an index (T_m) because this is the temperature of the maximum desorption. Observe that the activation energy does not depend on the coverage, then the fingerprint on the spectrum is a peak that does not change the T_m with the coverage. Another important observation is the relation of temperature and activation energy, the T_m shift on the spectrum when the E changes. The simulation for the first-order desorption (Figure 2.7) draws those observations, and also it is observed that after the maximum peak, the curve will be asymmetric and decrease fast. Figure 2.8(b) shows the coverage spectra of O_2 desorbed from Au(100) surface, and the first-order desorption trending is well observed [55].

Second-order desorption, $x = 2$, corresponds to the recombinative desorption of molecules. The previous analyses can be repeated here and are obtained with a similar equation,

$$E = RT_m \cdot \ln\left(\frac{2\theta\nu RT_m^2}{\beta E}\right), \quad (2.15)$$

but now the activation energy depends on surface coverage. Taking apart the equation into two parts,

$$E_2 = E_1 + RT_m \cdot \ln(2\theta), \quad (2.16)$$

where the E_1 refers to the part of the equation similar to the activation energy of first-order (2.14), and E_2 refers to the activation energy of second-order. Rearranging the terms,

$$T_m = \frac{E_2 - E_1}{R \cdot \ln(2\theta)}. \quad (2.17)$$

An increase in coverage will shift the maximum peak to low temperature, as observed by the simulation (Figure 2.7). The common trailing edges will be a signature of that order as the symmetric peak shift. The coverage spectra of water desorption from $Fe_3O_4(111)$ surface (Figure 2.8(c)) present the second-order trending [54].

2.4 Infrared Reflection Absorption Spectroscopy (IRAS)

The Infrared Reflection Absorption Spectroscopy (IRAS) technique has been used for different systems to investigate molecules adsorbed on the surface [56]. When the infrared (IR) light irradiates a surface, vibrational modes from the lattice and adsorbed molecules can be excited. Therefore, the IR light induces transitions between the vibrational levels, which happens under selection rules imposed by the surface and photon absorption conditions [57, 58].

Vibrations by IR Light Interaction

The motion of a particle at axes of the Cartesian coordinates system, often labeled as (x, y, z) , describes the translational degrees of freedom. The rotation motion of particles around a fixed point describes the rotation degrees of freedom. In contrast, the movement that changes the distance and angles between the particles of a molecule is related to the vibrational degrees of freedom. A molecule has $3N$ degrees of freedom where N is the number of atoms, and three of the degrees are translational. The other two will be rotational for a linear molecule, and the remaining $3N-5$ will be vibrational. For a non-linear molecule, three will be rotational, and $3N-6$ will be vibrational. The IR light electric field interacts with the molecule dipole moment, changing the length and angle of the chemical bond between the particles [57, 58].

When a surface absorbs the particles, all freedom motion is vibrational, and the surface has more $3N$ vibrational degrees of freedom associated with the adsorbed molecule. An example represents the adsorption of OH molecule on Si atoms at silica lattice framework (Figure 2.9). As the OH has two atoms, the surface now has six new vibrational degrees of freedom, and each vibration is labeled in the Figure [57].

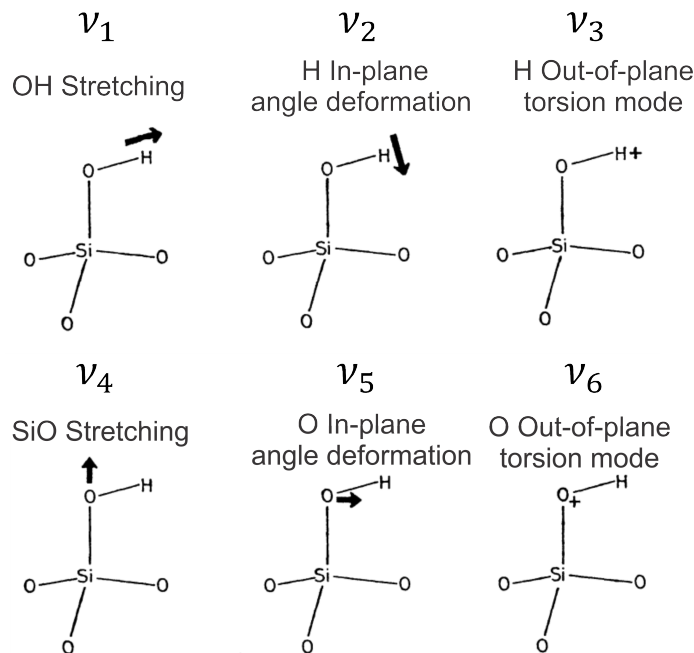


Figure 2.9: Representation drawing of vibration normal modes of OH group bonded to a Si atom on a silica lattice framework (adapted from [57]).

In the IRAS experiment, the electric field of IR light excites the vibration modes of the surface adsorbed molecules. The adsorption of the IR light promotes a transition from an initial (E_i) to a final (E_f) energy level of molecular vibrations, which is quantized as exhibited by equation 2.18:

$$h\nu = E_f - E_i. \quad (2.18)$$

Where the $h\nu$ is the photon energy, which for the Mid IR is in the range of 25 - 496 meV (200 - 4000 cm^{-1}) [51]. Furthermore, the transition dipole moment $(\mu_j)_t$ must be unequal zero, which can be described as the equation 2.19:

$$(\mu_j)_t = \int_{-\infty}^{\infty} \Psi_f \mu_j(q) \Psi_i dq \neq 0. \quad (2.19)$$

The index j refers to the Cartesian coordinates, where the transition dipole moment is not zero for x, y, or z coordination. This index will be implicit from the forward equations once we consider that it is not zero for one of the Cartesian coordination. The Ψ_f and Ψ_i are the eigenfunctions of the molecule in its final and initial vibrational state. The q is the displacement coordinate of the molecule vibration; hence the dipole moment is a function of this coordination. Applying the harmonic oscillator approximation, the dipole moment can be expanded in Taylor series,

$$\mu(q) = \mu(0) + \mu'(0)q + \mu''(0)\frac{q^2}{2} + \dots \quad (2.20)$$

It is not expected to have a large displacement, then it is considered only until the first order. Therefore, the equation 2.19 is rewrite as:

$$\mu_t = \mu(0)\delta_{fi} + \mu'(0) \int_{-\infty}^{\infty} \Psi_f q \Psi_i dq \neq 0. \quad (2.21)$$

The first term is unequal zero only if the final state is equal to the initial state ($\delta_{fi} = 1$ for $f = i$ and 0 for $f \neq i$), this happen due to the orthogonality property of the eigenfunctions from the harmonic oscillator approximation. The second term yield two selection rule: (1) The electric dipole moment must be a function of the vibration displacement, $\mu'(0) \neq 0$, to result in an IR-active; (2) The final state must be the initial state ± 1 when the integral is unequal zero. Therefore, overtones (*i. e.* $i = 0$ and $f = 2, 3, \dots$) are forbidden hence result in weak intensity on the spectrum. In the spectrum, most bands are from the fundamental transition (from the ground state to the first excited state).

The interaction of the IR light with the molecule dipole moment will be ruled by the dielectric behavior of the surface [59]. Figure 2.10 presents the drawn image dipole theory, which is equivalent to the surface selection rule [57]. Although it was developed for metal surfaces, it is true for thin films grown on metallic substrates as long as the film thickness is much smaller than the light wavelength ($d \ll \lambda_{IR}$) [58]. The sum dipole moment of molecule and surface will interact with the IR light electric field. Therefore, the adsorbed molecules induce a charge movement on the surface that the dipole will be enhanced at the perpendicular surface direction, and the parallel will vanish. Consequently, the IR spectrum will not observe vibrations parallel to the surface, only the vibrations with a perpendicular component [57].

That surface selection rule can be viewed by the interaction of sum dipole moment and the IR light as observed by Figure 2.11 [58]. The light electric field can be decomposed

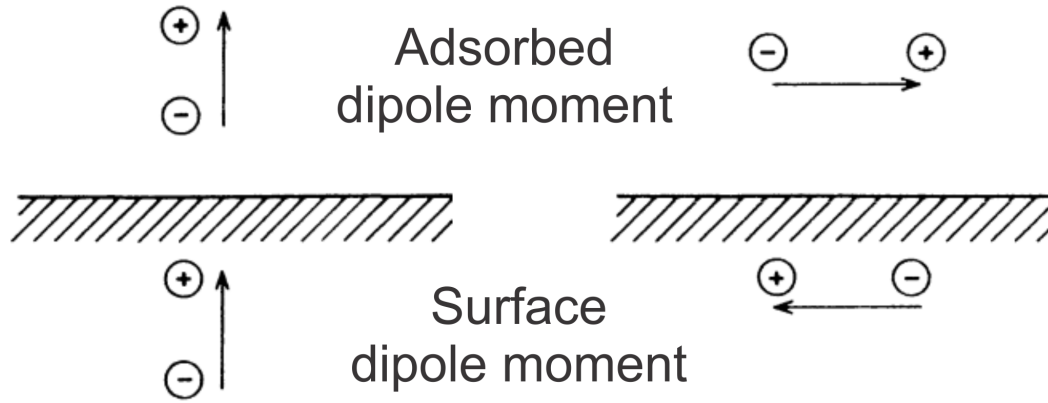


Figure 2.10: The image dipole theory of surface selection rule was drawn (Adapted from [57]).

into polarized perpendicular to the surface (p) and parallel to the surface (s). For all incidence angles (ϕ), the electrical field s-polarized has a uniform phase shift of about 180° , resulting in destructive interference ($E_s^i + E_s^r = 0$). The p-polarized electric field vector can be decomposed into two components. The components that lie down on the surface plane vanish through the same argument of s-vectors, and the other is summed in the normal direction (red arrow).

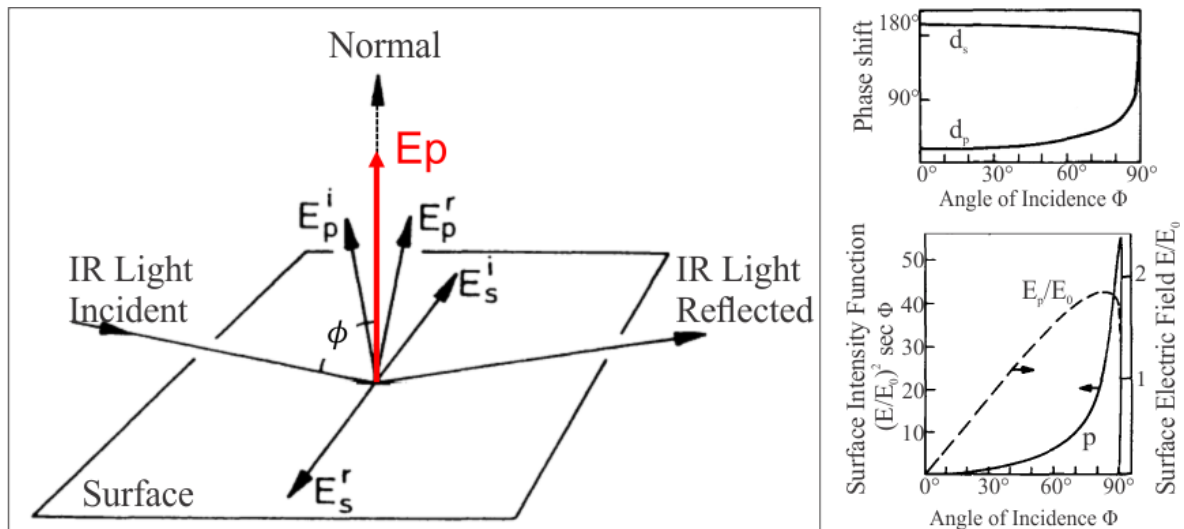


Figure 2.11: Representation of incident and reflected IR light by the surface, the phase shift in function of incidence angle ϕ and the surface electrical field (Adapted from [58]).

The p-component has a phase shift that depends on the incidence angle (ϕ), its intensity enhanced at a high incidence angle. Therefore, the experiment is performed at surface grazing angles and limited to the p-polarized IR light, and the total adsorption intensity is given by the equation 2.22.

$$\Delta R = \left(\frac{E_p^\perp}{E_p^i} \right)^2 \sec\theta \quad (2.22)$$

Figure 2.12 shows the total adsorption intensity, obtained experimentally through $\Delta R = R^0 - R$, where the R and R^0 are the reflectance with and without the adsorbate, respectively. And the spectra are presented by the absorption function, which is $\Delta R/R^0$ [57].

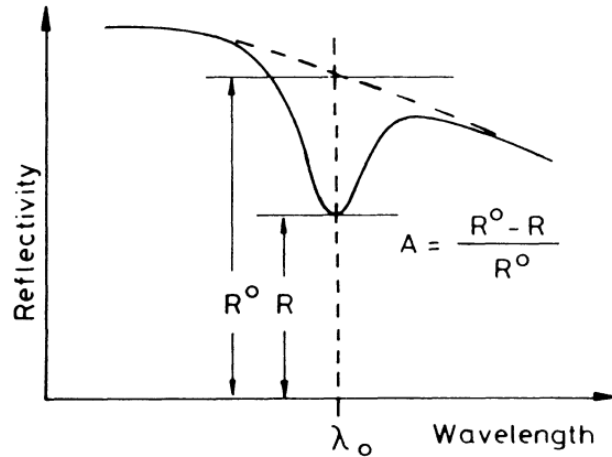


Figure 2.12: The total adsorption intensity and the absorption function A obtained from the spectrum. Extracted from [57].

Figure 2.13 shows the IRAS survey spectrum, range from 2800 cm^{-1} until 1000 cm^{-1} . The spectrum is from water (D_2O) adsorbed on $\text{Au}(111)$, where the adsorption peaks are from the distinct vibration of water.

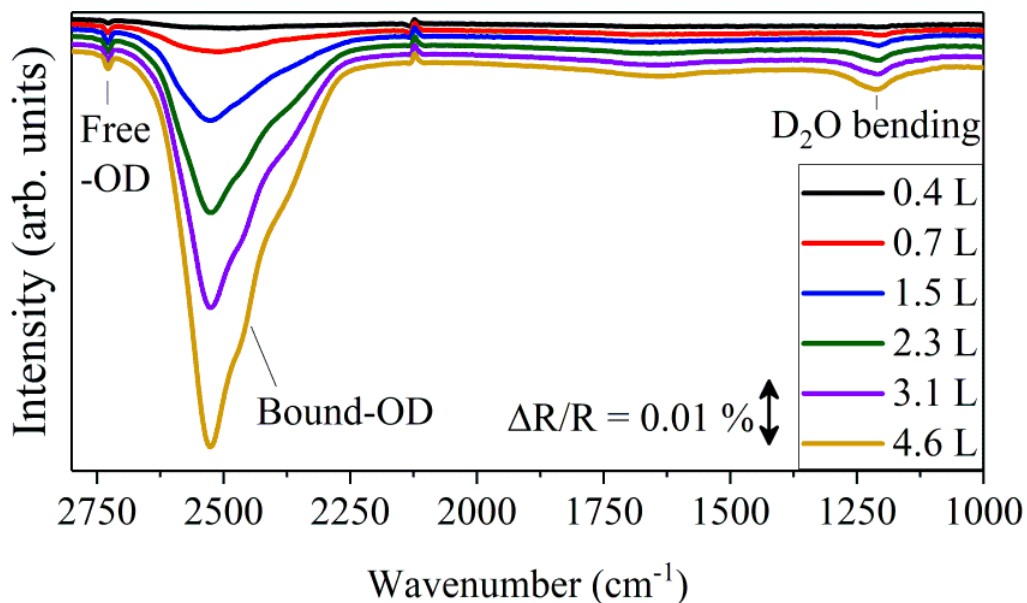


Figure 2.13: IRAS survey spectra of water on $\text{Au}(111)$ substrate.

Before the sample surface is exposed to the molecules, a background is taken. Therefore, the surface with all molecules present will be considered a zero point. The downwards bands (negative peaks) indicate the formation of new species on the surface. It is expected to observe the negative bands related to the molecules adsorbed on the surface.

The species that were present while the background was taken and, with time, just leaving the surface resulted in the upwards bands (positive peaks). A positive, nearly negative peak is observed when a species changes on the surface but is still there. Figure 2.13 shows only the positive and negative bands.

Since the detector operates at low temperatures, a water signal will be present in our data. Therefore, we employed deuterium, which has the same chemical properties as water and will not affect our results. We are interested in observing the hydroxyl groups formed on the surface, then the region exhibited will be the Free-OD ($2800 - 2600 \text{ cm}^{-1}$). This region represents the stretch of O-D bond; therefore, this region can present peaks from water dissociated. The position of the peaks is a fingerprint of the molecule vibration, which gives access to understanding how the molecules adsorbed on the surface.

Experiment Geometry

In short, the experimental setup comprises an interferometer to perform Fourier Transform IR (FTIR) spectrometer. The spectra obtained show a strongly improved signal-to-noise ratio, allowing for adsorbate signals' resolution. The IR beam passes through the beam splitter, sending part of the light to a fixed mirror and another to a movable mirror. Therefore, these two beams are directed to the surface, at the grazing incidence, and directed to the detector. First, the interferogram is detected and processed via Fourier-Transform, then the IR spectrum is obtained. Figure 2.14 shows an example of the IRAS setup, and the UHV chamber is in the beam path between the spectrometer and the detector.

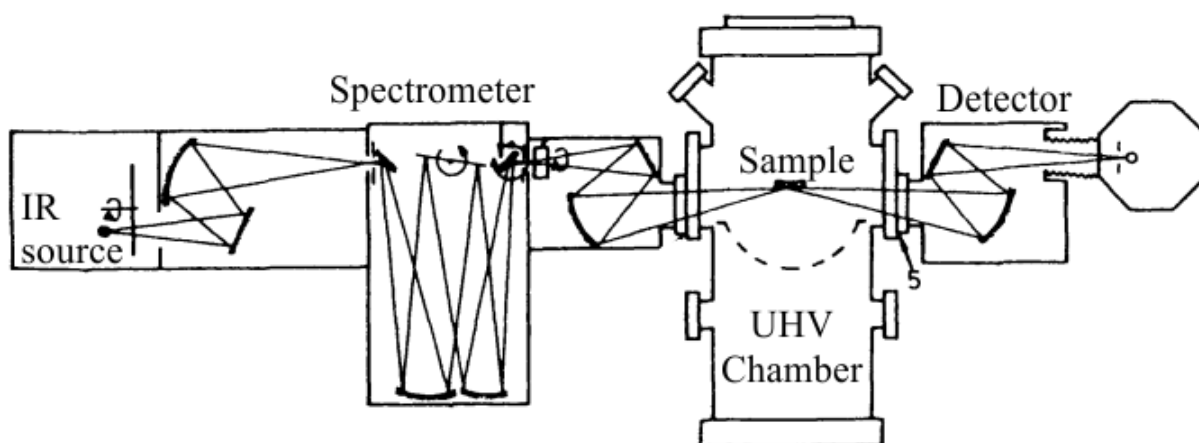


Figure 2.14: Example of IRAS setup (adapted from [57])

2.5 UHV Systems

The XPS and LEED experiments were performed in Brazil (CBPF/ Rio de Janeiro) at the Laboratory of Surfaces and Nanostructures (LabSurf), coordinated by Prof. Dr. Alexandre Mello. Figure 2.15 shows the equipment (SPECS) composed of different chambers. Load Lock chamber (base pressure of 1.10^{-7} mbar) to introduce samples. The preparation chamber (base pressure of 4.10^{-9} mbar) to clean the sample and grow the thin films is equipped with the LEED to observe the crystalline ordering of substrate and films. Analysis chamber (base pressure of 4.10^{-10} mbar) equipped with the spectrometer (HSA Analyzer and DLD detector) and an X-Ray monochromatic source (Al $K\alpha = 1486.6$ eV) to perform the XPS measures. First, the survey spectrum (from 1100 eV until -5 eV) and after the high resolution of each peak was obtained. Then, the fit analysis was performed with CasaXPS software [60]. LEED data were obtained through the pictures taken from the screen, and the analyses include a match of the diffraction pattern obtained with simulations performed with LEEDpat software [45].

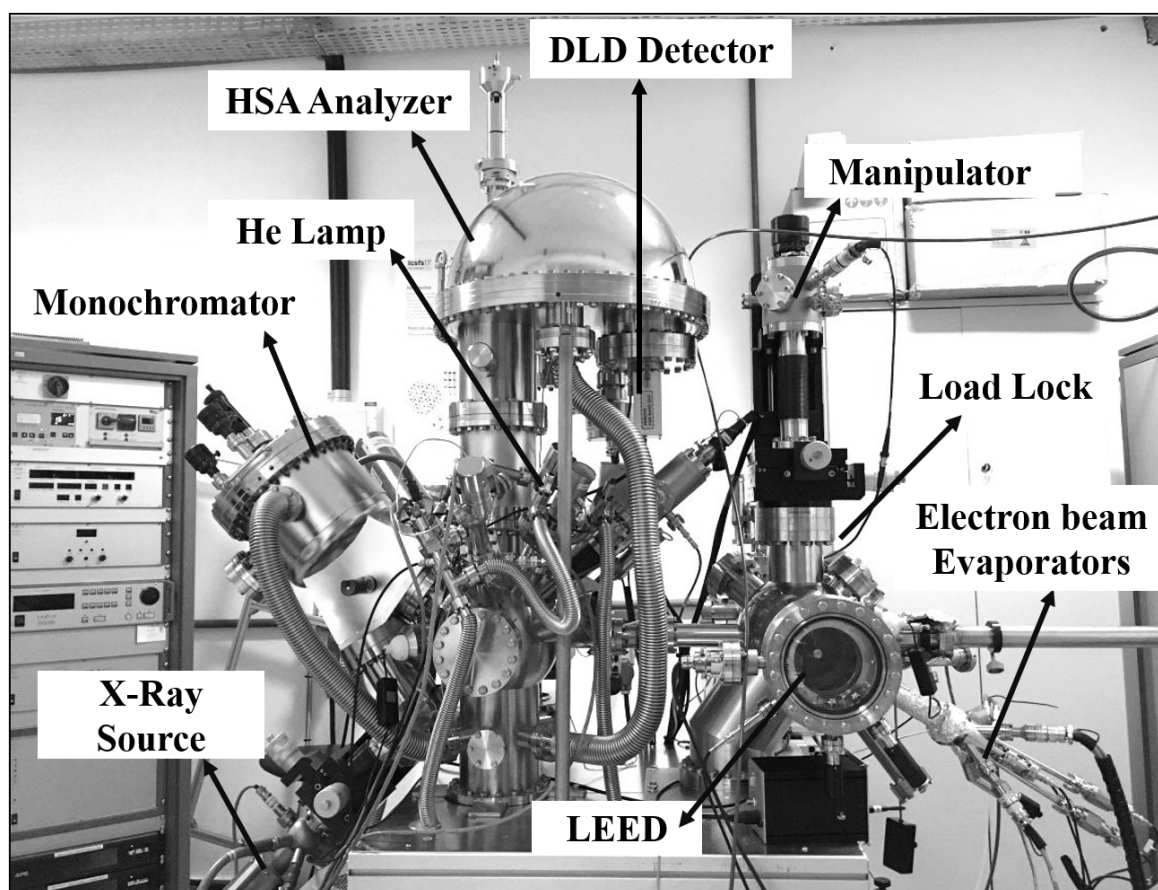


Figure 2.15: Photo of SPECS equipment from the Laboratory of Surfaces and Nanostructures (CBPF/Rio de Janeiro) (adapted from [31]).

The molecules adsorption experiments investigated by the infrared spectroscopy were performed in collaboration with two research groups in Germany. Both equipments comprise a single UHV chamber ($\sim 2 \times 10^{-10}$ mbar) where the films were grown and the molecules were adsorbed as well measured. For the MnO films, the data were obtained in collaboration with the laboratory of Structure and Reactivity (Figure 2.16a), coordi-

nated by Dr. Shamil Shaikhutdinov and led by director Prof. Dr. Hans-Joachim Freund (FHI/Berlin). The instrument is equipped with a Bruker IFS 66v/S IR spectrometer, quadrupole mass spectrometer (QMS), and the LEED apparatus. The spectra were measured at grazing angle 8° and resolution of 4 cm^{-1} . The temperature experiments were performed with a rate of 3 K/s , controlled by direct current heating in conjunction with LN_2 cooling. For the Mn_3O_4 films, the data were obtained in collaboration with the laboratory of Interface Research and Catalysis (Figure 2.16b), coordinated by Prof. Dr. Jörg Libuda (FAU/Erlangen). The instrument is equipped with the Bruker VERTEX 80v IR spectrometer and the liquid nitrogen-cooled mercury cadmium telluride (LN-MCT) detector. The background signal and the data are taken with a scan velocity of 20 kHz and a resolution of 4 cm^{-1} .

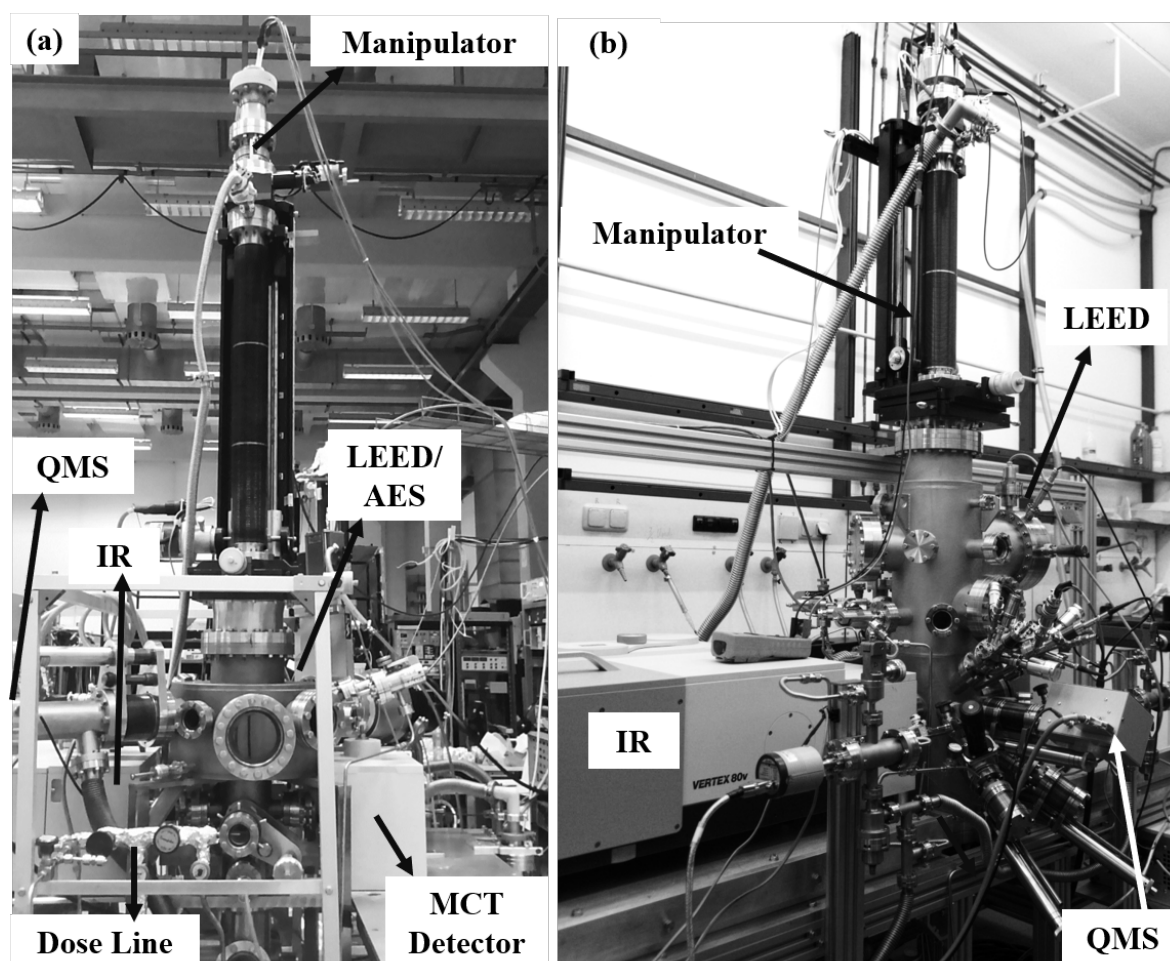


Figure 2.16: (a) Picture of the IRAS equipment with others facilities from the laboratory of Structure and Reactivity (FHI/Berlin) (b) Picture of the IRAS equipment with others facilities from the laboratory of Interface Research and Catalysis (FAU/Erlangen)

2.5.1 Procedures

The Au(111) single-crystal was prepared by cycles of annealing and sputtering in the same way at every apparatus, as well as the MnO_x film's growth (please see more parameters details in the appendix A.1). The films were grown with an Electron Beam Evaporator (EBE), LEED pattern pictures matched the films data, and the adsorption

experiments were performed with a doser system. These procedures will be explained as follows.

Annealing: It comprises sample heating by a filament until 800 K. A differential potential (about 800 V) is applied between the filament, usually tungsten, and the sample. When a current (about 2 A) passes through to the filament, electrons accelerate toward the sample hence heating. The temperature is observed by thermocouples near or in contact with the substrate.

Sputtering: An ion beam hits the sample surface, and atoms layers are removed through the collision. The sample is positioned at an angle (about 30°) regarding the sputtering gun to minimize the damage on the surface. The ion beam is created through a gas, which enters the field where the cathode's electrons are accelerated toward an anode. Then, the electrons can collide with the gas particles, ionize them, and form the ion beam (plasma). This plasma is focused by a lens system and oriented to the sample surface. Although any gas can be used to perform sputtering, argon is usually. It is an inert gas of low cost compared to other inert gases and can be easily removed from the surface once the sputtering process can insert gas atoms on the surface. The ion beam energy is defined by the voltage applied to the anode, ranging from 0 to 3 kV.

EBE: Manganese metallic is evaporated in a chamber filled with a partial oxygen pressure, and post-annealing is performed to promote film crystallization. The evaporator has a filament positioned ahead of the manganese material, accelerating electrons to the metal (emission current of about 13 mA). Due to the vacuum conditions, the metal has a relatively low vapor pressure and easily evaporates to the sample surface. Eventually, a fraction of the manganese particles will be ionized by the electrons, and then a flux current that reaches the sample can be measured (about 150 nA). The Au(111) substrate is kept at room temperature during the film growth.

Gas Dose: The water (D₂O) and carbon monoxide (CO) molecules were inserted from a gas reservoir into the chamber via an electromagnetic valve, where pulses exponentially increase exposure per pulse. The exposure gas were measured in Langmuir, where 10⁻⁶ mbar · 1 s is equal 1 L (Langmuir). Subsequently, IR spectra were acquired (200 scans; acquisition time, 57 s). The gas valves were remote-controlled using a LabView interface (National Instruments). For temperature-programmed IRAS (TP-IRAS), the sample was heated from 110 to 700 K with a heating rate of 2 or 5 K/min (controlled via LabView interface), simultaneously taking the IR spectra (57 s/spectrum, 60 s delay).

2.5.2 Au(111) Substrate

Figure 2.17a exhibits the Au(111) diffraction pattern by LEED picture. The spots that perform a hexagon symmetry are composed of center spots surrounded by satellite spots, as indicated by black arrows. While the center spots are from the plane (111) of face-centered cubic structure, FCC(111), the satellites are from herringbone reconstruction [46]. The observation of this LEED picture is only possible if the surface is clean and plain enough to highlight those structures. On the right side (Figure 2.17b), the FCC(111) representation shows the expected hexagon symmetry with the surface lattice parameter of 2.88 Å. Please observe that the two surface parameters are equal, and the angle between

them is 60° . Therefore, equation 2.23 makes it possible to determine the film's surface lattice parameter by the substrate LEED image:

$$a_f = \frac{a_s \times d_s}{d_f}, \quad (2.23)$$

where a_s and a_f are the lattice parameter of gold (2.88 \AA) and film, d_s and d_f are the circle diameter on LEED screen of gold and film respectively [31].

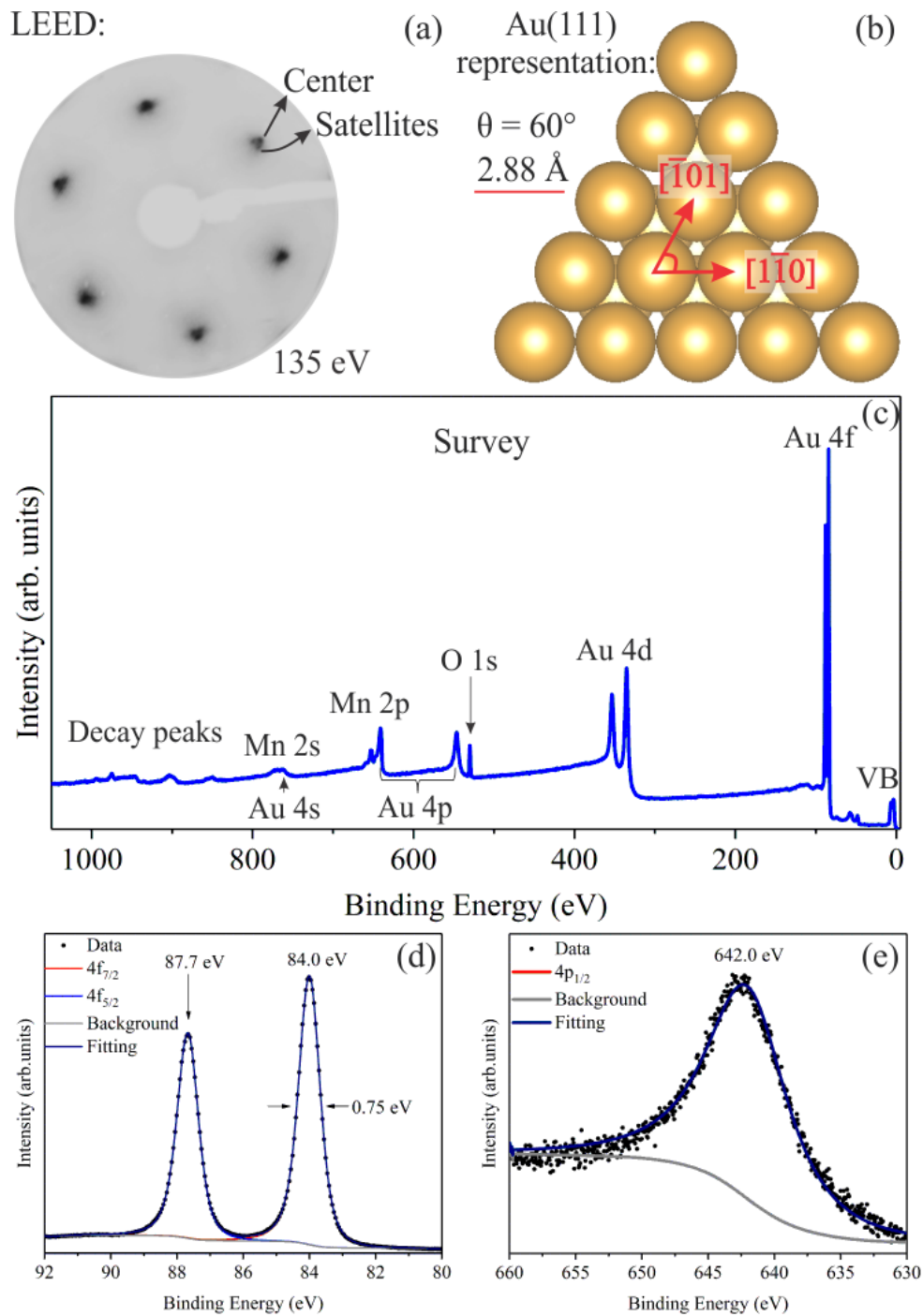


Figure 2.17: (a) Diffraction pattern by LEED picture and (b) real lattice representation of Au(111). Spectra (Al K_α source) of Au(111) for (c) survey (d) 4f and (e) 4p_{1/2} peaks.

Figure 2.17c-e presents spectra of Au(111) clean surface for the survey and the two high resolution $4f$ and $4p_{1/2}$ peaks. The survey spectrum shows all the core-levels peaks from Au and MnO_x ; above 800 eV are the decay peaks and below 50 eV is the valence band. It is observed that some peaks are at the same binding energy region. Since the Au $4f$ is the most intense peak of Au, it is very hard to observe the Mn $3s$. Although the Au $4p_{1/2}$ is at the same binding energy as Mn $2p$, it is possible to extract this peak contribution. Therefore, the Au $4f$ and $4p_{3/2}$ peaks were fitted to obtain the data resolution and to remove the substrate contribution. Both with the Voigt function, which better reproduces the spectrum shape, LA(1.4, 1.5, 10) for $4p_{1/2}$ and LA(1.5,1.6,70) for $4f$ [61,62]. The spectra resolution obtained was 0.75 eV (Full Width at Half Maximum - FWHM).

The electron inelastic mean free path of both peaks, Au $4p_{1/2}$ and Au $4p_{3/2}$, were calculated and resulted in 1.7 nm and 1.9 nm, respectively. Therefore, it is possible to rescale the Au $4p_{1/2}$ intensity by the intensity of Au $4p_{3/2}$, since the MnO film thickness investigated (1-2 nm) would not significantly affect their relative intensity [63]. Figure 2.18 shows the spectra before and after background subtraction (black spectrum). The choice of the Shirley-type background relies on the few layers' nature of our sample, in which photo-electron effective attenuation length for the comparison of a particular binding energy range should generally not affect the trends observed. Figure 2.18 shows the procedure to remove the Au $4p_{1/2}$ peak contribution. Three different MnO spectra are presented: First, the Shirley background is removed, and post, the substrate peak is removed. Note that the Mn $2p_{3/2}$ peak loses its intensity but does not change its shape, while the Mn $2p_{1/2}$ does not present modifications with this process. Therefore, the Au $4p_{1/2}$ peak can be subtracted from the spectra or can be inserted fixed into the spectrum, and this choice should not change the spectra shape.

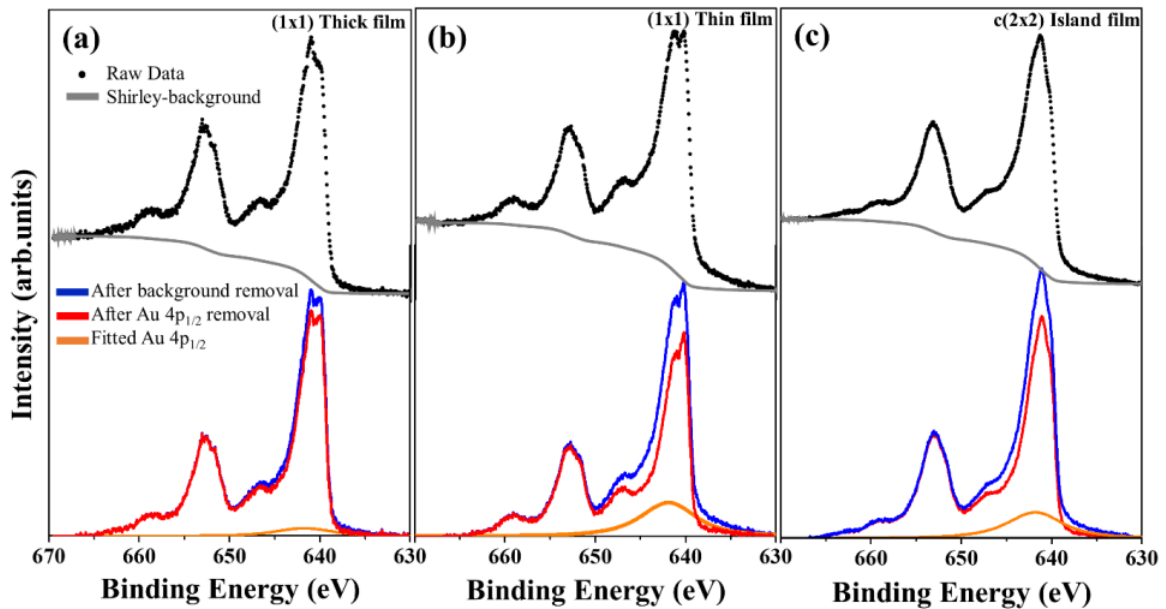


Figure 2.18: Procedure to remove the Au $4p_{1/2}$ peak contribution inside of Mn $2p$.

Chapter 3

Results

3.1 Core-level BE Shifts in MnO(001) Thin Films

3.1.1 Introduction

The Madelung potential, which is electrostatic energy, is the main contribution to the binding energy (BE) on ionic crystals. For a covalent solid with a stronger ionic character, such as the MnO, the Madelung energy will affect the BE as well. The magnitude of the Madelung potential decreases with the decrease of the atoms' coordination site. For example, its magnitude for the bulk (with ideally 6-nearest neighbors) is higher than the terrace surface (with ideally 5-nearest neighbors) and edges (with 4-nearest neighbors). Therefore, bulk, terrace, and edges will present components with different BE on the spectrum. As the Madelung potential raises the BE of anion and lowers the BE of cation, the anion and the cation components will shift respectively to lower and higher BE on the spectrum. This effect is known as Surface Core Level Shift (SCLS) due to the Madelung potential magnitude for atoms at different coordination sites [64]. The SCLS has been known for some time [65]. However, the SCLS was found in literature only for ionic oxide crystals, such as the CaO [66] and the MgO [67] materials. For both oxides, the SCLS of the cations and the anions gave significant insight into the surface properties.

In this section, we extended the SCLS to study BE shifts between the interior, terrace, and edge atoms for monolayers of MnO(001) thin films. Specifically, it will be made for three distinct forms of MnO(001) films named (1×1)-thick film, (1×1)-thin film, and islands exhibiting a $c(2\times 2)$ surface structure (more about these films, please see appendix A.1). For these films, shifts of the BEs related to interior, terrace, and edge atoms were identified, described as Core Level Shifts (CLS), and unambiguously related to the specific positions of the different oxide atoms. In addition, it is necessary to know how to perform the Mn 2p peak fit. Therefore, this thesis will take the challenge to fit the whole peak following the multiplet splitting theory (presented in the section 2.2). To our best knowledge, this is the first attempt to fit the entire Mn 2p spectrum. It is also the first time to explain the line shape of this spectrum and the application of CLS theory to a covalent material. Furthermore, the CLS can provide information about the relative amount of low-coordinated atoms on the surface hence improving our understanding of their potential catalytic properties for further investigations.

3.1.2 Results and Discussion

The first film to be analysed here has a thickness of 0.5 nm, grown with oxygen partial pressure of $5 \cdot 10^{-8}$ mbar and heated at 800 K. Figure 3.1a shows a LEED picture (at 75 eV), where two circles of twelve spots each are observed, and between them are the Au(111) spots. Due to the low thickness, it is expected to see the gold diffraction pattern on LEED. The lattice parameter measured by equation 2.23 was 0.3 nm. On the right side of the figure (a) have a simulation of this diffraction pattern, in which the empty circles represent the substrate spots, and the filled circles represent the film spots. It used a square symmetry with a surface lattice parameter of 3.15 \AA and allowed domains to perform the simulation (illustrated by three-color squares). Since the simulation and the LEED image match very well, this film structure is determined as $(1 \times 1)\text{MnO}(001)$ with three domains rotated by 60° . It was considered other possible structures, and none reproduced the diffraction pattern observed. Figure 3.1b shows the scanning tunneling microscopy (STM) image for a film grown *in situ* in the same conditions in another UHV chamber (STM images by Rubem Caetano). Unfortunately, the MnO has a large bandgap that makes it harder to observe the high-resolution film structure. However, the film wets the substrate surface, forming a thin film on the Au(111) substrate. Note that this is not the only condition to grow $(1 \times 1)\text{MnO}(001)$ crystalline, but it is the best condition for that.

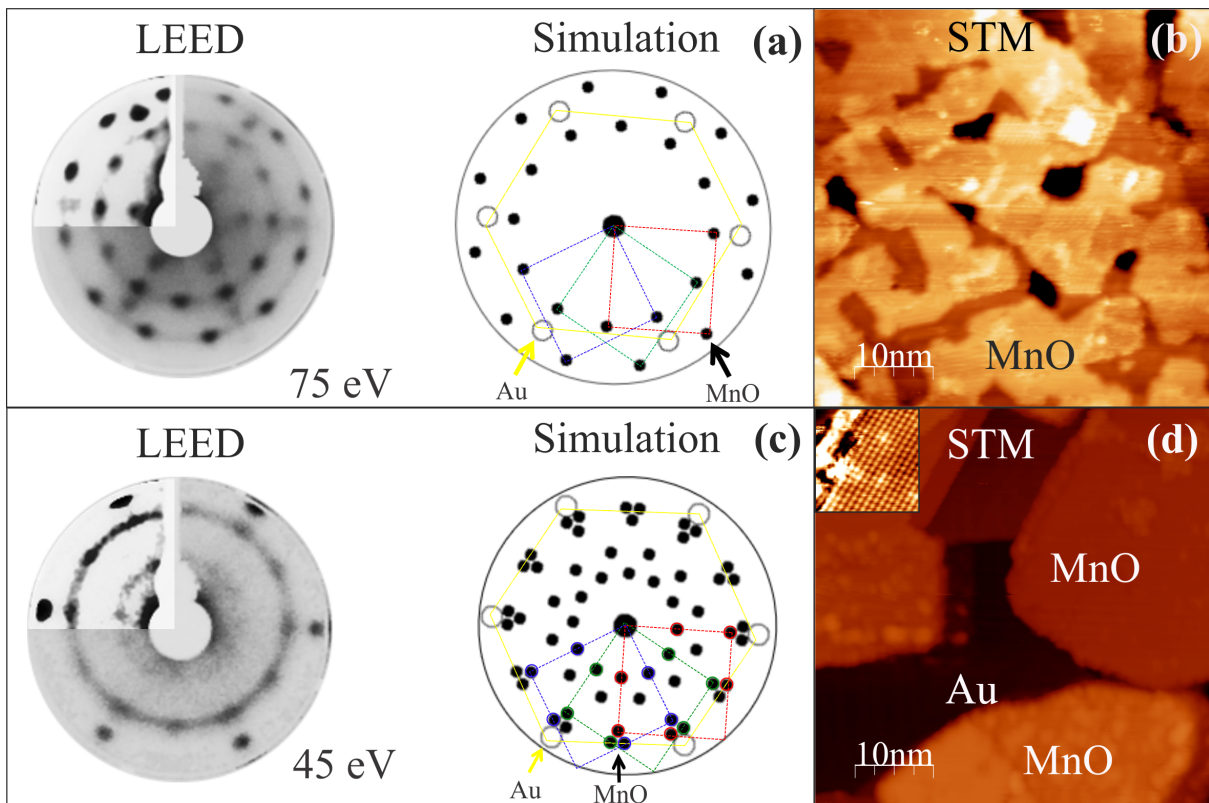


Figure 3.1: (a) LEED image by the side of LEEDpat simulation (b) and the corresponding STM image of the film $(1 \times 1)\text{MnO}(001)$. The corresponding (c) LEED image, simulation and (d) STM image of $c(2 \times 2)\text{MnO}(001)$ film. STM images by Rubem Caetano (CBPF).

The second film also has a thickness of 0.5 nm, but it was grown with higher oxygen pressure ($1 \cdot 10^{-7}$ mbar) and heated until 650 K. A different diffraction pattern is observed for this film (Figure 3.1c). Now, the LEED image is presented at lower energy than

the previous (at 45 eV) and shows two closed circles around the Au(111) spots. The diffraction pattern evolution for the substrate and all films presented are exhibited in Figure 3.3, forward. The lattice parameter measured for the inner circle was 0.6 nm, twice the $(1\times 1)\text{MnO}(001)$ lattice. In the simulation, on the right side of Figure (c), it was circled the spots visible on the LEED image. It is observed that the first circle has an intensity lesser than the second. The reason is that the second circle is a contribution of three spots while the first is composed of single spots (see in the simulation). The simulation was performed with a square symmetry and lattice parameter of 6.30 Å, also allowing domains. Therefore, this indicates that the surface observed comes from the $c(2\times 2)\text{MnO}(001)$ reconstruction. We made STM images for a film grown under the same conditions to collaborate with this assessment. Different from the previous film, this film structure exhibits islands. A high-resolution STM image (top corner) shows the distance of the atoms, and it was 0.58 nm, which is near the value obtained for the LEED. It is markedly different from the previous film, and this one shows not only a surface reconstruction but also high islands. If the growth conditions change, such as an increase in the temperature or decrease in the oxygen pressure, it will lead the film to convert into (1×1) .

When the thickness increases, the formation of $c(2\times 2)$ reconstruction is not possible. The (1×1) surface has a limit of thickness, which is ≤ 2 nm, above that thickness, the film converts to Mn_3O_4 . Figure 3.2a shows a scanning transmission electron microscope (STEM) image of a (1×1) structure (image by Maria Ramos), where the Au($1\bar{1}0$), MnO(100) and the cape protection are observed respectively. This cape consists of gold metallic particles that are inserted to transport the film in air conditions.

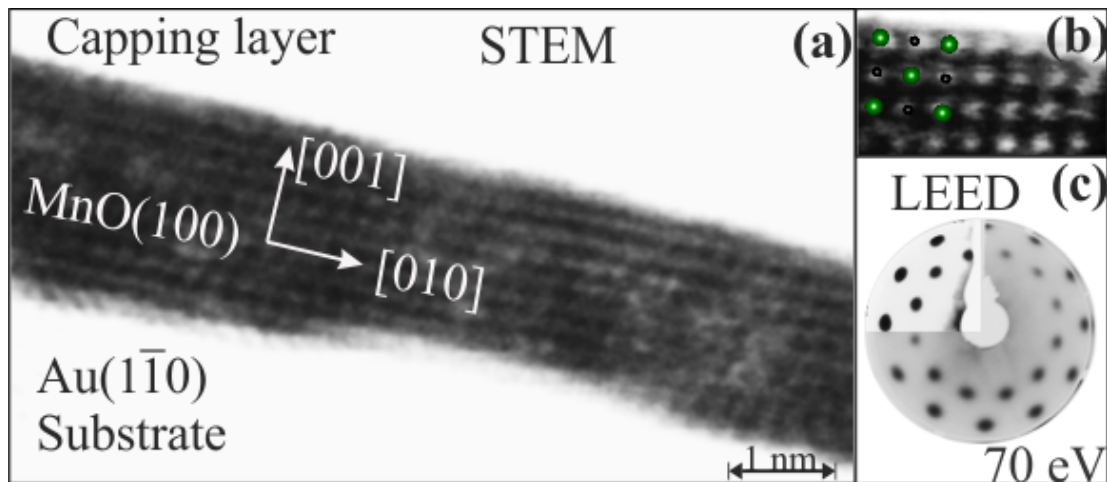


Figure 3.2: (a) STEM image of the thick (1.77 nm) film of (1×1) MnO(100). (b) High-resolution image of film structure (c) and the corresponding LEED. STEM image by Maria Ramos (INMETRO).

In agreement with LEED and STM images, is observed a continuous film composed of a square lattice with atomic distances similar to the expected MnO(100) bulk (Figure 3.2b). Due to MnO insulating character, the image contrast does not allow the observation of the interface. The film thickness can be observed which is about 4 ML of MnO structure (1.77 nm). In the last image (Figure 3.2c), the film diffraction pattern confirms the $(1\times 1)\text{MnO}(001)$ surface without the substrate spots. This LEED image has better quality than the other two because it has much more MnO film. Figure 3.3 exhibits the

LEED pictures for three energies (45 eV, 60 eV and 75 eV) to show the diffraction pattern evolution for the clean Au(111) substrate and for the surfaces (1×1)-Thick, (1×1)-Thin and c(2×2)-Island from the MnO(001) thin films.

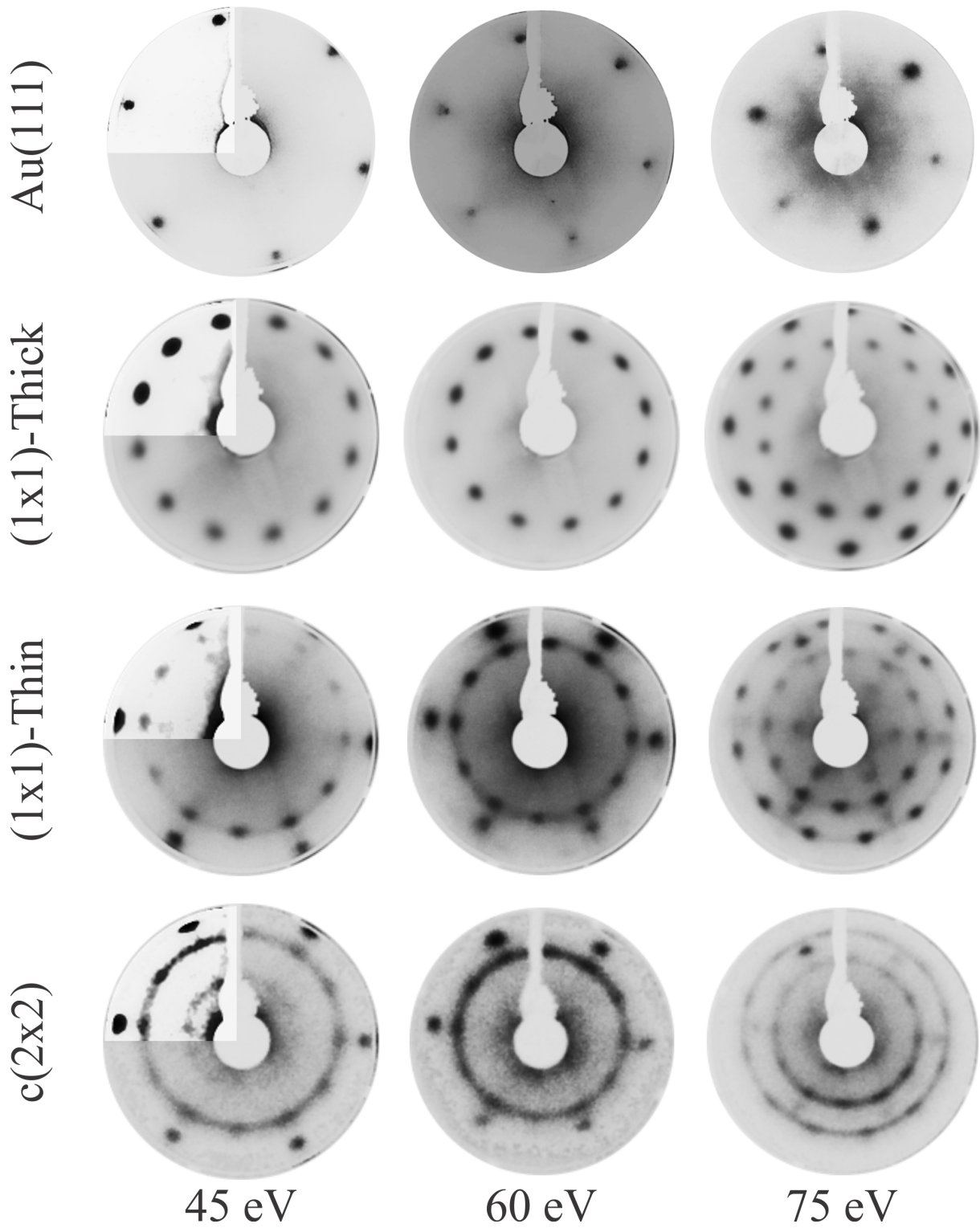


Figure 3.3: Series of LEED pictures for the Au(111) substrate and the surfaces (1×1)-Thick, (1×1)-Thin and c(2×2) from the MnO(001) thin film.

We characterized the atomic-level structure of the three MnO(001) thin films, and Figure 3.4 summarizes this data. Therefore, we aim to understand how these three distinct surfaces change the Mn 2p spectra line shape.

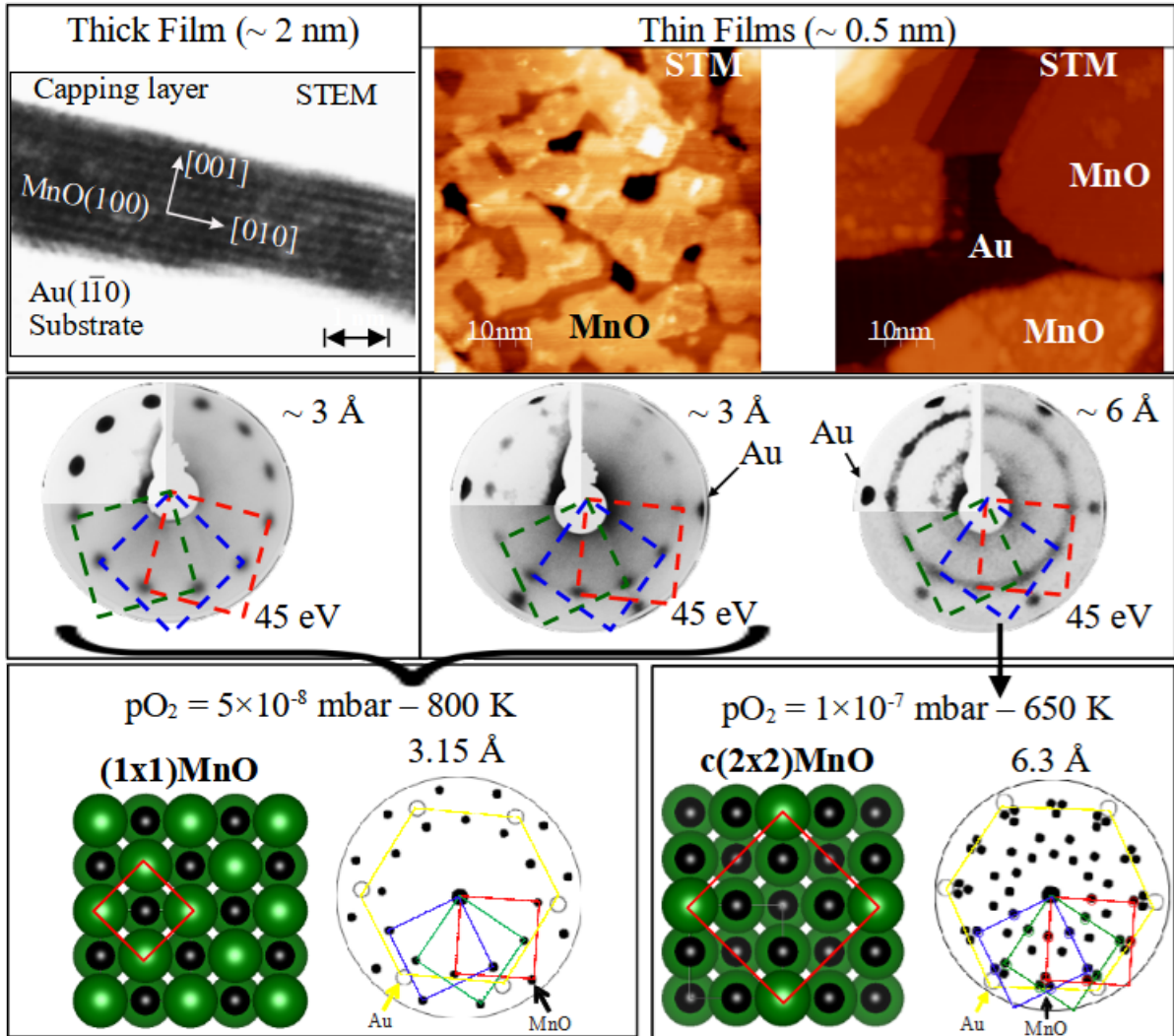


Figure 3.4: MnO(001) atomic-level structure of thick, thin, and island thin films observed with LEED, STEM, and STM techniques.

The Mn 2p spectrum for the MnO material is very typical, and the deconvolution theory is well established in literature [32]. On the other hand, it is always observed in the literature that the spectra shapes are slightly different, mainly the peak shape [68–71]. Markedly, the spectra of (1×1)-Thin and c(2×2)-Island are very different; these two spectra are compared in Figure 3.5. These two present the respective satellites from Mn²⁺ cations (distanced about 6 eV of each main peak), and the positions of the peak are expected for MnO (640.5 ± 0.5 eV for the Mn 2p_{3/2}) [72]. However, the line shape has differences, where the (1×1)-Thin most intense peak is at 640.2 eV and a second intense peak at 641.2 eV while for c(2×2)-Island the most intense peak is at 641.2 eV and has a shoulder at 640.2 eV. Note that the main peaks of c(2×2)-Island seems larger than the (1×1)-Thin. Figure 3.6 shows these two spectra fitted with the multiplet splitting theory (please see the section 2.2).

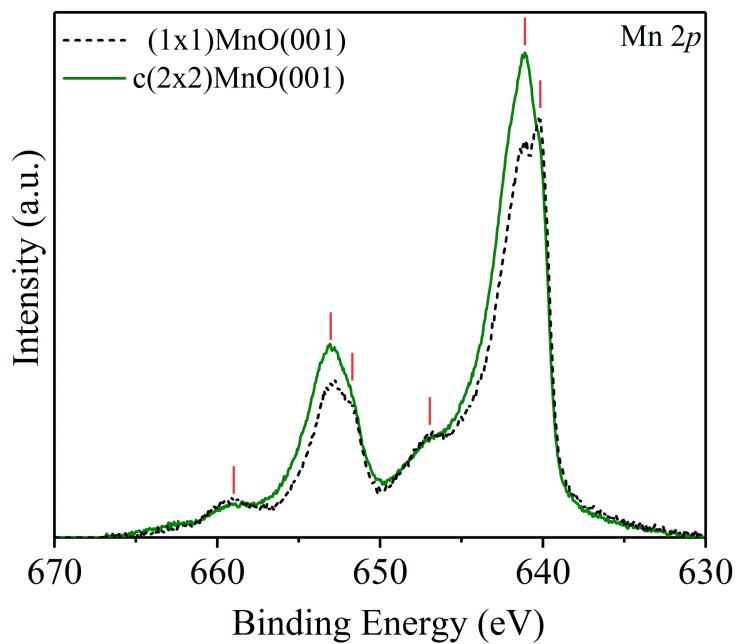


Figure 3.5: Two Mn 2p spectra, the black dash line is the (1×1)-Thin structure and the green continuous line is the c(2×2)-Island reconstruction.

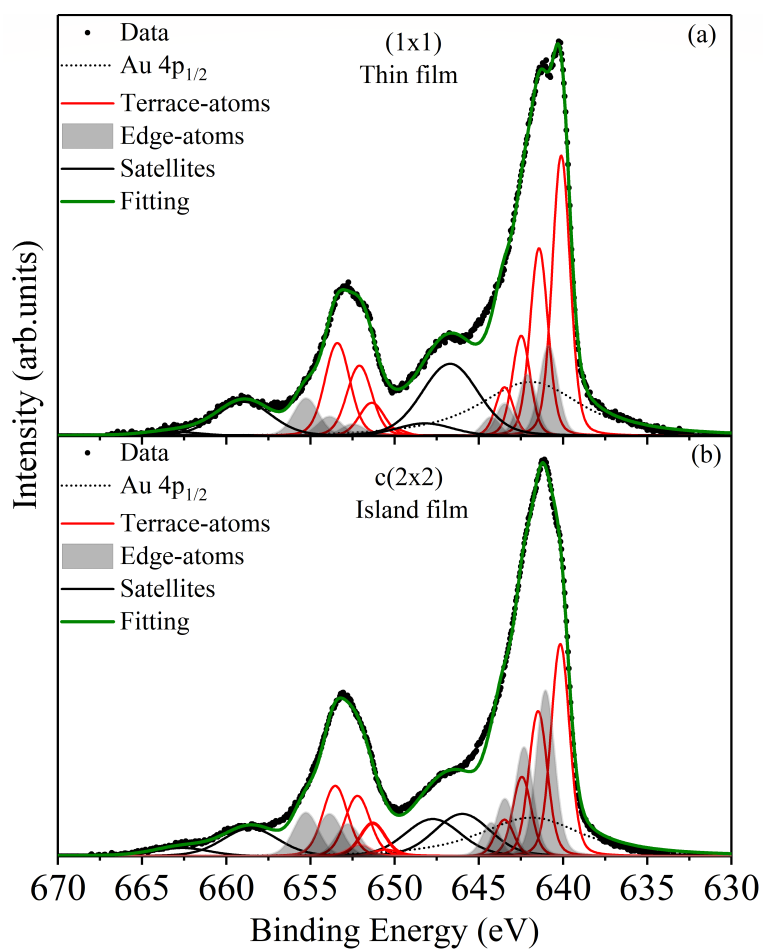


Figure 3.6: Mn 2p multiplet deconvolution for two different surface structure of MnO: (a) (1×1)-Thin and (b) c(2×2)-Island.

In principle, the fit can identify two groups: one is related to the terrace-atoms (ideally 5 nearest oxygen atoms) and the other to the edge-atoms (ideally 4 or less nearest oxygen atoms). On the first spectrum, (a), it is visible that the terrace components (red lines) are more intense than the edge components (gray areas). The terrace composes 70 % of the peak intensity, excluding the satellites. This difference in intensity is reduced in the (b) spectrum, where the terrace and edge have about 50 % each (see the values in Table 3.1). Therefore, the second film has much more edge-sites than the first, and two reasons should be considered: the surface reconstruction and the growth model. However, those two reasons may not be completely disconnected, where the $c(2\times 2)$ reconstruction could lead to growth in an island model. Since the components are associated with the variety of cation coordination sites on the surface, it is better to associate this with the growth mode because an island film of (1×1) surface will have more edge sites than the thin film.

The spectrum of (1×1) -Thick film can also be analyzed, and now a new site should be considered, intern-atoms (ideally 6 nearest oxygen atoms). Previously, the bulk-like were not considered because the two films were the surface majority (~ 0.5 nm of thickness). Even if there were some intern-atoms, this would be negligible. However, the intern-atoms will not be negligible for the (1×1) -Thick film due to its considerable thickness (~ 2 nm). Figure 3.7a shows the spectrum of Mn 2p from the thick film, fitted with three groups of multiplets, which represent the intern-atoms (blue and dashed line), terrace-atoms (red and solid line), and edge-atoms (gray filled area). The intern components compose the majority of the peak intensity (about 50 %), followed by the terrace (about 30 %) and edge (about 20%) components. It is not common sense to have twelve components inside a peak; however, it is necessary to fit the peak like that because this has a physical meaning. Following the theory [32], the positions do not change, and the group of components fits the spectrum well.

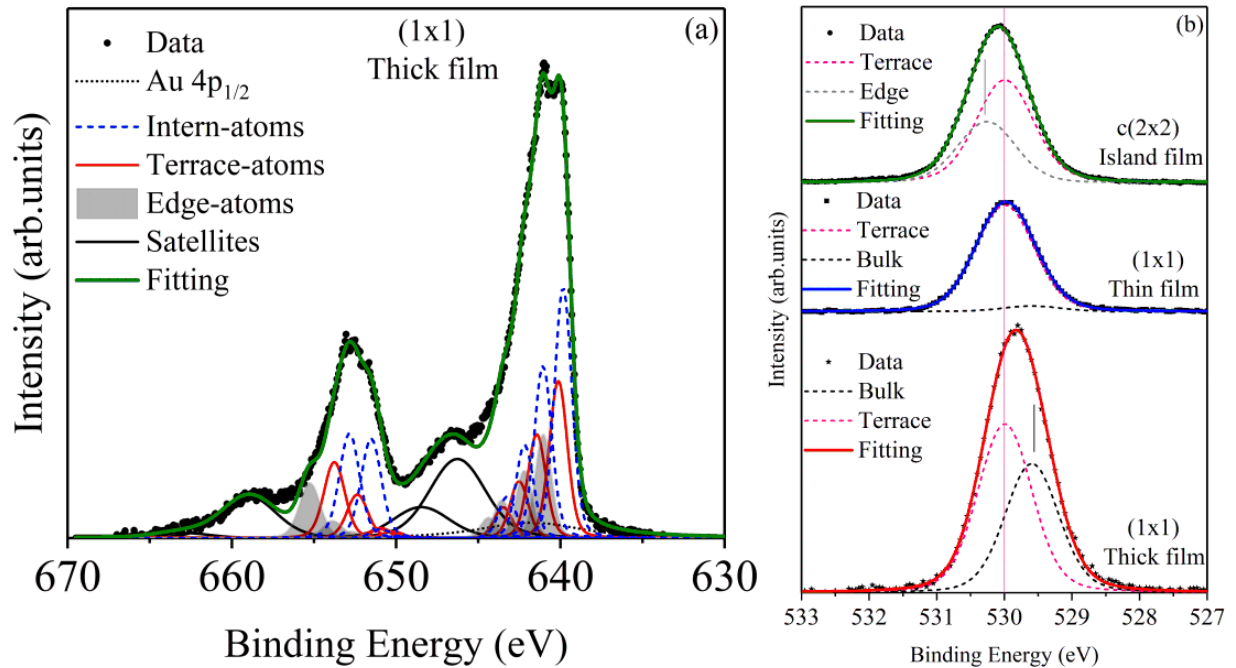


Figure 3.7: Mn 2p multiplet deconvolution for (a) (1×1) thick film and (b) O 1s peak deconvolution for the three films.

The same analyses can be done for the oxygen 1s, which should shift to the low binding energy. Figure 3.7b shows the fitting for the three O 1s spectra after subtracting the respective background (Shirley type). The binding energy expected for MnO material is 529.6 eV, which is indicated on the spectra as a black dashed component [73,74]. Another very expressive component is at 530.0 eV (pink component), and the island film presents a small peak at 530.25 eV. Those components cannot be from the CLS effect, and it is not even expected to observe the CLS effect for the O 1s spectra [66,67]. This effect comes from the charge movement of the O 2p orbital, which leads to an increase of binding energy that cancels the SCLS on ionic materials [66,67]. However, the MnO is not an ionic material, although it has a high ionic character [32]. The deformities in the orbitals are higher in the covalent material than in the ionic material. Hence, this charge movement will not just reduce the Madelung potential, as in ionic materials, but will create an effect that shifts the peak to the high binding energy. This effect is called closed-shell screen, which is responsible for the shifts to high binding energy on the O 1s spectra [32]. Therefore, the components inside were labeled as bulk (529.6 eV), terrace (530.0 eV), and edge (530.25 eV) due to the closed-shell screen for oxygen in different sites in the material.

Although controversy is observed, the terrace component is higher in the thicker film than the bulk component. While the CLS effect is related to the sites with more or fewer neighbor-atoms, the closed-shell screen is related to the movement of the electrons; hence not only the top-most layer will be counted as a terrace. Since the charge of the top-most layer is freer to move, the next layers will suffer a gradient in direction to the inside material. Also, the interface atoms will present a charge movement different from the bulk-like. Therefore the component intensity from the bulk-like should be lesser than the component of terrace-like.

Table 3.1 exhibits the fit experimental values of $2p_{3/2}$ and $2p_{1/2}$ peaks. Three groups of four multiplets are presented, which represent the intern-, terrace- and edge atoms. It shows for each multiplet its binding energy (BE) position, relative energy (E_{rel}), area (A), and relative intensity (I_{rel}). Where for each group, the multiplets have its E_{rel} calculated relative to the BE position of the first multiplet, at 0 eV. Area (A) was calculated, excluding the contributions of the satellite. The I_{rel} were calculated for each group relative to the first multiplet, which is 1. The multiplets of $2p_{3/2}$ peak were more restrictive as described at table 2.1, through the restrictions was fitted the $2p_{1/2}$ peak. The experimental results are similar to the expected theory for this peak, where two or three more intense multiplets fit the peak. In particular, the fourth multiplet has reduced intensity relative to the others. Since the ratio between the $2p_{1/2}$ by $2p_{3/2}$, for each group results in about 0.5, which is expected for p orbital, this should be a good deconvolution peak for the whole Mn $2p$. The total intensity for intern-, terrace- and edge atoms is in accordance with the analysis performed with microscopies.

Table 3.2 shows the values of O 1s peak fit. The three components were inserted into the peak, but the peak at 530.2 eV does not present any intensity for the (1×1) thick and thin. The peak at 529.6 eV presents nearly zero intensity for the c(2×2)-Island and (1×1)-Thin films.

Mn $2p_{3/2}$	(1x1)-Thick				(1x1)-Thin				c(2x2)-Island			
	Position	E_{rel}	A	I_{rel}	Position	E_{rel}	A	I_{rel}	Position	E_{rel}	A	I_{rel}
Intern	639.83	0	13.67	1								
	641.06	1.23	9.91	0.72								
	642.18	2.35	5.66	0.41								
	643.23	3.40	2.85	0.21								
Terrace	640.20	0	9.13	1	640.12	0	21.40	1	640.17	0	15.51	1
	641.49	1.29	6.34	0.69	641.44	1.32	14.88	0.70	641.49	1.32	11.08	0.71
	642.58	2.38	3.64	0.40	642.49	2.37	8.15	0.38	642.45	2.28	6.25	0.40
	643.49	3.29	1.89	0.21	643.49	3.37	4.03	0.19	643.49	3.32	2.95	0.19
Edge	641.08	0	5.53	1	640.87	0	7.29	1	641.06	0	12.50	1
	642.20	1.12	3.85	0.70	642.13	1.26	5.13	0.70	642.33	1.27	8.57	0.69
	643.57	2.49	2.18	0.39	643.47	2.60	2.76	0.38	643.46	2.40	4.64	0.37
	644.36	3.28	1.12	0.21	644.27	3.40	1.64	0.23	644.27	3.21	2.74	0.22
Intensities:	$I_I = 49.1\%$; $I_T = 31.7\%$; $I_E = 19.2\%$				$I_T = 73.8\%$; $I_E = 26.2\%$				$I_T = 56\%$; $I_E = 44\%$			
Mn $2p_{1/2}$	(1x1)-Thick				(1x1)-Thin				c(2x2)-Island			
	Position	E_{rel}	A	I_{rel}	Position	E_{rel}	A	I_{rel}	Position	E_{rel}	A	I_{rel}
Intern	652.92	0	8.37	1								
	651.62	-1.30	7.89	0.94								
	650.98	-1.94	0.63	0.07								
	650.54	-2.38	0.11	0.01								
Terrace	653.76	0	6.16	1	653.41	0	11.64	1	653.54	0	8.46	1
	652.36	-1.40	3.39	0.55	652.10	-1.31	8.68	0.75	652.22	-1.32	7.12	0.84
	651.00	-2.76	0.72	0.12	651.36	-2.05	4.08	0.35	651.30	-2.22	3.87	0.46
	650.56	-3.20	0.45	0.07	650.18	-3.23	0.96	0.08	650.53	-3.01	0.77	0.09
Edge	655.20	0	4.54	1	655.26	0	4.80	1	655.28	0	5.30	1
	653.86	-1.34	1.38	0.30	653.87	-1.39	2.46	0.51	653.88	-1.40	5.09	0.96
	652.73	-2.47	0.51	0.11	652.49	-2.77	1.50	0.31	652.80	-2.48	3.81	0.72
	651.80	-3.40	0.09	0.02	651.86	-3.40	0.61	0.13	652.08	-3.20	1.35	0.25
$p_{1/2}/p_{3/2}$	$I = 0.53$; $T = 0.51$; $E = 0.51$				$T = 0.52$; $E = 0.56$				$T = 0.56$; $E = 0.55$			

Table 3.1: Fit experimental values of $2p_{3/2}$ and $2p_{1/2}$ peaks. For each film is presented the total area of intern, terrace and edge components.

O 1s	(1x1)-Thick			(1x1)-Thin		c(2x2)-Island	
	Position	A	I_{rel}	A	I_{rel}	A	I_{rel}
Intern	529.6	238.2	0.75	151.3	0.03	29.2	0
Terrace	530.0	318.4	1	4312.1	1	4040.8	1
Edge	530.2					2757.7	0.68

Table 3.2: Fit experimental values of O 1s spectra for the thick, thin, and island films.

In Table 3.1, the BE position does not change significantly, so the three spectra can fit with the average BE position. Therefore, it is necessary to insert the three groups of components, intern-, terrace-, and edge-atoms, for the three films. Then, for simplicity, it will be fitted only the Mn $2p_{3/2}$ peak region (Figure 3.8). It also removed the Au $4p_{1/2}$ contribution for better visualization of the multiplets. Although the average intensity can be found, it is obtained a better fit with the 10 % constraint to adjust.

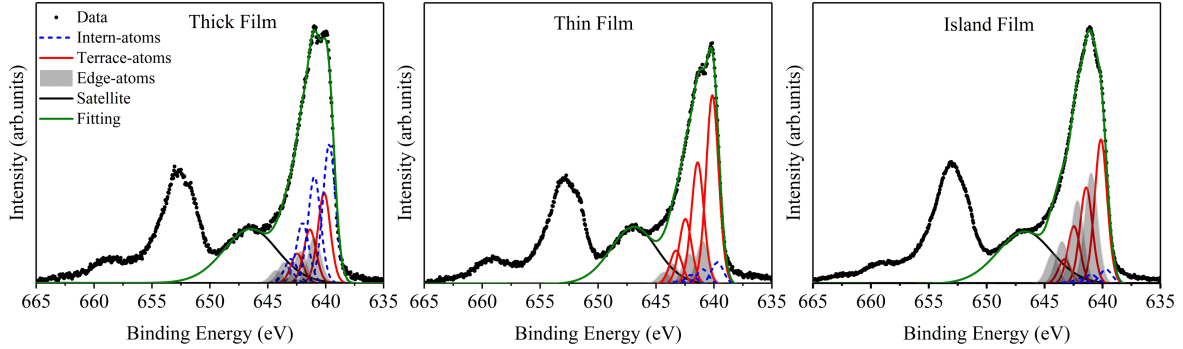


Figure 3.8: Mn $2p$ multiplet fit for the three films with the average BE position.

Table 3.3 shows the average of BE position, relative energy, and relative intensity (with $\pm 10\%$). The total contribution of each group, intern-, terrace-, and edge-atoms multiplet can be observed vertically for each film.

		FWHM (1.3 eV)			Thick	Thin	Island
		BE (eV)	E_r (eV)	I_r (%)	A (%)	A (%)	A (%)
Interior-atoms Multiplets		639.70	0	1	22.07	3.84	2.39
		640.98	1,28	0.71	16.96	2.63	1.57
		642.00	2,3	0.41	9.62	1.64	0.95
		643.00	3,3	0.16	3.89	0.59	0.36
		CLS = 0 eV (639.7 eV)				52.5	8.7
Terrace-atoms Multiplets		640.14	0	1	14.25	33.33	23.09
		641.41	1,21	0.69	8.47	21.51	15.44
		642.47	2,33	0.37	4.67	11.54	9.26
		643.28	3,14	0.18	2.43	5.97	3.97
		CLS = 0.44 eV				29.8	72.3
Edge-atoms Multiplets		640.98	0	1	7.34	7.70	17.86
		642.17	1,19	0.68	5.02	5.48	13.37
		643.50	2,58	0.42	3.30	3.62	6.82
		644.30	3,28	0.25	1.99	2.15	4.92
		CLS = 1.28 eV				17.70	19.0

Table 3.3: Fit experimental values of $2p_{3/2}$ peak with the average of BE positions, relative energy and relative intensity ($\pm 10\%$). The area, A, for each multiplet is present, at the end is presented the sum and the core-level shift is presented.

3.1.3 Conclusions

Three distinct MnO(001) films, grown on Au(111) single-crystal, were analyzed due to their different surface structure and morphology. These films were labeled as (1×1)-Thick, (1×1)-Thin and c(2×2)-Island. The crystalline structure of films was analyzed by LEED and microscopy techniques (STM and STEM). Then, it took advantage of these three distinct films to investigate their XPS spectrum line shape. The fit theory for Mn $2p_{3/2}$ peak is well established in the literature, but the $2p_{1/2}$ presents a more complex line shape [32]. Therefore, constraints were applied to the multiplets to perform the fit on the Mn $2p$ spectrum, and the theory's result was compared with the expected spectrum. Thus, the presence of relatively high quantities of cations at low coordination could be observed through the XPS spectra. Where the c(2×2)-Island film has more atoms at edge sites relative to the (1×1)-Thin film, it was possible to check this by Mn $2p$ fit peak. The (1×1) thick film is also relative to the thin, where the thick film presented new multiplets relative to the intern-Mn cations.

In summary, a precise fit of the Mn $2p$ peak evidenced the core-level binding energy shift (CLS) for different atomic coordination, namely intern-, terrace-, and edge-Mn cations. For the c(2×2)-Island spectrum, the edge- and terrace-components rise in equal intensity, while the (1×1)-Thin spectrum has the terrace components more intense than the edge components, about 75 % and 25 % respectively. The (1×1)-Thick spectrum exhibits the intensities about 50 %, 30 % and 20 % for intern-, terrace-, and edge-Mn cations respectively. To better illustrate, Figure 3.9 shows the microscopies images with the corresponding Mn $2p$ fitted where the intern-, terrace-, and edge-atoms are highlighted and indicated. Therefore, it is visible that the thick film, which contains mostly the inter-atoms (exhibited by STEM image), also presents the intern-components more intensely than the terrace- and edge- components. The same is observed for the MnO(001) thin and island films. The fit of the whole Mn $2p$ guaranteed that the ratio of $2p_{1/2}/2p_{3/2}$ was about 0.5 and also showed a good agreement with the expected relative intensity by the multiplet theory. This thesis shows that the CLS effect can explain the difference in the XPS Mn $2p$ line shape, and it was possible to perform the multiplet splitting fit of the whole Mn $2p$ spectrum. The peak fit shows that the BE position values for the Mn $2p$ are near a value. Therefore a peak fit was performed with the same average BE position for the three films, including the inter-atoms components for each spectrum. This show that the three Mn $2p$ spectra can be fitted with the same values of BE and intensity.

The oxygen $1s$ spectra were also analyzed, and it was expected by the CLS theory that the components shift to the lower binding energy. However, a slight shift is observed for high binding energy. Although the MnO has a strong ionic character, it is a covalent material, and the charge movement on this material is high enough to overcome the CLS effect. Thus, the shift is changed for high binding energy due to the core-shell screen, which describes this charge movement [32]. The Mn $2p$ and O $1s$ spectra agree regarding the amount of edge-, terrace- and intern-sites in each film presented. Since the films presented different quantities of edge and terrace sites on the surface, their surfaces should also present distinct chemical reactivity. Therefore, this study showed the relevance of characterizing the quantities of different sites on the surface of thin films with a rigorous analysis of the XPS spectrum. It should be possible to perform the same analyses on other metal oxides films and nanomaterials.

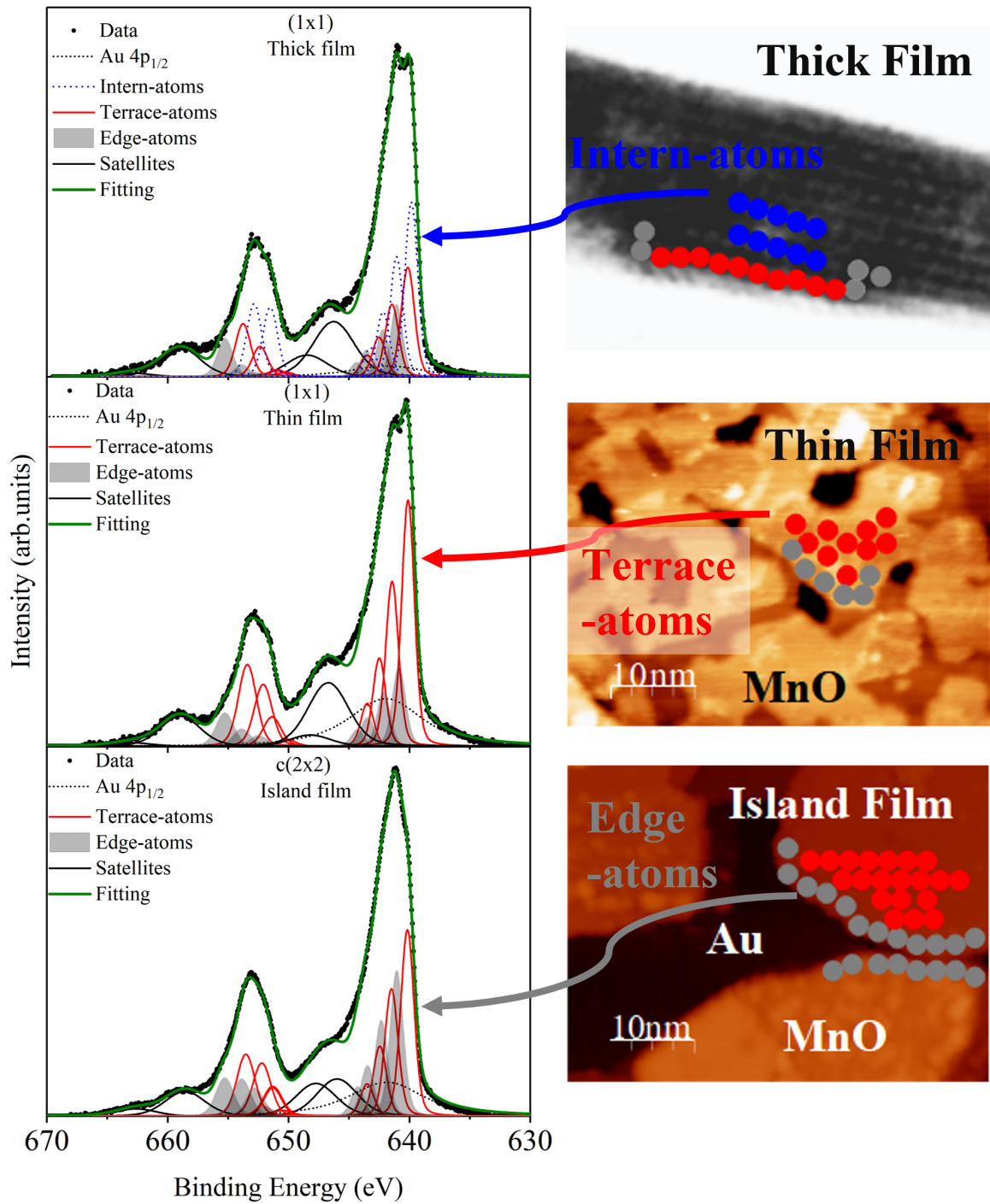


Figure 3.9: Mn $2p$ multiplet fit for thick, thin and island films with the corresponding microscopies images.

3.2 Chemical Reactivity of MnO(001) Thin Films

3.2.1 Introduction

Water and carbon monoxide (CO) interaction with metal oxide surfaces plays an important role in many fields, such as corrosion, water splitting, catalysis, and others [75,76]. Therefore, studies of water molecules' interaction with different oxides through the "surface science" approach are found in the literature [77]. For example, the oxides show distinct water adsorption behavior, such as the $\text{TiO}_2(110)$ [78] and $\text{ZnO}(1010)$ [79, 80] that dissociates the water molecules through the defects, while $\text{Cu}_2\text{O}(111)$ [81] does not dissociate the water molecules. It is also possible to adsorb water dissociated and not dissociated, as in the case of $\text{Co}_3\text{O}_4(111)$ [82, 83]. Studies with the density functional theory indicate that the water adsorption on MnO films is found to be dissociative [84]. In contrast, the CO adsorption has been employed as a probe molecule to understand the active sites on different oxide surfaces, such as the $\text{Fe}_3\text{O}_4(111)$ [85, 86], $\text{Co}_3\text{O}_4(111)$ [87], and MgO thin films [88, 89]. Furthermore, the MnO thin films grown onto Au(111) [17], Pt(111) [90], and Rh(100) [91] and probed by CO molecule show that depending on the surface structure, the film activates the carbon monoxide. It is known that the CO molecule intends to bind with the cation in perpendicular geometry, like Mn-C-O, which results in high-intensity peaks. When this molecule is bound to an angle with the surface normal, its intensity decrease then a map of the surface can be made [85–89].

For these reasons, we have examined the water (D_2O) and carbon monoxide (CO) interaction with MnO(001) films in order to understand their chemical reactivity. Where its molecular or dissociative nature, as well as the hydroxylation process, were examined. Whereas the MnO(001) surface dissociates the water through defects, and once hydroxylated, its water adsorption behavior changes to not dissociate the water. Then, the surface can only dissociate water after the sample temperature overpasses 550 K. Therefore, the experiments show a corrosion effect of water driven by rising temperature related to the film's crystalline structure. The CO research directs to the active sites of oxide structure, for which carbon monoxide adsorption also was revealed. We show that the CO adsorbs on the same sites as the D_2O , which helped to identify water in molecular and dissociated forms. Furthermore, CO and D_2O can be co-adsorbed to support our experimental findings on $\text{D}_2\text{O}/\text{MnO}$ and CO/MnO .

3.2.2 Results and Discussion

D_2O Molecule

We start our measurements with water (D_2O) adsorption behavior onto the Au(111) clean substrate. The adsorption behavior is investigated by coverage-dependent infrared spectra (Figure 3.10a). Continuous D_2O doses cover the surface, and at each dose, a peak at 2728 cm^{-1} increases its intensity until it is saturated. To understand the origin of this peak is necessary to know the mechanisms of water adsorption by Au(111) surface. In the literature, theoretical research concludes that the formation of water monomer on Au(111) is preferably at atop site with near-parallel orientation [92–95]. Furthermore, experimental investigations on FCC(111) surfaces show that the water monomers usually are absorbed in the atop sites [96–98]. Particularly on the Au(111) surface, studies of ice on its surface with scanning tunneling microscopy (STM) demonstrate that the for-

mation of monomers is favored. The D_2O molecules adsorb weakly on the elbows of the herringbone reconstruction [99–101]. Therefore, we assign this peak to an O-D stretching of D_2O monomers adsorbed on atop metal atoms, weakly bounded, and had a dangling O-D vibration (O_wD) [102, 103]. Besides that, as the monomers of free-OD stretching are on the surface, the peak intensity will reach the maximum when the whole surface is covered. After the peak reach the maximum, which occurs after the dose of 0.7 L, the signal-to-noise ratio of low wavenumber worst with doses increment. It happens due to the bound-OD stretch having a large band localized nearly about 2550 cm^{-1} , which is related to water bonds that increase with doses, without saturation, and indicate the formation of amorphous solid water (ASW) [76].

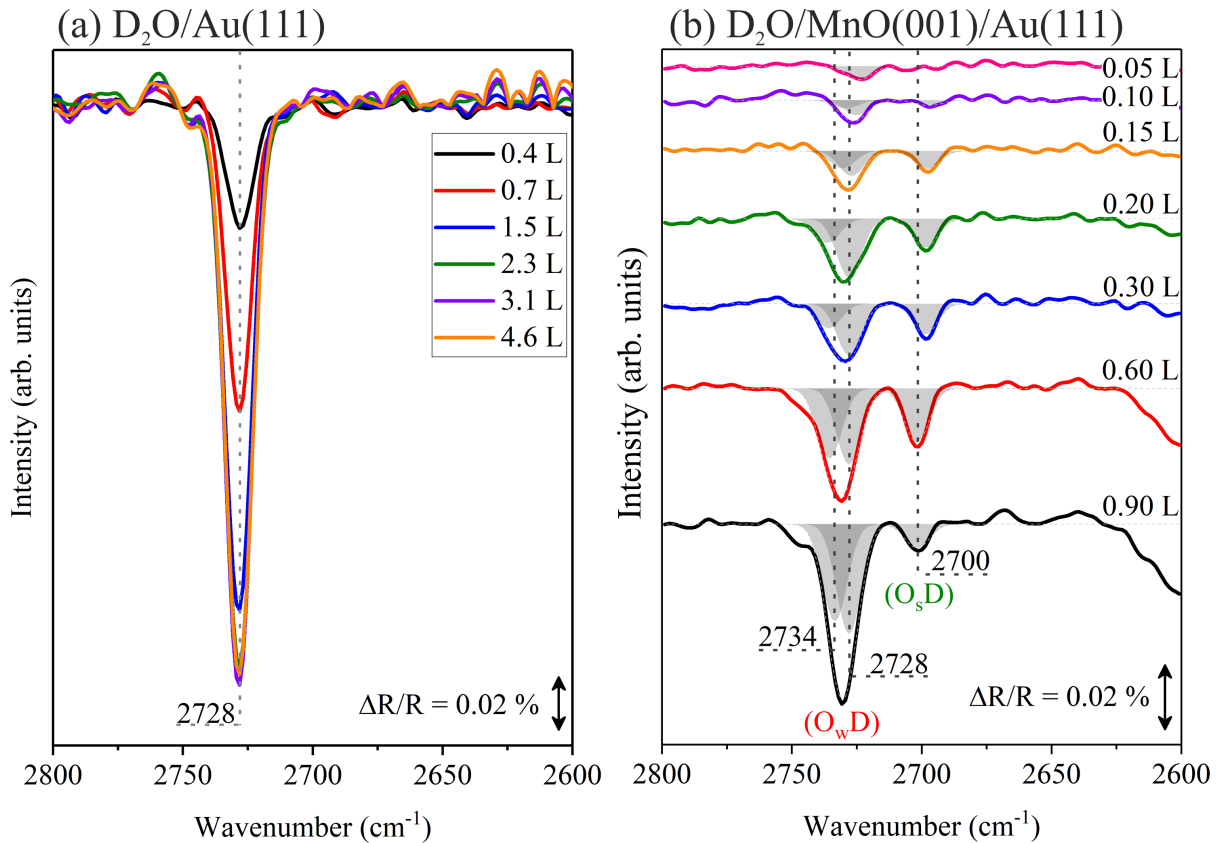


Figure 3.10: Coverage-dependence spectra of D_2O on (a) Au(111) surface and (b) MnO(001) thin film.

D_2O dosing was performed until 1 L exposure to avoid the significant formation of ASW on the film surface. Figure 3.10b exhibits the D_2O on MnO(001) thin film, where the spectra are presented with a vertical shift displacement to facilitate the analyses. Two peaks are visible at low coverage, at 2700 cm^{-1} and 2730 cm^{-1} . Therefore, a Gaussian fit was performed using a full width at half maximum (FWHM) component given by 5.6 cm^{-1} . Therefore, the 2730 cm^{-1} peak corresponds to two contributions, one at 2734 cm^{-1} and the other at 2728 cm^{-1} . The latter contribution is at the same wavenumber of D_2O on Au(111), then this peak is attributed to the exposed substrate. Since the formation of MnO film is obtained only at a low thickness, the film can uncover the substrate surface. Then the contribution at 2728 cm^{-1} is related to the substrate (Au- O_wD), and the other two (at 2734 cm^{-1} and 2700 cm^{-1}) are connected to manganese oxide film. The presence

of two vibration modes contributions in this region indicates that the film dissociates the water molecule. Then, the 2700 cm^{-1} peak can be attributed to the $\nu(O_sD)$, and the 2734 cm^{-1} peak to $\nu(O_wD)$, wherein the O_s is the oxygen from the surface and O_w is the oxygen from water [83, 104, 105]. Both 2730 cm^{-1} and 2700 cm^{-1} peaks grow nearly equally in intensity at low coverage, but the 2730 cm^{-1} gets more intense. Once the first doses fill surface defects later, the following doses will fill the whole surface until it is fully covered. Thus one can attribute the peak at 2700 cm^{-1} to be related to water adsorption at defective sites. While the 2730 cm^{-1} peak would be water adsorbed on the surface terrace, which should be intenser compared to the vibration mode related to the defects sites.

The $\nu(O_sD)$ and the $\nu(O_wD)$ show respectively a redshift and a blueshift as compared to the gas-phase frequency [106]. Due to the sample temperature (90 K), our reference is the frozen D_2O clusters at 2725 cm^{-1} , then the $\nu(O_sD)$ has a large redshift that can indicate a bound stronger than the $\nu(O_wD)$ [106, 107]. The water desorption analysis can perform the comparison between bounds, which one is the stronger. Figure 3.11a exhibits a spectra series that start with the spectrum of 0.3 L (D_2O) on $MnO(001)$, and the two following spectra were taken after a flash temperature until 150 K and post until 175 K. After that, the 2730 cm^{-1} peak fades, and the 2700 cm^{-1} remains. It reinforces that the 2700 cm^{-1} is related to $\nu(O_sD)$ and is stronger bounded than 2734 cm^{-1} , which is the $\nu(O_wD)$ species at the terrace surface sites. After raising the temperature to 200 K, the spectrum presents no peaks. Therefore, all the water molecules have evaporated from the surface. The temperature was raised until 230 K when again it was dosed. At this time, only the signal of $\nu(O_wD)$ appears in the spectrum. This same adsorption behavior is observed when repeating the experiment for temperatures of 350 K, 450 K, and 550 K. Interestingly, independent of the dosing being small or large, the prominent peak at 2700 cm^{-1} was not observed. After the surface temperature reached 650 K, a little intensity at 2700 cm^{-1} again was observed. This peak has its intensity enhanced after the surface temperature reaches 850 K. Nevertheless, the adsorption behavior is restored after sample annealing at a high temperature (800 K) in an environment of partial oxygen pressure (5×10^{-8} mbar), as observed by the last spectrum (red line).

Figure 3.11b exhibits an illustrated model proposed of what is happening. When the water desorbs from the surface, the vacancies change, that water dissociation is not possible anymore. Then it is suggested that the O_sD bond is not broken but leaves the surface, changing the electronic configuration of the vacancy with a new anion. Therefore, when again it is water dosed, the vacancies sites do not offer the proper chemical environment to promote the water dissociation. The surface can lose atoms and expose the next layer at high temperatures (over 550 K) in UHV conditions. That layer will have vacancies that can dissociate the water again, and the $\nu(O_sD)$ will be visible on the spectra. The annealing performed in partial oxygen pressure (about 5×10^{-8} mbar) recovers the absent oxygen atoms. Therefore, the 2734 cm^{-1} corresponds to the frequency of water intact molecule, labeled as $\nu(O_wD)$, since the surface can not dissociate but absorb D_2O monomers.

In the simplified ball model display in the Figure 3.11b, the blue and gray balls with arbitrary orientation represent the water dissociated ($\nu(O_wD)$ and $\nu(O_sD)$) and not-dissociated ($\nu(O_wD)$). A hydrogen atom can occupy a cation vacancy (as an example), while the remaining O_wD can be on the surface in a bound with manganese or surface

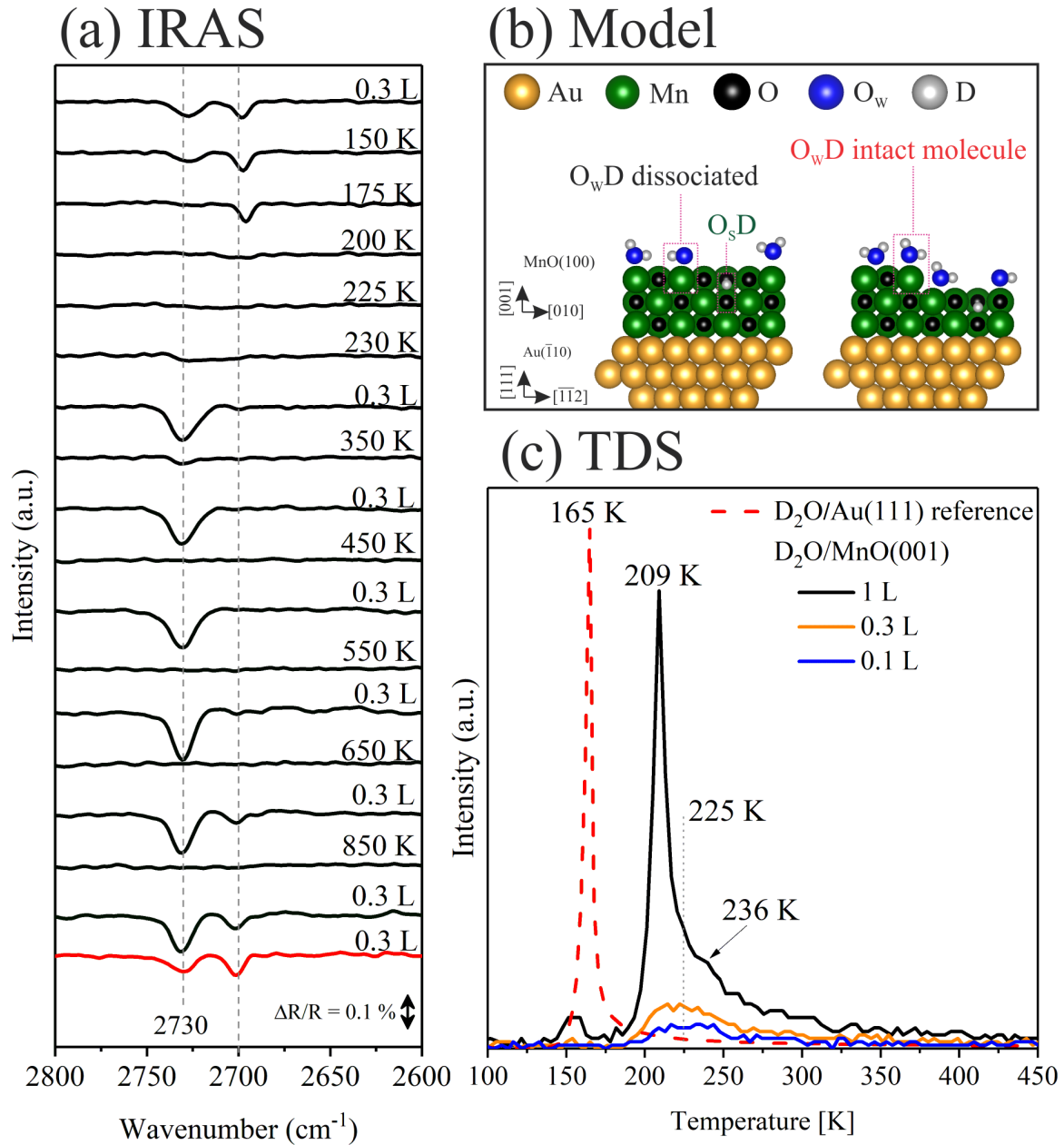


Figure 3.11: (a) IRAS spectra showing the temperature effect after D₂O dose on the MnO(001) thin film. (b) Illustration of interpretation with ball-model. (c) TDS measurement for three initial doses on the MnO(001)/Au(111) surface, and one dose on the Au(111) clean surface.

oxygen (O_s). After the sample is heated and dosed with water again, the vacancies of the latest layer will not be able to dissociate from the water. However, once the surface heats at a high temperature, which allows the loss of atoms, the below layer will have vacancies to enable the water to dissociate again. This model shows that the water performs corrosion in the film. Therefore, it identified three different species: The O_wD dangling bound from the water not dissociated, pointed on the spectra at 2734 cm⁻¹; the O_sD from the water dissociated at 2700 cm⁻¹; and the remaining O_wD from the water dissociated, not observed on the spectra. It is expected to have a peak for the $\nu(O_wD)$ of dissociated water but is also not observed on spectra for D₂O on the Co₃O₄ surface [83]. A possible explanation can be from the molecule orientation, where this species is more

parallel oriented to the surface and will present a weak intensity on the spectrum that is hardly identified [58, 108].

Figure 3.11c exhibit the TDS data for three D₂O exposure on MnO(001) surface, which are 1 L (black spectrum), 0.3 L (orange spectrum), and 0.1 L (blue spectrum). The reference peak presented (red dashed line) was performed through data of high D₂O exposure on Au(111) divided by a factor. The Au(111) surface has a desorption peak at 165 K, while the film presents a little peak at 160 K, an intense peak at 209 K, and a shoulder on the tail at 236 K. The desorption peak around 165 K matches the ASW temperature desorption [54]. The signal of bounds that forms the ASW on IRAS (dimers, trimers, ...) is more intense than the monomers bonded to the surface [76]. However, in the TDS data, this is a small peak. The reason is that the adsorptive factor depends on the orientation of the molecules for the IRAS, and this does not directly indicate the specific quantities [108]. The desorption peak starts after 200 K, at low coverage, and decreases to about 240 K (center peak at 225 K). The shoulder (at 1 L spectrum) and the spectra desorption trending, these common trailing edges, come from the second-order kinetics due to recombination desorption of dissociated water [109]. The desorption of Au(111) surface presents the first-order of desorption, which indicates a low surface interaction with the water. While the MnO surface presents the trending related to reactions on the surface, indicating that the oxide has a stronger interaction with water. The desorption peak, near 210 K, indicates how much the sample temperature needs to reach to break the binds, and new species can be formed, which are removed only after 236 K.

CO Molecule

Further adsorption experiment were performed using the CO molecule to probe the MnO(001) film surface. Figure 3.12a presents the CO coverage-dependence spectra, where one peak is blue-shifted (2174 cm⁻¹ - 2182 cm⁻¹) to the CO gas phase (2143 cm⁻¹), and the other is red-shifted (2120 cm⁻¹ - 2112 cm⁻¹) [110]. While the blueshift in CO stretch frequency is characteristic of CO adsorbed on the oxide surface, the redshift is characteristic of CO adsorbed on the metal surface [85, 87, 88]. Theoretical studies were performed for different systems to understand those shifts [111–113]. Studies attribute to the charge transfer donation and back donation between orbitals of CO molecule and the surface [113]. The electron donation is reasonable since the metal surface can be interpreted as a sea of electrons. Therefore, electron donation made from the Au(111) surface to the CO molecule weakens the CO bond and leads to a peak redshift. The peak at 2120 cm⁻¹ is characteristic of CO adsorption on Au(111), then it will be labeled as $\nu_{CO}(Au)$ and is 23 cm⁻¹ redshifted due to electron donation [114, 115]. Nevertheless, it will hardly be the same for the MnO(001) due to its stronger insulator character. The interaction between the surface electric field with the CO dipole moment (field-dipole interaction) and the Pauli repulsion, which appears when the CO molecule stretches (wall effect), explains the oxide surface [111, 112]. It was the case for research performed on materials with rock-salt structures such as MgO and transition metal oxides such as Co₃O₄ and Fe₃O₄ [85, 87, 88]. Therefore, it attributed to the peak at 2174 cm⁻¹, the CO molecule adsorbed in perpendicular geometry at Mn²⁺ cations, making the (Mn²⁺)-CO bond (labeled as $\nu_{CO}(Mn)$) and 31 cm⁻¹ blueshifted due to the wall effect.

While the $\nu_{CO}(Au)$ signal red-shift from 2120 cm⁻¹ to 2112 cm⁻¹ after 0.3 L CO

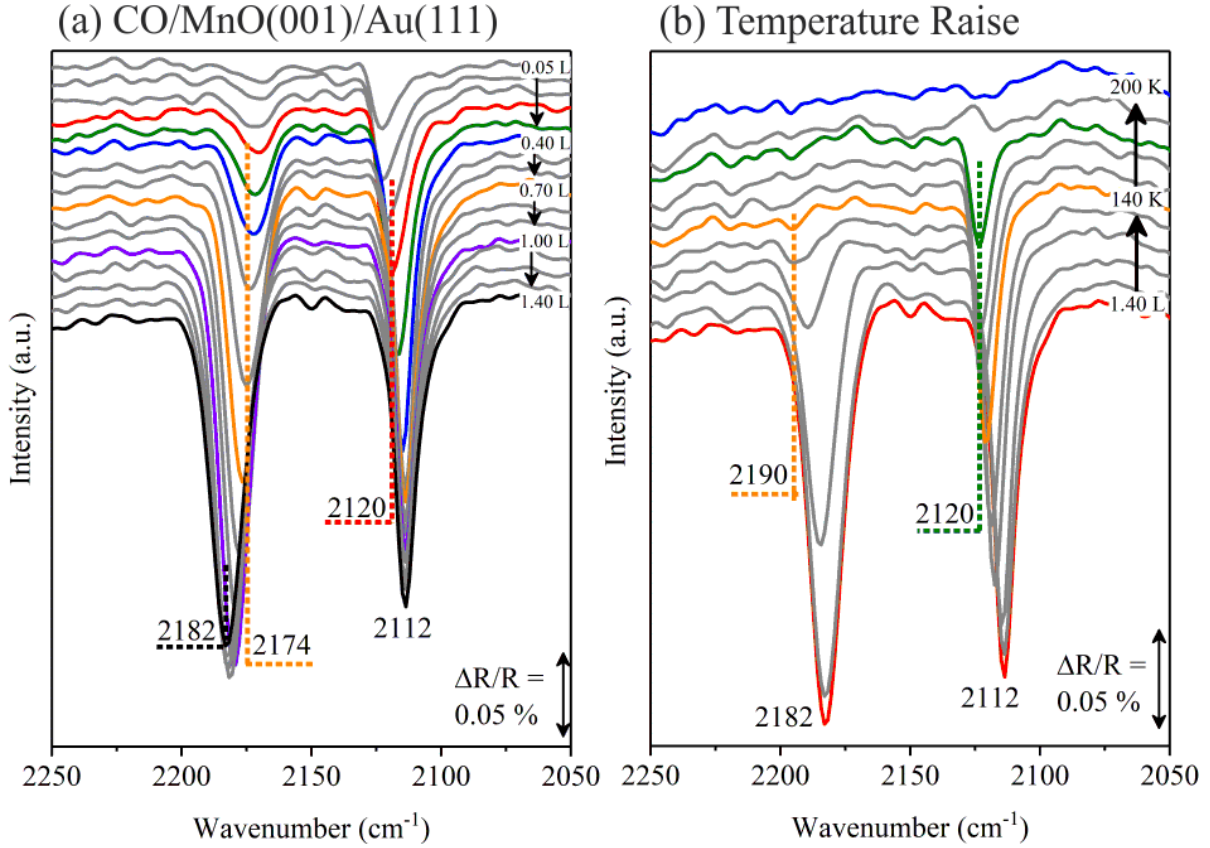


Figure 3.12: (a) CO Dosing from 0.05 L until 1.4 L. (b) Temperature rise from 100 K until 200 K.

dose, the $\nu_{CO}(Mn)$ signal blue-shift to 2182 cm^{-1} after 0.7 L dose. Both peaks have their intensity saturated after the complete shift. These shifts are due to the changes in the chemical environment when the surface is covered. On the Au(111) surface, it is attributed to the increase of CO molecule interactions, which start a competition for the charge coming from the metal surface. Interestingly, the shift for the oxide film occurs at a high frequency, which is unexpected because a shift to low frequency with the CO molecule interaction on oxide surfaces that own the rock-salt structure is observed [113]. This behavior can be attributed to the stronger MnO insulator character, which is expected to reach 3.5 eV bandgap. Therefore, it will be difficult for the CO receives a charge transfer from this film, so when all the surface was CO-covered, the dipole-dipole coupling made the peak blue shift again.

In our water adsorption experiments, about 1 L exposure covers the surface, and at this condition, layers of CO molecules will accumulate. Those numbers of when the shifts occur, 0.3 L for the substrate surface and 0.7 L for the film, can indicate that the exposed substrate surface is about 30 %. At low doses, the peak at 2120 cm^{-1} is higher than the 2174 cm^{-1} because the holes fill first. At 0.7 L, both peaks have about the same intensity because after filling the holes, CO layers will increase over the filled holes. Since the MnO film overgrew in large part of the substrate surface, the $\nu_{CO}(Mn)$ peak will have an intensity higher than the $\nu_{CO}(Au)$ signal after covering the whole surface. The change in the relation of intensity peaks happens after the 2174 cm^{-1} peak completely shifts to 2182 cm^{-1} , in agreement with our understanding. Please note that the CO bounds to

the Mn^{2+} atoms, hence, the CO peak on the MnO surface will be higher than the water dissociated.

After the 1.4 L of CO dosing, the sample temperature was increased step by step (Figure 3.12b). When it reaches 110 K, the 2182 cm^{-1} peak decreases its intensity and presents a shoulder at 2189 cm^{-1} . This peak completely shifts to 2189 cm^{-1} after 120 K, and its intensity reduces by 87 % and fades after 130 K. This blue shift of $\nu_{\text{CO}}(\text{Mn})$ is assigned to the field-dipole interaction, which changes with the temperature. The peak at 2112 cm^{-1} do not change before 120 K. At this temperature, the peak shift back to 2120 cm^{-1} and only fades after the temperature reaches 200 K. The metal surface act differently from the oxide. The blue shift can be attributed to the evaporation of some CO hence reducing the competition for the charge transfer.

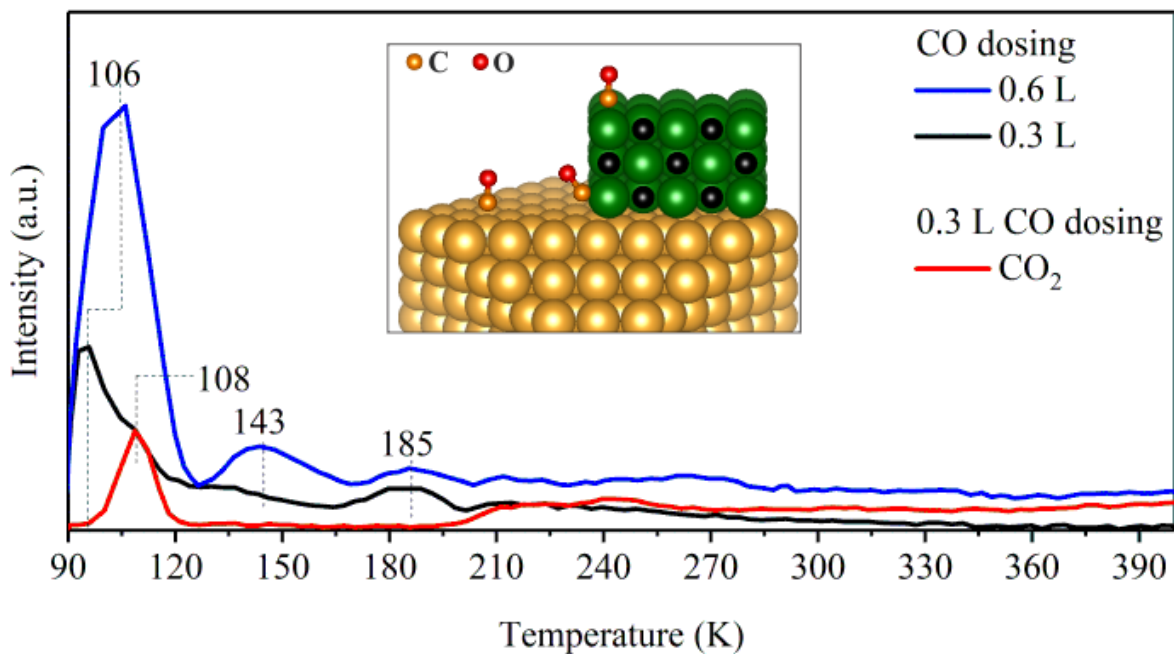


Figure 3.13: TDS data for two CO exposure on MnO(001) surface.

The TDS data (Figure 3.13) present the CO spectra for two doses, 0.3 L (black curve) and 0.6 L (blue curve), and the CO_2 spectrum for the 0.3 L of CO dose (red curve). The CO presents three sharp peaks centered at 106 K, 143 K, and 185 K. Two CO spectra present a trending too high-temperature characteristic of zero-order desorption from bulk water [53]. The first peak is composed of the evaporation of the CO molecules bounded to MnO film, $\nu_{\text{CO}}(\text{Mn})$, that, after reaching the maximum, still presents a tail that came from the evaporation after the blue-shift. Note that the infrared spectra refer to a high dose, 1.4 L, while the TDS refers to the desorption of two low doses, 0.6 L and 0.3 L. The first peak has the maximum peak, dependent on CO doses. At 0.3 L, the $\nu_{\text{CO}}(\text{Mn})$ observed is at 2174 cm^{-1} , and the 0.6 L is near the shift to 2182 cm^{-1} . The relatively intense CO_2 peak, at 108 K, indicates that the oxide surface activates the CO, as already observed by Li et al. (2021) [17], which assigned this conversion to the edge sites. Further temperature (200 K) show that the intensities of CO decrease and CO_2 increase, which is possible to relate to CO_2 molecules in the UHV chamber which increase with the temperature. The second and third peaks are composed of the evaporation of the CO

molecules bonded to the Au substrate, $\nu_{CO}(Au)$. The CO layers on the Au(111) surface start to evaporate after 120 K but only fades completely after 200 K. The first peak, at 143 K, can be attributed to the CO adsorbed on the middle of the Au(111) exposed and the second peak, at 185 K, can be from the CO adsorbed on edges with the MnO film [114]. That attribution is due to the expectation that the CO molecules on the edges with metal oxide surfer with a repulsion higher than the CO molecules on the middle Au surface.

CO and D₂O Co-Adsorption

Figure 3.14a shows the coverage spectra of D₂O on CO/MnO. The MnO surface was covered with a 0.05 L CO-dose. We expected that the CO molecules occupy the manganese cation hence preventing the water dissociation. As is observed with the D₂O doses, only the $\nu(O_wD)$ is visible on the spectra. When the surface heats to 850 K, all D₂O and CO molecules evaporate, then the surface can dissociate the water again. The last spectrum is the 0.25 L D₂O dose on the surface, and as well it is observed the $\nu(O_sD)$ that indicates the water dissociation. In agreement with the assignment of the peaks, the 2732 cm⁻¹ and the 2700 cm⁻¹ are from water intact molecule (O_wD) and water dissociated, respectively. Figure 3.14b shows the coverage spectra of CO on the D₂O/MnO surface. The surface was covered with a 0.15 L D₂O-dose, the CO peak associated with manganese oxide, $\nu_{CO}(Mn)$, presents a very low intensity compared to the $\nu_{CO}(Au)$. Hence, the D₂O/MnO surface does not favor CO adsorption as a previous MnO surface. The CO will prefer to bind with the metallic substrate to obtain the charge donation.

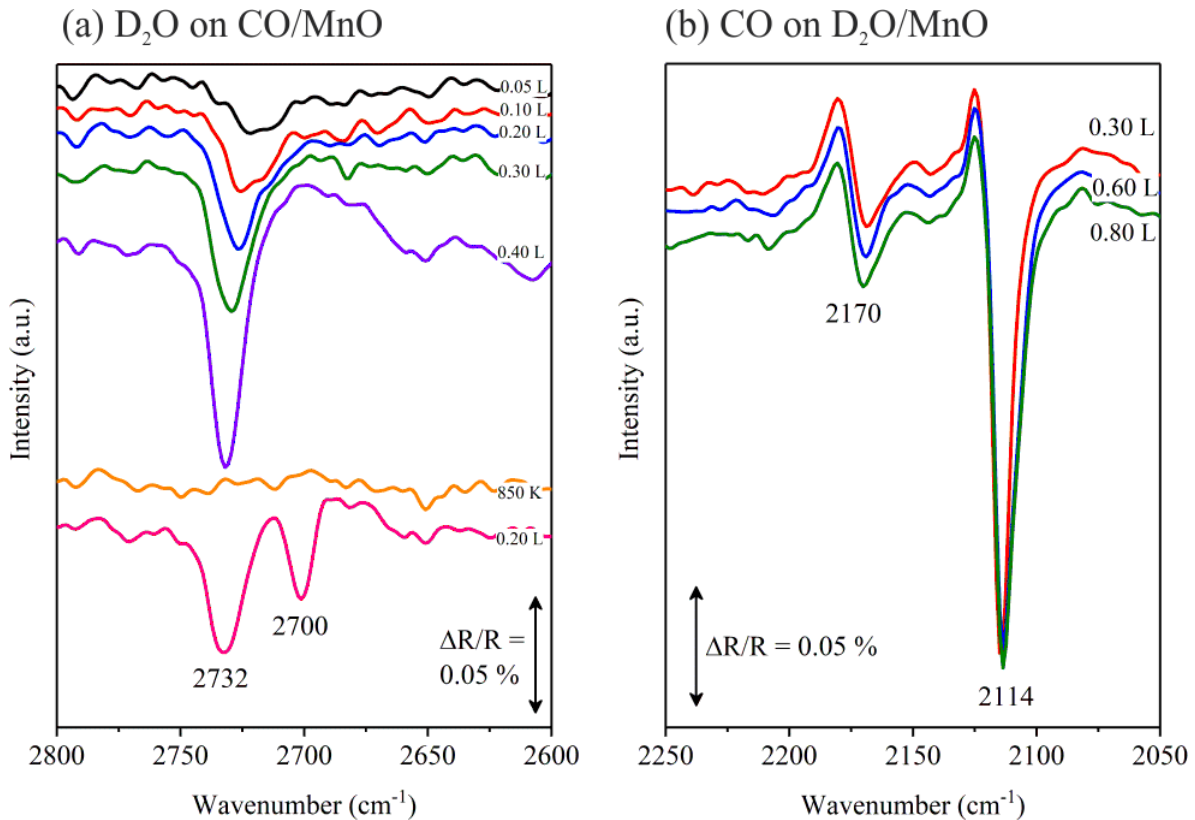


Figure 3.14: Co-adsorption of (a)D₂O on CO/MnO. (b) CO on D₂O/MnO.

3.2.3 Conclusions

Experiments with D_2O and CO molecules were performed on films of MnO(001) grown on Au(111) substrate. The MnO surface dissociates the water through vacancies, showing that the film interacts more with water than the Au(111) surface, but this is still a little interaction. The dissociated peak is attributed to the bound of the oxygen surface with the hydrogen of water broken molecule (O_sD). In contrast, the not-dissociated peak was attributed to a water monomer with a dangling bound (O_wD) on the surface. The O_sD species is strong, and after 200 K, that species leave the surface with anions vacancy. This hydroxylated MnO has a water adsorption behavior different from the pristine surface, i. e. cannot dissociate the water molecules. The CO adsorption experiments show that the oxide film can convert part of the CO molecule into CO_2 . It also shows that the CO bound to the middle of the substrate surface differs from the CO bounded nearly MnO film. Once the CO peak is very high, the MnO surface can be identified as terminated with Mn-O atoms in alternity. The adsorption of D_2O on the CO/MnO surface shows that the water does not dissociate on a surface rich in oxygen atoms. Once the CO bands present high intensity, they bind to the cation like Mn-C-O, making the termination rich in oxygen atoms. Since all the cations are occupied with a CO bond, the water molecules are not dissociated. Furthermore, the adsorption of CO on the D_2O /MnO surface shows that the CO molecules adsorb by the exposed metal surface than the oxide partially filled by water.

3.3 Probing Surface Structure of $\text{Mn}_3\text{O}_4(001)$ Film with CO and D_2O Adsorptions

3.3.1 Introduction

This section explores the structure of Mn_3O_4 thin films and their chemical reactivity with water (D_2O) and carbon monoxide (CO) molecules. The Mn_3O_4 is a spinel composed of a cation mix at tetrahedral (Mn^{2+}) and octahedral (Mn^{3+}) coordination. Therefore, it is relevant to investigate its structure to understand its water and carbon monoxide adsorption behavior as a catalyst model. Then, Mn_3O_4 thin films were grown on Au(111) [21, 42] substrate to probe its surface adsorption behavior with CO and D_2O molecules. XPS Mn 2p spectrum confirms its oxidation state, and its structure is analyzed using a combined techniques. Whereas the LEED measurements provides the first insights into the film structure, and further information is obtained through images of the STEM technique. Finally, the CO adsorption experiment can support the film structure interpretation. In literature, this molecule is commonly applied to probe the surface structure of oxide films [86] since its weak interaction energies and various modes of interaction can provide information about the nature of surface coordination sites [116].

3.3.2 Results and Discussion

Figure 3.15 show the Mn 2p peak of Mn_3O_4 , which is a complex spectrum due to the presence of two cations. In general, the $2p_{3/2}$ peak is composed of an asymmetry with a binding energy at 641.7 eV, a satellite peak at 663 eV and the spin-orbit splitting of 11.8 eV. A forward step will be attempted in this thesis to fit the whole Mn 2p peak.

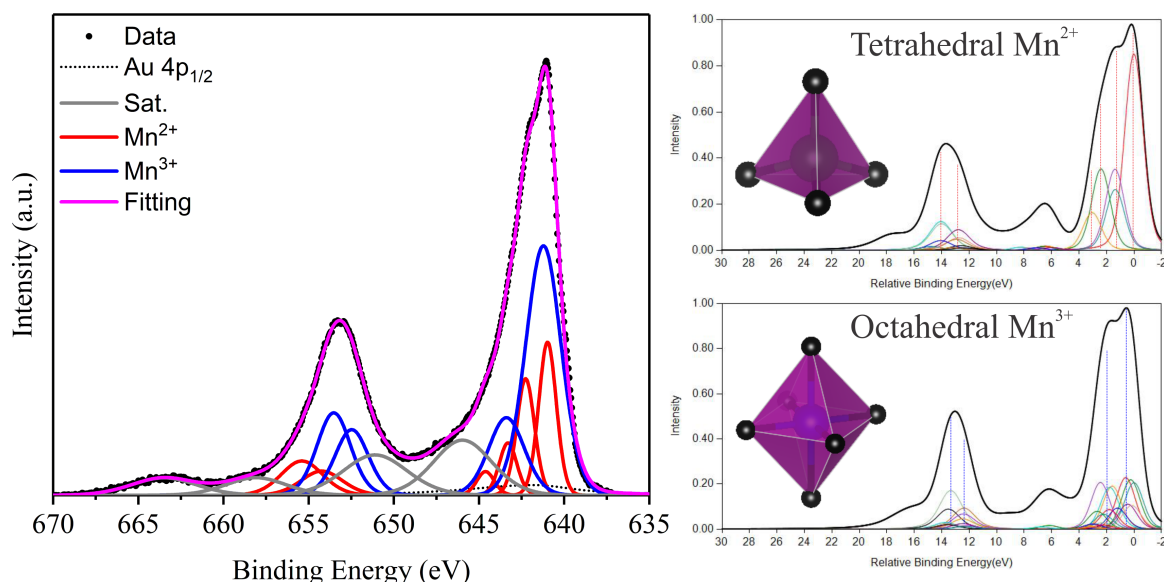


Figure 3.15: XPS fitting of Mn 2p spectrum and the calculations for the Mn^{2+} and the Mn^{3+} cations (Calculations performed by Prof. Dr. Paul Bagus).

Theoretical calculations for the Mn^{2+} and the Mn^{3+} cations were performed by Prof. Dr. Paul Bagus from the University of North Texas (UNT), and it will be used to fit the Mn 2p spectrum. In the calculations were considered the manganese-oxygen distance and

its coordination, this can change the multiplets inside the peak [32]. Although the Mn^{2+} cation changes the coordination, and the Mn-O distance is 0.33 Å shorter, its components are similar to those obtained for the MnO material. In the experimental data, red components represent these multiplets. The multiplet contributions for the Mn^{3+} cations are two with relative energy near 2 eV, and blue components represent these multiplets. Combining the components from the Mn^{2+} and Mn^{3+} results in the peak asymmetry. Such asymmetry is not present on the Mn_2O_3 spectrum, which is composed only with Mn^{3+} cations [117]. The fit ensures that the ratio of $\text{Mn}^{2+}/\text{Mn}^{3+}$ and the $2p_{1/2}/2p_{3/2}$ be 0.5. Both satellites contributions are fixed positions and intensities, indicated as gray contributions.

Figure 3.16 shows a LEED pattern of Mn_3O_4 film by the side of the diffraction pattern simulation [45]. The LEED picture (at 40 eV) exhibits three circles of twelve spots interpreted as a square lattice with three domains rotated, as indicated by the three colored squares. A lattice parameter of 5.76 Å with three domains rotated by 60° was applied to perform the simulation, which matches the diffraction pattern observed. Although the (001) plane of Mn_3O_4 has two possible symmetries, a square (5.76 Å) and a rectangle (5.76 Å \times 2.88 Å), the sum of both symmetries results in this same diffraction pattern, it used the square to perform the LEED simulation for simplicity. Therefore, the film grown was $\text{Mn}_3\text{O}_4(001)$, and other directions were considered and discarded as a possibility [31].

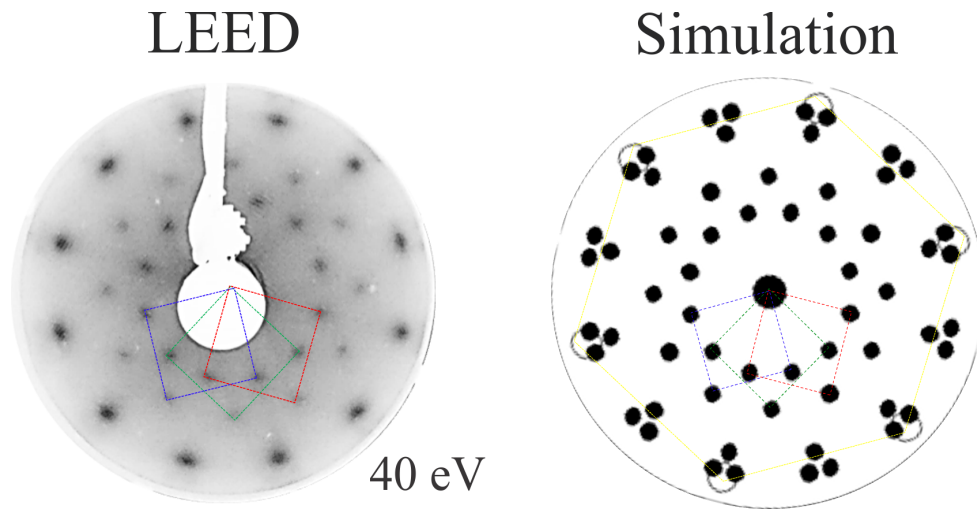


Figure 3.16: Diffraction pattern (at 40 eV) of $\text{Mn}_3\text{O}_4(001)/\text{Au}(111)$ by the side of the diffraction pattern simulation.

Further structure characterization is performed by STEM images presented in Figure 3.17, the images were obtained by Maria Ramos collaborator from INMETRO and the interpretation were performed by this thesis. Both images show respectively the $\text{Au}(1\bar{1}0)$, Mn_3O_4 film, and the cape of metallic gold particles. Two distinct domains could be identified, the first structure shows spots very intense that perform a hexagon symmetry, inside that hexagon has ten spots with a minor intensity. This symmetry was already observed for a Mn_3O_4 thin film grown on $\text{Cu}(111)$ substrate [29]. In the second domain, the intense spots are spaced in rows and separated by continuous lines. Below the STEM images, the Mn_3O_4 ideal structure is presented to explain those two domains. On the Mn_3O_4 cell, some columns contain relatively more atoms than others, those columns were selected

(yellow cross). Since those columns have more atoms, they should contribute with higher intensity to the STEM image. The plane (100), without rotation, has columns with more relative atoms that perform a hexagon symmetry with ten atoms inside. In the STEM image, the spots are highlighted with the related colors of the plane to show that the image matches the $\text{Mn}_3\text{O}_4(100)$.

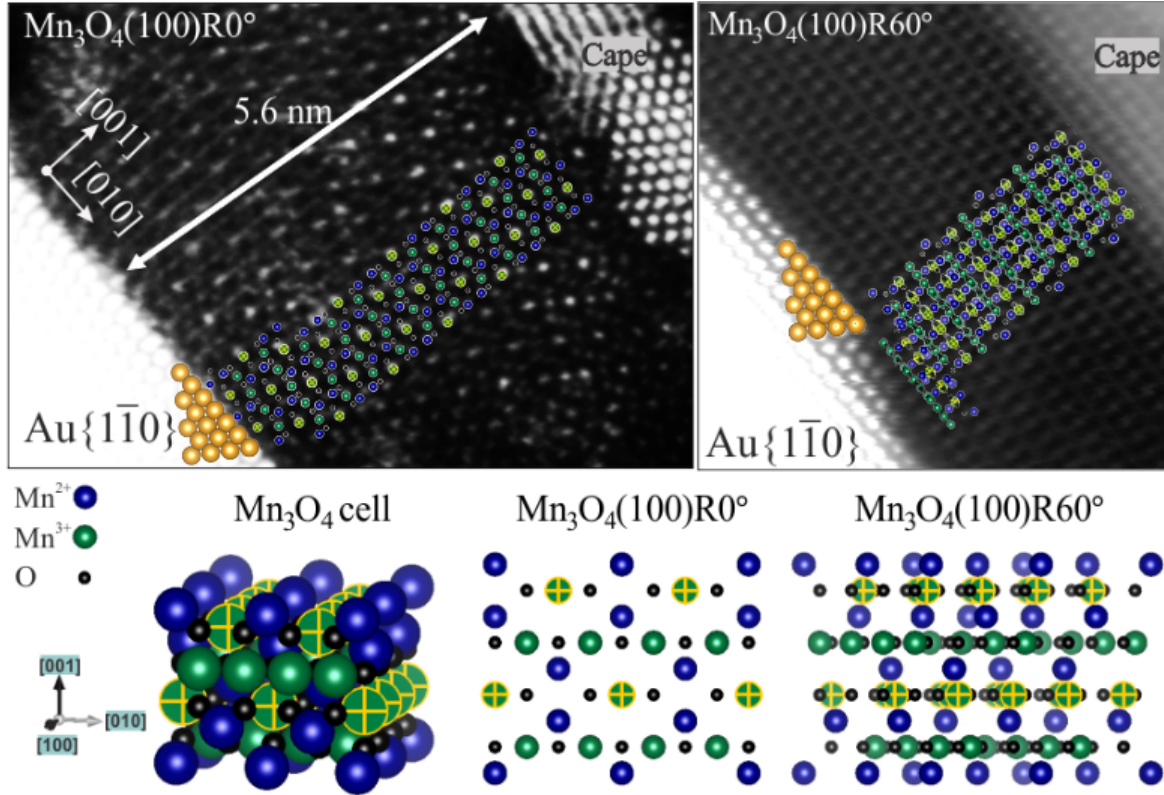


Figure 3.17: STEM images of two domains from the same Mn_3O_4 film. The first domain is the $\text{Mn}_3\text{O}_4(100)$ without rotation and the second is the plane rotated by 60° , as presented by the ball-models below the two STEM images. STEM images obtained by Maria Ramos (INMETRO), and interpreted by this thesis.

From the interface until the top surface was not observed a reconstruction of the film, which can be seen as the truncated bulk material. It is hard to determine the film start-layer with the interface, which can be the square (Mn^{2+} layer) or the rectangle (Mn^{3+} layer). However, the rectangle is preferable through the DFT calculations [41] and due to the lattice mismatch, $a_{\text{Au}} = 2.88 \text{ \AA}$ and $(a \times b)_{\text{Mn}^{3+}} = (5.76 \text{ \AA} \times 2.88 \text{ \AA})$ [21]. A rotation of the (100) plane by 60° will lead to a structure of rows with intense columns well-spaced each other, in the middle of those rows are layers of atoms spread which leads to continuous lines on the image. The position and the distances match very well with the model, again it is hard to be assertive about the interface and film termination. The image matches with the $\text{Mn}_3\text{O}_4(100)\text{R}60^\circ$ hence the second domain is the (100) plane rotated by 60° . Both domains agree with LEED data, which indicates that the film is growing on top of Au(111) at [001] direction with three domains rotated. Where the film domains are aligned with the $\langle 1\bar{1}0 \rangle$ equivalent directions of Au(111) lattice.

Probing the surface with CO molecule

Figure 3.18a presents the CO coverage-dependent spectra for the region from 2200 cm^{-1} until 2000 cm^{-1} , where a positive (2109 cm^{-1}) and a negative (2140 cm^{-1}) peak are observed. A new peak at 2102 cm^{-1} appears on the spectra with the CO exposures. The CO dosing ranged from 0.003 L to 49 L while keeping the sample below 110 K . During the sample cooling, molecules of CO residual inside the chamber can move to the sample surface. While obtaining the background, for 10 min , the start point will contain these molecules, which are mobile and can leave the surface over time. Therefore, the positive peak indicates that some CO residuals were on the surface during the background but were not there when the CO doses started. Note that the positive peak (2109 cm^{-1}) is near the new peak (2102 cm^{-1}), and its intensity decreases with the increase of 2102 cm^{-1} peak. Therefore, the real wavenumber position of the new peak may be a little higher than the observed one, and both peaks may represent the same adsorption sites. While the negative peak of CO (2140 cm^{-1}) has a position near the CO gas phase (2143 cm^{-1}), which indicates that these CO molecules are free on the oxide surface.

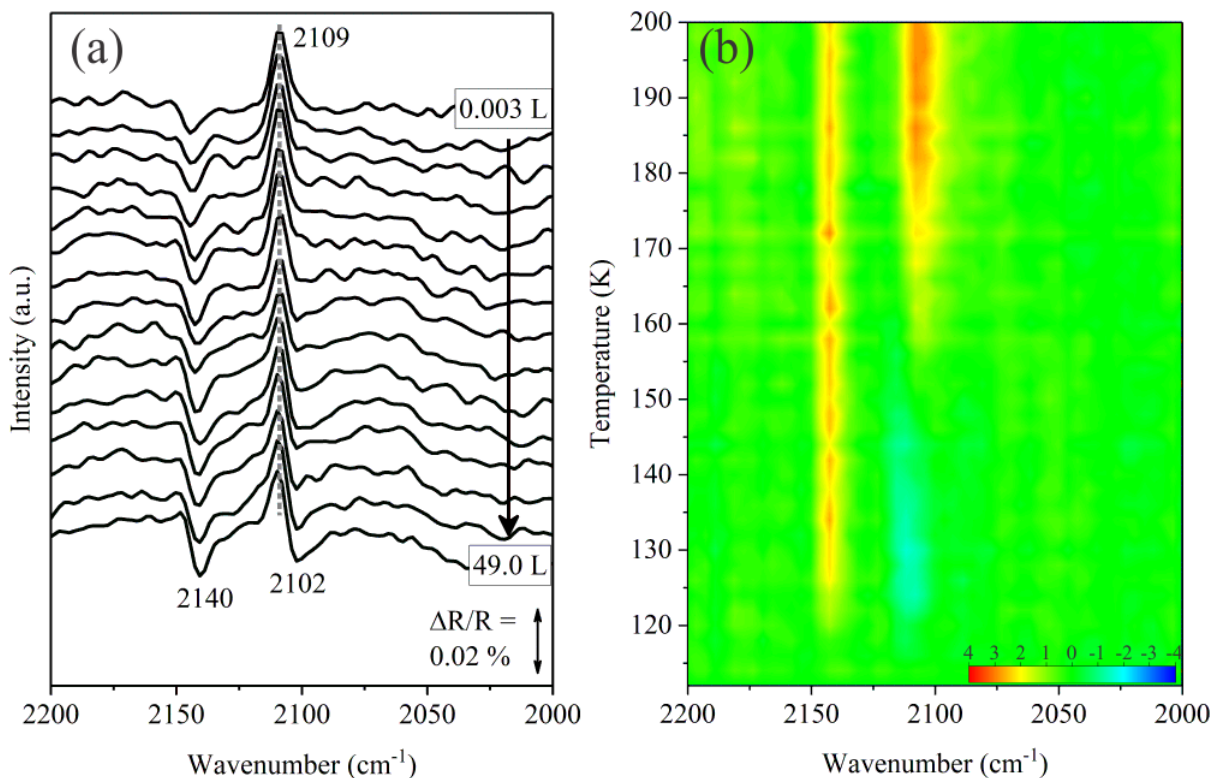


Figure 3.18: (a) IRAS spectra ($2200\text{ cm}^{-1} - 2000\text{ cm}^{-1}$) of CO coverage from 0.003 L until 49 L and (b) TP-IRAS color plot from 112 K until 200 K with step of 2 K .

Surprisingly, the CO adsorption on Mn_3O_4 appears to be rather weak. This behavior contrast to similar spinel mixed cation material such as the Co_3O_4 and Fe_3O_4 [86, 87]. For example, the Co_3O_4 shows a very stronger interaction with CO molecules adsorbed on the Co^{2+} cations. Notable, the Fe_3O_4 shows distinct interactions with both cations (Fe^{2+} and Fe^{3+}). Therefore, a surface terminated with the cations (Mn^{2+} or Mn^{3+}) should have a stronger intensity once the CO binding in a perpendicular geometry with the cations [86, 87]. When the CO has bound, its wavenumber position shifts due to the

interaction with the cation from the surface. Thus, it is likely that the Mn_3O_4 film surface termination oxygen rich, which does not favor CO adsorption [90]. Accordingly, the $\text{Mn}_3\text{O}_4(001)$ terminated with stripes of Mn^{3+} cations that have the whole oxygen atoms of the octahedral sites [21]. Therefore, the peak at 2140 cm^{-1} is CO gas mobile on the $\text{Mn}_3\text{O}_4(001)$ surface.

Figure 3.18b shows the color plot of TP-IRAS obtained from 112 K until 600 K, with steps of 2 K. However, all the molecules had evaporated from the surface after 200 K. Therefore, the color plot displays only until this temperature. On the figure scale, the closer to red indicates evaporation of species, and the closer to blue indicates adsorbed species. The peak at 2140 cm^{-1} leaves the surface after a slight temperature increase up to 125 K. It agrees with the interpretation that it is a mobile molecule on the surface. Once a small temperature rise is enough to remove these molecules. The low intensity observed at 2109 cm^{-1} indicates CO adsorption during the exposures. About 170 K new species have evaporated, and the wavenumber position is at 2106 cm^{-1} . It indicates that the peaks at 2109 cm^{-1} and at 2102 cm^{-1} represent the same CO adsorption site.

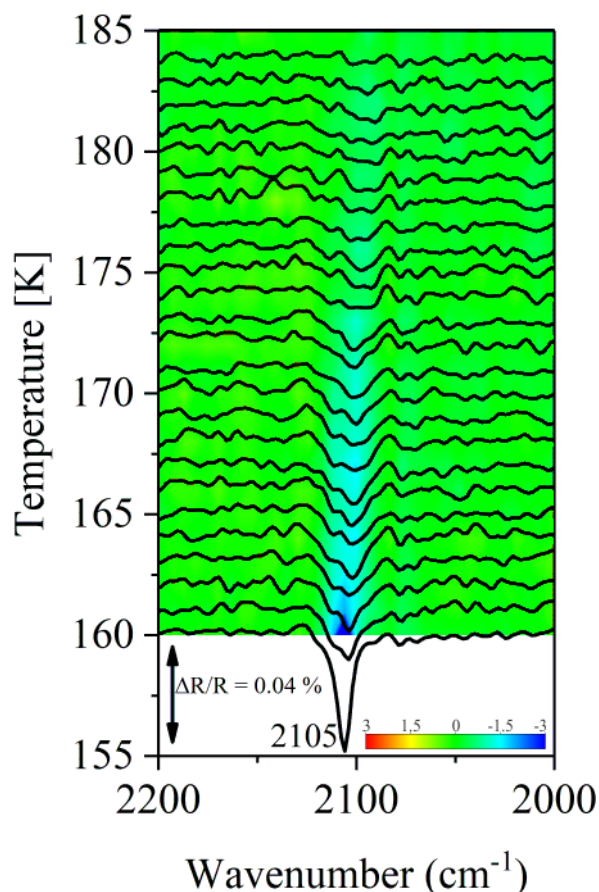


Figure 3.19: TP-IRAS spectra ($2200\text{ cm}^{-1} - 2000\text{ cm}^{-1}$) from 160 K until 185 K of the oxide surface with CO partial pressure of 5×10^{-8} mbar.

For analyses of this CO adsorption site, around the 2100 cm^{-1} region, a different experiment is presented in Figure 3.19. The TP-IRAS spectra were acquired while the chamber was filled with a CO partial pressure of 5×10^{-8} mbar and had a start point at 160 K. The peak appeared at 2105 cm^{-1} , and CO molecules did not adsorb above the 175 K sample

temperature. While the peak at 2140 cm^{-1} is free on the surface, the peak at 2105 cm^{-1} adsorbs on the oxygen holes at Mn^{3+} cations, which results in a stronger bond (about 38 cm^{-1} shifted to the CO gas phase). This red-shift is characteristic of electron donation from the 3d orbital to the bond of C-O hence weakening this bond [113]. Therefore, it attributed this peak (2105 cm^{-1}) to the bond with the Mn^{3+} cations because these cations are in octahedral coordination. The CO adsorbed on Fe_3O_4 film presents a red-shifted peak, near the 2100 cm^{-1} , for the cations at octahedral sites on the oxide [86]. While it attributes a blue-shift peak to the CO bound to the cations at tetrahedral sites. For the iron oxide blue shift to 2207 cm^{-1} and about 2174 cm^{-1} for the cobalt oxide [86,87].

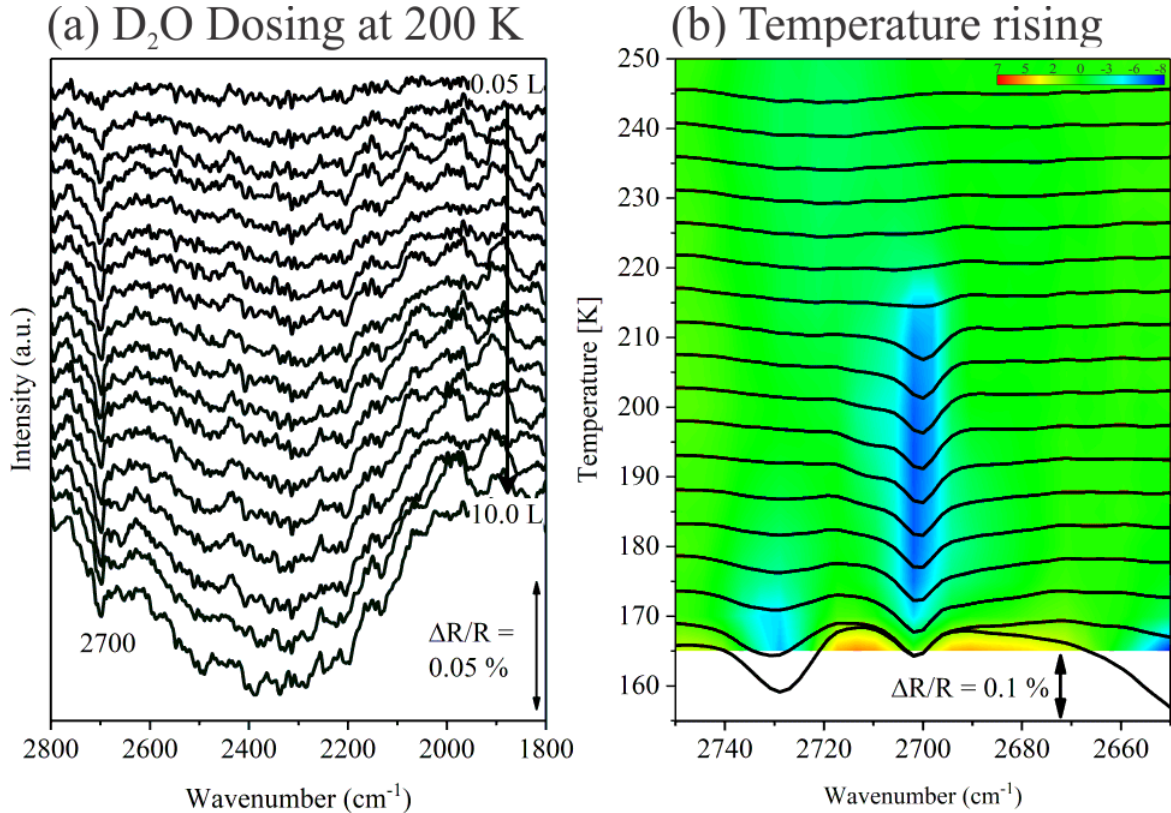


Figure 3.20: (a) D₂O coverage-dependent spectra (2800 cm^{-1} - 1800 cm^{-1}) from 0.05 L until 10 L of exposure. (b) TP-IRAS (2750 cm^{-1} - 2650 cm^{-1}) keeping a partial water pressure of 2×10^{-8} mbar, from 165 K until 250 K with 5 K of steps.

Probing the surface with D₂O molecule

Figure 3.20a shows the water coverage-dependent IRAS spectra for the region from 2800 cm^{-1} until 1800 cm^{-1} , where the sample was kept at 200 K to facilitate the observation of hydroxyl groups and avoid ice formation on the surface. The spectra shows a small peak at 2700 cm^{-1} , and this peak does not have its intensity increased with the doses, even when the large band centered at 2400 cm^{-1} starts appearing on the spectra. This 2400 cm^{-1} spectrum region is known to be related to the formation of ASW [76]. Adsorption experiments also were performed with the sample at temperatures of 300 K and 110 K. At room temperature (300 K), the water does not adsorb, and at low temperature (110 K), the large peak at 2730 cm^{-1} hid the small peak at 2700 cm^{-1} . Interesting, this

two peaks indicates that the surface dissociates the water by the defects sites. It occurs due to the presence of a limited amount of Mn^{3+} cations sites on the surface with missing oxygen atoms. These sites are expected to be particularly preferred since oxygen-rich termination surfaces are known to be unfavorable for water dissociation, as observed on the Cu_2O thin film [81].

Figure 3.20b shows the TP-IRAS spectra by raising the sample temperature from 165 K to 500 K, with steps of 5 K, keeping inside a partial water pressure of 2×10^{-8} mbar. However, the figure is shown until 250 K once the water has left the surface. Two peaks appear on the spectrum, where the first vanished before 175 K, and the second at 220 K. The 2730 cm^{-1} peak is assigned to be the intact water molecule weakly bounded on the surface, which will not remain on the surface after 175 K. Thus the 2700 cm^{-1} peak is attributed to the water dissociated on the oxygen vacancies. The hydroxyl group leaves the adsorption sites at 200 K in the $\text{MnO}(001)$ film, which indicates that this water bond is stronger on the Mn^{3+} cations of $\text{Mn}_3\text{O}_4(001)$ surface as compared to the Mn^{2+} species on $\text{MnO}(001)$ surface.

3.3.3 Conclusions

Mn_3O_4 thin films were grown on $\text{Au}(111)$ substrate, and its structure was probed by carbon monoxide (CO) and water (D_2O) molecules. This film is grown in the [001] direction with three domains rotated by 60° , and it is like the Mn_3O_4 bulk truncated without any reconstruction. The molecules adsorption experiments show a weak interaction indicating that the surface is oxygen-rich terminated. Where the rectangle ($5.76 \text{ \AA} \times 2.88 \text{ \AA}$) performed by the Mn^{3+} cations is the preferable termination due to the lattice mismatch, STM images [21] and DFT calculations [41]. The peak shift of CO adsorbed on the defects indicates that the bond is with a cation at octahedral coordination (Mn^{3+}). Therefore, the $\text{Mn}_3\text{O}_4(001)$ is terminated with Mn^{3+} and oxygen-rich, where the oxygen vacancies provide the water dissociation, until 220 K. This temperature is 20 K higher than the Mn^{2+} cations at octahedral sites in the MnO thin films (see section 3.2).

Conclusions

Well-ordered thin films of manganese oxide were grown on Au(111) substrate, where analyses of the electronic and lattice structures were presented. The MnO and the Mn₃O₄ were the films obtained, and both grow at [001] direction with domains rotated by 60° on the substrate surface. The MnO has the (1×1) structure regarding bulk structure, but for a determined temperature (650 K) and partial oxygen pressure (5×10^{-7} mbar), it presents the c(2×2) reconstruction. While (1×1) is approximated to a thin film that wets the substrate, the c(2×2) is approximated to the island. The Mn₃O₄ films present a (1×1) structure like a bulk truncated. It was performed a peak fit of XPS Mn 2p following the multiplet theory, and both materials present a complex spectrum composed of satellites, asymmetry peak, and Au 4p_{1/2} peak. The substrate contribution was calculated and removed for each spectrum, and the satellites were fixed. Therefore, the whole Mn 2p peak was fitted, and the multiplets components intensities were observed. Lastly, experiments with water (D₂O) and carbon monoxide (CO) were performed on the films. Both films show similar adsorption behavior, although they are distinct oxides.

First, advanced research was performed with the MnO thin films, and the fit of Mn 2p spectra evidences the low coordination cations on the film structure. The films could be fitted with three groups of multiplets presenting the intern, the terrace, and the edges components. Where each group of components comes from cations at different coordination, the intern-atoms have 6-nearest oxygen in the octahedral coordination, the terrace-atoms have ideally 5, and the edge-atoms have 4 or even less. Therefore, three distinct films were analyzed, which were labeled as thick (about 2 nm), thin (about 0.5 nm), and an island (about 0.5 nm). As expected, the thick film presents intense intern components, followed by the terrace and edge components. While the thin films, due to the low thickness, will present low-intense intern components. Hence, the intern components in the fit of thin and island films were despised. The thin film presents the terrace components as more intense than the edge components, while the island has the terrace- and edge components with about equal intensity. Therefore, the island film is expected to present more edge atoms than the thin film. These analyses presented show how a detailed XPS analysis can provide valuable information about the electronic structure of thin films and nanomaterials.

Experiments with D₂O show that the water is dissociated through the defects on the MnO surface, which modify the oxide surface. After the first water interaction, the surface changes its adsorption behavior, and the water is not dissociated. Although it is not the same as previous water adsorption, water dissociation is possible after the surface reaches 650 K. The adsorption behavior of clean film is recovered post-annealing (at 850 K) in partial oxygen pressure. These experiments show that the water performs corrosion on the

MnO surface, where the vacancies allow the water dissociation. However, once the water is removed from the surface, an oxygen vacancy is created, modifying the surface's electronic structure. The high temperature (over 600 K) can evaporate the defected layer, exhibiting the below layer that can dissociate the water again. It is a corroded surface, which can be ordered again with temperature and oxygen conditions in the post-annealing. The carbon monoxide presents a bind with the Mn^{2+} cations (at about 2174 cm^{-1}), which is blue-shifted due to the wall effect produced by its large band gap (3.5 eV). Identified adsorption sites at MnO terraces, edges, and interfaces with the substrate surface were identified. The interaction of CO with oxide is lesser than on the metal surface. The co-adsorption of CO and D_2O show that the sites that adsorb CO are the same that dissociate the water.

The surface structure and the chemical reactivity of Mn_3O_4 thin films were analyzed. This film presents a complex Mn 2p peak spectrum due to the mix of cations (Mn^{2+} and Mn^{3+}). Therefore, the fit is composed of the components of both cations, which explain the asymmetric peak. The film termination is the Mn^{3+} cations with the octahedral coordination completed, making this film oxygen-rich on the surface. The CO adsorbs on the oxygen vacancies, performing a bind with the cation (at about 2105 cm^{-1}). It is red-shifted due to the electron donation from the $3d$ orbital provided by the cation. This bind is stronger than the CO performed with the MnO film. It is not a surprise that this surface also dissociates the water only through the vacancies, but a corrosion effect is not observed, and its water-bind is stronger than the MnO surface.

Future Prospects: This thesis investigated the atomic-level structure and the chemical reactivity of manganese oxide thin films, particularly the MnO and the Mn_3O_4 . Therefore, it is possible to perform catalytic experiments on this oxides surfaces, considering their termination. Furthermore, once we can observe the changes in the XPS line shape due to the concentration of low-coordination atoms on the surface, it would be interesting to observe the change in the line shape after the molecules bind to the surface atoms. It is not expected to have much chemical reactivity of MnO. However, the same can not be said about the Mn_3O_4 . It is a material with a mix of cations, the Mn^{2+} and the Mn^{3+} at tetrahedral and octahedral sites, respectively. Therefore, some preliminary photo-catalyzed experiments showed the Mn_3O_4 as promising material. Furthermore, the nano-particles inserted on the surface to elucidate the electronic activities with the materials' adsorption are interesting in surface science.

Appendix A

Appendix

A.1 Master Thesis Summary

The Au(111) single-crystal was cleaned with cycles of sputtering and annealing as follow:

Cycle	Procedure	Time	Energy / Temperature
1	Sputtering	40 min	3 keV
	Annealing	20 min	400 K
2	Sputtering	30 min	2 keV
	Annealing	25 min	500 K
3	Sputtering	20 min	1 keV
	Annealing	30 min	650 K
4	Sputtering	10 min	800 eV
	Annealing	40 min	700 K

Table A.1: Parameters to perform the Sputtering and Annealing procedures to clean the Au(111) single-crystal.

After the Au(111) result at the diffraction pattern, where it is possible to observe the satellites from the herringbone structure, the oxide film was grown. The substrate was at room temperature during the growth, and the manganese pallets were evaporated on top of the substrate under partial oxygen pressure. A post-annealing was performed to promote film crystallization. Many manganese oxide thin films were grown onto Au(111) substrate, and the results were summarized in the Table A.2. In short, the range of oxygen pressure and thickness for the growth of well-ordered MnO(001) and Mn₃O₄(001) was determined.

Thickness	until $pO_2 = 5 \times 10^{-8}$ mbar	up to $pO_2 = 5 \times 10^{-7}$ mbar
Ultra-thin (from 0.5 nm until 2 nm)	(1×1) MnO(001)	(1×1)Mn ₃ O ₄ (001) or c(2×2)MnO(001)
Thin (up to 2 nm)	(1×1) or c(2×2) Mn ₃ O ₄ (001)	(1×1) Mn ₃ O ₄ (001)

Table A.2: Manganese oxide films dependence of film thickness and partial oxygen pressure.

Observe that the (1×1) and c(2×2) is with relation to the MnO(001) and Mn₃O₄(001) bulk structure. The film thickness was determined by Transmission Electron Microscopy (TEM). First, the film was grown onto Au(111), then protected with a capping layer, and then taken to the TEM equipment. Figure A.1 shows a STEM image of Mn/Mn₃O₄(001)/Au(111) interface, where it determined the rate of 1.5 Å/min. The thickness calibration was confirmed with Atomic Force Microscopy (AFM). A film of manganese metallic where grown onto a Si surface partially covered by a mask. It indicates a deposition rate of 1.7 Å/min. In this case, it is not considered the post-annealing and the size of the film unit cell.

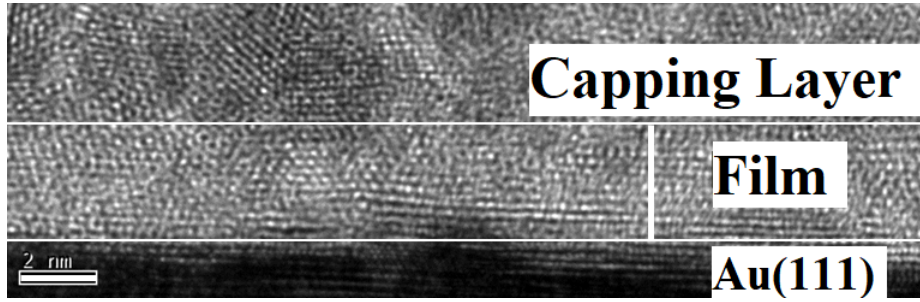


Figure A.1: The film thickness was determined by TEM image (performed by Prof. Dr. André Luiz Pinto). Interface of Mn on Mn₃O₄(001) film of 5 nm onto Au(111).

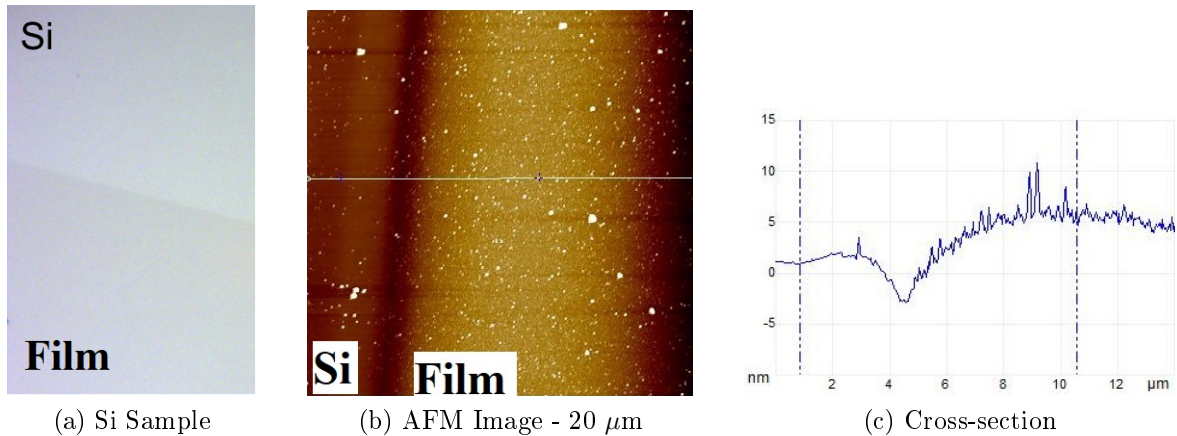


Figure A.2: Thickness calibration by Atomic Force Microscopy (AFM) image (image obtained by the master thesis). (a) Picture of Si sample (b) AFM Image - 20 μm and (c) cross-section.

A.2 Curriculum

Jade Barreto
(J. Barreto)

UNIVERSITY EDUCATION

2022 Ph.D. Brazilian Center for Research in Physics (CBPF)

Advisor: Prof. Dr. Fernando Stavale

Fellowship: CNPq, Brazil

2018 M.Sc. Brazilian Center for Research in Physics (CBPF)

Advisor: Prof. Dr. Fernando Stavale

Fellowship: CAPES, Brazil

2016 B.A. State University of Maringá (UEM)

Advisor: Prof. Dr. Ivair Aparecido dos Santos

SCIENCE POPULARIZATION

2019 - 2020 LABDID (Didactic Laboratory) at CBPF.

2016 - 2019 LABDIV (Scientific dissemination laboratory) at CBPF.

ORGANIZATION OF EVENTS

Barreto, J.; Macchiutti, C.; Peñafiel, M.; Melo, F., 2^o Scientific Academic Journey (JACa). 2020. (Congress) at CBPF.

Barreto, J.; Cavalcanti, E.; Mendes, L.; Melo, F., 1^o Scientific Academic Journey (JACa). 2019. (Congress) at CBPF.

PRESENTATIONS OF WORK

1. **BARRETO, J.;** CAETANO, R.; RAMOS, M. I.; ALÍ, A.; FÉLIX, G.; ANNESE, E.; NILIUS, N.; FREUND, H-J.; ARCHANJO, B. S.; ACHETE, C. A.; BAGUS, P. S.; STAVALE, F., Core-level binding energy shifts in MnO(001) thin films grown on Au(111). 2022.

XI Brazilian-German Workshops on Applied Surface Science. (Conference).

2. **BARRETO, J.;** STAVALE, F., Surface science studies on manganese oxide thin films grown on gold (111) Surface. 2018.

VI San Luis Conference on Surfaces, Interfaces and Catalysis. (Conference).

3. **BARRETO, J.;** STAVALE, F., Manganese oxide thin films grown on Au (111). 2017.

Brazilian Physical Society Meeting (ENFMC). (Congress).

Best Banner Award – Surface and Interface area. Brazilian Society of Physics (SBF).

PUBLICATIONS

1. **Barreto, J.**; Caetano, R.; Ramos, M. I.; Alí, A.; Félix, G.; Annese, E.; N. Nilius; H. J. Freund; Archanjo, B. S.; Achete, C. A.; Bagus, P. S.; Stavale, F., Core-level binding energy shifts between Interior, Terrace and Edge Atoms in MnO(001) thin films. *Surface Science*, v. 725, p. 122159, 2022.
DOI: 10.1016/j.susc.2022.122159.
2. Caetano, R.; Alí, A.; **Barreto, J.**; Félix, G.; Ramos, M. I.; Archanjo, B. S.; Achete, C. A.; Annese, E.; Stavale, F., The structure of Mn₃O₄(110) thin films. *Surface Science*, v. 720, p. 122062, 2022.
DOI: 10.1016/j.susc.2022.122062.
3. Annese, E.; Alí, A.; **Barreto, J.**; Félix, G.; Stavale, F., Unraveling hausmannite (Mn₃O₄) thin films surface structure by X ray linear dichroism. *Applied Surface Science*, v. 578, p. 151944, 2022.
DOI: 10.1016/j.apsusc.2021.151944.
4. Dos Santos, T.; Mancera, R. C.; Marcus, V. J.; Da Silva, A. F. M.; Furtado, I. O.; **Barreto, J.**; Stavale, F.; Archanjo, B. S.; De M. Carneiro, J. W.; Costa, L. T.; Ronconi, C. M., CO₂ and H₂ adsorption on 3D nitrogen-doped porous graphene: Experimental and theoretical studies. *Journal of CO₂ Utilization*, v. 48, p. 101517, 2021.
DOI: 10.1016/j.jcou.2021.101517.
5. Lima, L.; Caldas, L.; Alí, A.; **Barreto, J.**; Freitas, R.; Mazzarella, A.; Félix, G.; Carozo, V.; Stavale, F., Growth and Raman spectroscopy of ultrathin ZnO(0001) films on Ag(001). *Surface Science*, v. 704, p. 121748, 2021.
DOI: 10.1016/j.susc.2020.121748.
6. Annese, E.; Ali, A.; **Barreto, J.**; ; Stavale, F., Mn₃O₄ Thin Film on Cu(111): Modulating Electronic Structure through Film–Substrate Interaction. *The Journal of Physical Chemistry C*, v. 124, n. 28, p. 15162-15170, 2020.
DOI: 10.1021/acs.jpcc.0c01961.
7. Gonzalez Caronton, A.; Pinto, J.; **Barreto, J.**; Stavale, F.; Schmal, M., Statistical analysis of the catalytic synthesis of Vinyl acetate over Pd-Cu/ZrO₂ nanostructured based catalysts. *CATALYSIS TODAY*, v. 344, p. 108-117, 2020.
DOI: 10.1002/cctc.201801083.
8. Dos Santos, T.; Santos, E.; Dias, J.; **Barreto, J.**; Stavale, F.; Ronconi, C., Reduced graphene oxide as an excellent platform to produce a stable Brønsted acid catalyst for biodiesel production. *FUEL*, v. 256, p. 115793, 2019.
DOI: 10.1016/j.fuel.2019.115793.
9. Möller, C.; **Barreto, J.**; Stavale, F.; Nilius, N., Manganese Oxide Thin Films on Au(111): Growth Competition between MnO and Mn₃O₄, *Journal of Physical Chemistry C*, v. 123, n. 13, p. 7665-7672, 2018.
DOI: 10.1021/acs.jpcc.8b04176.

10. Möller, C.; **Barreto, J.**; Stavale, F.; Tissot, H.; Shaikhutdinov, S.; Freund, H.-J.; Nilius, N., Water Adsorption to Crystalline Cu₂O Thin Films – Structural and Vibrational Properties, *Journal of Physical Chemistry C*, v. 122, n. 4, p. 2195-2199, 2018.
DOI: 10.1021/acs.jpcc.7b10835.
11. Gonzalez Caronton, A.; Dille, J.; **Barreto, J.**; Stavale, F.; Pinto, J. C.; Schmal, M., Nanostructured Pd-Cu Catalysts Supported on Zr-Al and Zr-Ti for Synthesis of Vinyl Acetate. *ChemCatChem*, v.10, p. 1-15, 2018.
DOI: 10.1016/j.cattod.2018.10.034.

In preparation

Jade Barreto, Christoph Möller, Niklas Nilius, Heloise Tissot, Shamil Shaikhutdinov, Hans Joachim Freund, and Fernando L. Stavale, Chemical Reactivity of MnO(001) Thin Films Grown on Au(111).

Jade Barreto, Georg Fickenscher, Rubem Caetano, Maria I. Ramos, Astrid Alí, Guilherme Félix, Emilia Annese, Braulio Archanjo, Carlos A. Achete, Jörg Libuda and Fernando Stavale, Probing Surface Structure of Mn₃O₄(001) Film with CO and D₂O Adsorptions.

Bibliography

- [1] H. Lüth, *Solid surfaces, interfaces and thin films*, vol. 4. Springer, 2001.
- [2] C. Wöll, S. Chiang, R. Wilson, and P. Lippel, “Determination of atom positions at stacking-fault dislocations on Au(111) by scanning tunneling microscopy,” *Physical Review B*, vol. 39, no. 11, p. 7988, 1989.
- [3] L. Zhang, Z. Tang, S. Wang, D. Ding, M. Chen, and H. Wan, “Growth and vibrational properties of MnO_x thin films on Rh (111),” *Surface Science*, vol. 606, no. 19-20, pp. 1507–1511, 2012.
- [4] H. Nishimura, T. Tashiro, T. Fujitani, and J. Nakamura, “Surface structure of MnO/Rh (100) studied by scanning tunneling microscopy and low-energy electron diffraction,” *Journal of Vacuum Science & Technology A: Vacuum, Surfaces, and Films*, vol. 18, no. 4, pp. 1460–1463, 2000.
- [5] J. C. Védrine, “Heterogeneous catalysis on metal oxides,” *Catalysts*, vol. 7, no. 11, p. 341, 2017.
- [6] P. Saranraj, P. Sivasakthivelan, and M. Naveen, “Fermentation of fruit wine and its quality analysis: A review,” *Australian Journal of Science and Technology*, vol. 1, no. 2, pp. 85–97, 2017.
- [7] G. M. Walker and G. G. Stewart, “*Saccharomyces cerevisiae* in the production of fermented beverages,” *Beverages*, vol. 2, no. 4, p. 30, 2016.
- [8] G. A. Somorjai, “Surface science and catalysis,” *Science*, vol. 227, no. 4689, pp. 902–908, 1985.
- [9] F. Gao, S. M. McClure, Y. Cai, K. K. Gath, Y. Wang, M. Chen, Q. Guo, and D. W. Goodman, “Co oxidation trends on pt-group metals from ultrahigh vacuum to near atmospheric pressures: A combined in situ pm-iras and reaction kinetics study,” *Surface Science*, vol. 603, no. 1, pp. 65–70, 2009.
- [10] K. Anic, A. V. Bukhtiyarov, H. Li, C. Rameshan, and G. Rupprechter, “CO adsorption on reconstructed Ir (100) surfaces from uhv to mbar pressure: A LEED, TPD, and PM-IRAS study,” *The Journal of Physical Chemistry C*, vol. 120, no. 20, pp. 10838–10848, 2016.
- [11] G. Ertl, “Surface science and catalysis,” *Pure and Applied Chemistry*, vol. 52, no. 9, pp. 2051–2060, 1980.
- [12] H. H. Kung, *Transition metal oxides: surface chemistry and catalysis*, vol. 45. Elsevier, 1989.

- [13] H. Kuhlenbeck, S. Shaikhutdinov, and H.-J. Freund, “Well-ordered transition metal oxide layers in model catalysis—a series of case studies,” *Chemical reviews*, vol. 113, no. 6, pp. 3986–4034, 2013.
- [14] T. Yamashita and A. Vannice, “NO decomposition over Mn_2O_3 and Mn_3O_4 ,” *Journal of Catalysis*, vol. 163, no. 1, pp. 158–168, 1996.
- [15] S. C. Kim and W. G. Shim, “Catalytic combustion of vocs over a series of manganese oxide catalysts,” *Applied Catalysis B: Environmental*, vol. 98, no. 3-4, pp. 180–185, 2010.
- [16] C.-H. Kuo, W. Li, L. Pahalagedara, A. M. El-Sawy, D. Kriz, N. Genz, C. Guild, T. Ressler, S. L. Suib, and J. He, “Understanding the role of gold nanoparticles in enhancing the catalytic activity of manganese oxides in water oxidation reactions,” *Angewandte Chemie International Edition*, vol. 54, no. 8, pp. 2345–2350, 2015.
- [17] Y. Li, L. Lin, R. Mu, Y. Liu, R. Zhang, C. Wang, Y. Ning, Q. Fu, and X. Bao, “Activation of CO over ultrathin manganese oxide layers grown on Au(111),” *ACS Catalysis*, vol. 11, no. 2, pp. 849–857, 2021.
- [18] C. Hagendorf, S. Sachert, B. Bochmann, K. Kostov, and W. Widdra, “Growth, atomic structure, and vibrational properties of MnO ultrathin films on Pt(111),” *Physical Review B*, vol. 77, no. 7, p. 075406, 2008.
- [19] G. Rizzi, M. Petukhov, M. Sambri, R. Zanoni, L. Perriello, and G. Granozzi, “An X-ray photoelectron diffraction structural characterization of an epitaxial MnO ultrathin film on Pt(111),” *Surface science*, vol. 482, pp. 1474–1480, 2001.
- [20] F. Allegretti, C. Franchini, V. Bayer, M. Leitner, G. Parteder, B. Xu, A. Fleming, M. Ramsey, R. Podloucky, S. Surnev, *et al.*, “Epitaxial stabilization of MnO (111) overlayers on a Pd (100) surface,” *Physical Review B*, vol. 75, no. 22, p. 224120, 2007.
- [21] C. Möller, J. Barreto, F. Stavale, and N. Nilius, “Manganese oxide thin films on Au(111): Growth competition between MnO and Mn_3O_4 ,” *The Journal of Physical Chemistry C*, vol. 123, no. 13, pp. 7665–7672, 2018.
- [22] K. Meinel, M. Huth, H. Beyer, H. Neddermeyer, and W. Widdra, “Mosaic and facet structures of epitaxial MnO films on Au (110),” *Surface Science*, vol. 619, pp. 83–89, 2014.
- [23] A. K. Kundu and K. S. Menon, “Growth and characterization of ultrathin epitaxial MnO film on Ag (001),” *Journal of Crystal Growth*, vol. 446, pp. 85–91, 2016.
- [24] F. Müller, R. De Masi, D. Reinicke, P. Steiner, S. Hüfner, and K. Stöwe, “Epitaxial growth of MnO/Ag (001) films,” *Surface Science*, vol. 520, no. 3, pp. 158–172, 2002.
- [25] E. A. Soares, R. Paniago, V. de Carvalho, E. Lopes, G. Abreu, and H.-D. Pfannes, “Quantitative low-energy electron diffraction analysis of MnO (100) films grown on Ag (100),” *Physical Review B*, vol. 73, no. 3, p. 035419, 2006.

- [26] M. Nagel, I. Biswas, H. Peisert, and T. Chassé, “Interface properties and electronic structure of ultrathin manganese oxide films on Ag (001),” *Surface Science*, vol. 601, no. 18, pp. 4484–4487, 2007.
- [27] A. Chassé, C. Langheinrich, F. Müller, and S. Hüfner, “Growth and structure of thin MnO films on Ag (001) in dependence on film thickness,” *Surface Science*, vol. 602, no. 2, pp. 597–606, 2008.
- [28] E. Annese, A. Ali, J. Barreto, and F. Stavale, “Mn₃O₄ Thin Film on Cu (111): Modulating Electronic Structure through Film–Substrate Interaction,” *The Journal of Physical Chemistry C*, vol. 124, no. 28, pp. 15162–15170, 2020.
- [29] R. Caetano, A. Ali, J. Barreto, G. Félix, M. I. Ramos, B. S. Archanjo, C. A. Achete, E. Annese, and F. Stavale, “The structure of Mn₃O₄ (110) thin films,” *Surface Science*, p. 122062, 2022.
- [30] A. C. P. Ali, *Growth and doping of Mn_xO_y thin films on copper (111)*. PhD thesis, Centro Brasileiro de Pesquisas Físicas - CBPF, 2022.
- [31] J. Barreto, “Estudo do crescimento de filmes finos de MnO e Mn₃O₄ sobre substrato de Au(111),” Master’s thesis, Centro Brasileiro de Pesquisas Físicas, Rio de Janeiro, 2018. Portuguese.
- [32] P. S. Bagus and E. S. Ilton, “Effects of covalency on the p-shell photoemission of transition metals: MnO,” *Physical Review B*, vol. 73, no. 15, p. 155110, 2006.
- [33] R. Metselaar, R. Van Tol, and P. Piercy, “The electrical conductivity and thermoelectric power of Mn₃O₄ at high temperatures,” *Journal of Solid State Chemistry*, vol. 38, no. 3, pp. 335–341, 1981.
- [34] K. Momma and F. Izumi, “Vesta: a three-dimensional visualization system for electronic and structural analysis,” *Journal of Applied crystallography*, vol. 41, no. 3, pp. 653–658, 2008.
- [35] S. Lany, “Band-structure calculations for the 3 *d* transition metal oxides in GW,” *Physical Review B*, vol. 87, no. 8, p. 085112, 2013.
- [36] V. Bayer, C. Franchini, and R. Podloucky, “Ab initio study of the structural, electronic, and magnetic properties of MnO (100) and MnO (110),” *Physical Review B*, vol. 75, no. 3, p. 035404, 2007.
- [37] M. Towler, N. Allan, N. M. Harrison, V. Saunders, W. Mackrodt, and E. Apra, “Ab initio study of MnO and NiO,” *Physical Review B*, vol. 50, no. 8, p. 5041, 1994.
- [38] A. Chartier, P. D’Arco, R. Dovesi, and V. R. Saunders, “Ab initio hartree-fock investigation of the structural, electronic, and magnetic properties of Mn₃O₄,” *Physical Review B*, vol. 60, no. 20, p. 14042, 1999.
- [39] M. Fonin, Y. S. Dedkov, U. Rüdiger, and G. Güntherodt, “Growth and structure of Mn on Au (1 1 1) at room temperature,” *Surface science*, vol. 529, no. 3, pp. L275–L280, 2003.

- [40] A. K. Kundu, S. Barman, and K. S. Menon, “Stabilization of polar Mn_3O_4 (001) film on Ag (001): Interplay between kinetic and structural stability,” *Surface Science*, vol. 664, pp. 207–215, 2017.
- [41] C. Franchini, J. Zabloudil, R. Podloucky, F. Allegretti, F. Li, S. Surnev, and F. Netzer, “Interplay between magnetic, electronic, and vibrational effects in monolayer Mn_3O_4 grown on Pd(100),” *The Journal of chemical physics*, vol. 130, no. 12, p. 124707, 2009.
- [42] E. Annese, A. Alí, J. Barreto, G. Felix, and F. Stavale, “Unraveling hausmannite (mn_3o_4) thin films surface structure by x ray linear dichroism,” *Applied Surface Science*, vol. 578, p. 151944, 2022.
- [43] V. Bayer, R. Podloucky, C. Franchini, F. Allegretti, B. Xu, G. Parteder, M. G. Ramsey, S. Surnev, and F. P. Netzer, “Formation of Mn_3O_4 (001) on MnO (001): surface and interface structural stability,” *Physical Review B*, vol. 76, no. 16, p. 165428, 2007.
- [44] M. A. Vanhove, W. H. Weinberg, and C.-M. Chan, *Low-energy electron diffraction: experiment, theory and surface structure determination*, vol. 6. Springer Science & Business Media, 2012.
- [45] V. LEEDpat, “4.2, utility by KE Hermann (FHI) and MA Van Hove (HKBU),” *Berlin/Hong Kong*, 2014.
- [46] M. A. Van Hove, R. J. Koestner, P. C. Stair, J. P. Bibérian, L. L. Kesmodel, I. Bartoš, and G. A. Somorjai, “The surface reconstructions of the (100) crystal faces of iridium, platinum and gold. II. Structural determination by LEED intensity analysis,” *Surface Science*, vol. 103, no. 1, pp. 218–238, 1981.
- [47] S. Hüfner, *Photoelectron spectroscopy: principles and applications*. Springer Science & Business Media, 2013.
- [48] F. De Groot and A. Kotani, *Core level spectroscopy of solids*. CRC press, 2008.
- [49] P. S. Bagus, R. Broer, W. A. De Jong, W. Nieuwpoort, F. Parmigiani, and L. Sangaletti, “Atomic many-body effects for the p-shell photoelectron spectra of transition metals,” *Physical review letters*, vol. 84, no. 10, p. 2259, 2000.
- [50] V. Rakić and L. Damjanović, “Temperature-programmed desorption (tpd) methods,” in *Calorimetry and thermal methods in catalysis*, pp. 131–174, Springer, 2013.
- [51] J. W. Niemantsverdriet, *Spectroscopy in catalysis: an introduction*. John Wiley & Sons, 2007.
- [52] C. Badan, *Surface-structure dependence of water-related adsorbates on platinum*. PhD thesis, Leiden University, 2016.
- [53] J. L. Daschbach, Z. Dohnalek, S.-R. Liu, R. S. Smith, and B. D. Kay, “Water adsorption, desorption, and clustering on feo (111),” *The Journal of Physical Chemistry B*, vol. 109, no. 20, pp. 10362–10370, 2005.

- [54] E. Zaki, Z. Jakub, F. Mirabella, G. S. Parkinson, S. Shaikhutdinov, and H.-J. Freund, "Water ordering on the magnetite Fe_3O_4 surfaces," *The journal of physical chemistry letters*, vol. 10, no. 10, pp. 2487–2492, 2019.
- [55] K. A. Davis and D. W. Goodman, "Propene adsorption on clean and oxygen-covered au (111) and au (100) surfaces," *The Journal of Physical Chemistry B*, vol. 104, no. 35, pp. 8557–8562, 2000.
- [56] A. Buswell, K. Krebs, and W. Rodebush, "Infrared studies. iii. absorption bands of hydrogels between 2.5 and 3.5 μ ," *Journal of the American Chemical Society*, vol. 59, no. 12, pp. 2603–2605, 1937.
- [57] T. E. Madey and J. T. Yates Jr, *Vibrational spectroscopy of molecules on surfaces*, vol. 1. Springer Science & Business Media, 2013.
- [58] F. Hoffmann, "Infrared reflection-absorption spectroscopy of adsorbed molecules," *Surface Science Reports*, vol. 3, no. 2-3, p. 107, 1983.
- [59] A. A. Christy, Y. Ozaki, and V. G. Gregoriou, *Modern Fourier transform infrared spectroscopy*, vol. 2001. Elsevier, 2001.
- [60] N. Fairley, V. Fernandez, M. Richard-Plouet, C. Guillot-Deudon, J. Walton, E. Smith, D. Flahaut, M. Greiner, M. Biesinger, S. Tougaard, *et al.*, "Systematic and collaborative approach to problem solving using X-ray photoelectron spectroscopy," *Applied Surface Science Advances*, vol. 5, p. 100112, 2021.
- [61] S. Hüfner, G. K. Wertheim, D. N. E. Buchanan, and K. W. West, "Core line asymmetries in XPS-spectra of metals," *Physics Letters A*, vol. 46, no. 6, pp. 420–421, 1974.
- [62] S. Hüfner and G. K. Wertheim, "Core-line asymmetries in the x-ray-photoemission spectra of metals," *Physical Review B*, vol. 11, no. 2, pp. 678–683, 1975.
- [63] S. Tanuma, "Quases-imfp-tp2m inelastic electron mean free path calculated from the tanuma, powell, and penn tpp2m formula," *Surf Interface Anal*, vol. 21, p. 165, 1994.
- [64] P. S. Bagus, F. Illas, G. Pacchioni, and F. Parmigiani, "Mechanisms responsible for chemical shifts of core-level binding energies and their relationship to chemical bonding," *Journal of electron spectroscopy and related phenomena*, vol. 100, no. 1-3, pp. 215–236, 1999.
- [65] W. Egelhoff Jr, "Core-level binding-energy shifts at surfaces and in solids," *Surface Science Reports*, vol. 6, no. 6-8, pp. 253–415, 1987.
- [66] P. S. Bagus, C. J. Nelin, S. V. Levchenko, X. Zhao, E. M. Davis, H. Kuhlenbeck, and H.-J. Freund, "Surface core level BE shifts for CaO (100): insights into physical origins," *Physical Chemistry Chemical Physics*, vol. 21, no. 45, pp. 25431–25438, 2019.
- [67] C. J. Nelin, F. Uhl, V. Staemmler, P. S. Bagus, Y. Fujimori, M. Sterrer, H. Kuhlenbeck, and H.-J. Freund, "Surface core-level binding energy shifts for MgO (100)," *Physical Chemistry Chemical Physics*, vol. 16, no. 40, pp. 21953–21956, 2014.

- [68] S. Kowalczyk, L. Ley, F. McFeely, and D. Shirley, "Multiplet splitting of the manganese 2p and 3p levels in MnF_2 single crystals," *Physical Review B*, vol. 11, no. 4, p. 1721, 1975.
- [69] J. Van Elp, R. Potze, H. Eskes, R. Berger, and G. Sawatzky, "Electronic structure of MnO ," *Physical Review B*, vol. 44, no. 4, p. 1530, 1991.
- [70] F. Parmigiani and L. Sangaletti, "Fine structures in the x-ray photoemission spectra of MnO , FeO , CoO , and NiO single crystals," *Journal of electron spectroscopy and related phenomena*, vol. 98, pp. 287–302, 1999.
- [71] M. Oku, K. Wagatsuma, and T. Konishi, "Relation between 2p X-ray photoelectron and $\text{K}\alpha$ X-ray emission spectra of manganese and iron oxides," *Journal of electron spectroscopy and related phenomena*, vol. 98, pp. 277–285, 1999.
- [72] V. Di Castro and G. Polzonetti, "Xps study of MnO oxidation," *Journal of Electron Spectroscopy and Related Phenomena*, vol. 48, no. 1, pp. 117–123, 1989.
- [73] M. Oku, K. Hirokawa, and S. Ikeda, "X-ray photoelectron spectroscopy of manganese—oxygen systems," *Journal of Electron Spectroscopy and Related Phenomena*, vol. 7, no. 5, pp. 465–473, 1975.
- [74] M. Langell, C. Hutchings, G. Carson, and M. Nassir, "High resolution electron energy loss spectroscopy of MnO (100) and oxidized MnO (100)," *Journal of Vacuum Science & Technology A: Vacuum, Surfaces, and Films*, vol. 14, no. 3, pp. 1656–1661, 1996.
- [75] M. A. Henderson, "The interaction of water with solid surfaces: fundamental aspects revisited," *Surface Science Reports*, vol. 46, no. 1-8, pp. 1–308, 2002.
- [76] P. A. Thiel and T. E. Madey, "The interaction of water with solid surfaces: Fundamental aspects," *Surface Science Reports*, vol. 7, no. 6-8, pp. 211–385, 1987.
- [77] C. Stampfl, M. V. Ganduglia-Pirovano, K. Reuter, and M. Scheffler, "Catalysis and corrosion: the theoretical surface-science context," *Surface Science*, vol. 500, no. 1-3, pp. 368–394, 2002.
- [78] U. Diebold, "Perspective: A controversial benchmark system for water-oxide interfaces: $\text{H}_2\text{O}/\text{TiO}_2(110)$," *Journal of Chemical Physics*, 2017.
- [79] N. G. Petrik and G. A. Kimmel, "Reaction kinetics of water molecules with oxygen vacancies on rutile $\text{TiO}_2(110)$," *Journal of Physical Chemistry C*, vol. 119, no. 40, pp. 23059–23067, 2015.
- [80] X. Yu, P. Schwarz, A. Nefedov, B. Meyer, Y. Wang, and C. Wöll, "Structural evolution of water on $\text{ZnO}(100)$: From isolated monomers via anisotropic H-bonded 2d and 3d structures to isotropic multilayers," *Angewandte Chemie*, vol. 131, no. 49, pp. 17915–17921, 2019.
- [81] C. Möller, J. Barreto, F. Stavale, H. Tissot, S. Shaikhutdinov, H.-J. Freund, and N. Nilius, "Water adsorption to crystalline Cu_2O thin films: Structural and vibrational properties," *The Journal of Physical Chemistry C*, vol. 122, no. 4, pp. 2195–2199, 2018.

- [82] M. Schwarz, S. Mohr, C. Hohner, K. Werner, T. Xu, and J. Libuda, "Water on atomically-defined cobalt oxide surfaces studied by temperature-programmed ir reflection absorption spectroscopy and steady state isotopic exchange," *Journal of Physical Chemistry C*, vol. 123, no. 13, pp. 7673–7681, 2019.
- [83] G. Yan, T. Wähler, R. Schuster, M. Schwarz, C. Hohner, K. Werner, J. Libuda, and P. Sautet, "Water on oxide surfaces: A triaqua surface coordination complex on Co_3O_4 (111)," *Journal of the American Chemical Society*, vol. 141, no. 14, pp. 5623–5627, 2019.
- [84] C. Arble, X. Tong, L. Giordano, A. M. Ferrari, and J. T. Newberg, "Water dissociation on $\text{MnO}(1\times 1)/\text{Ag}(100)$," *Physical Chemistry Chemical Physics*, vol. 18, no. 36, pp. 25355–25363, 2016.
- [85] X. Li, J. Paier, J. Sauer, F. Mirabella, E. Zaki, F. Ivars-Barceló, S. Shaikhutdinov, and H.-J. Freund, "Surface termination of $\text{Fe}_3\text{O}_4(111)$ films studied by CO adsorption revisited," *The Journal of Physical Chemistry B*, vol. 122, no. 2, pp. 527–533, 2018.
- [86] C. Lemire, R. Meyer, V. E. Henrich, S. Shaikhutdinov, and H.-J. Freund, "The surface structure of $\text{Fe}_3\text{O}_4(111)$ films as studied by CO adsorption," *Surface science*, vol. 572, no. 1, pp. 103–114, 2004.
- [87] P. Ferstl, S. Mehl, M. A. Arman, M. Schuler, A. Toghan, B. Laszlo, Y. Lykhach, O. Brummel, E. Lundgren, J. Knudsen, *et al.*, "Adsorption and activation of CO on $\text{Co}_3\text{O}_4(111)$ thin films," *The Journal of Physical Chemistry C*, vol. 119, no. 29, pp. 16688–16699, 2015.
- [88] H. Jian-Wei, C. A. Estrada, J. S. Corneille, W. Ming-Cheng, and D. W. Goodman, "CO adsorption on ultrathin MgO films grown on a Mo(100) surface: an IRAS study," *Surface science*, vol. 261, no. 1-3, pp. 164–170, 1992.
- [89] E. Guglielminotti, S. Coluccia, E. Garrone, L. Cerruti, and A. Zecchina, "Infrared study of CO adsorption on magnesium oxide," *Journal of the Chemical Society, Faraday Transactions 1: Physical Chemistry in Condensed Phases*, vol. 75, pp. 96–108, 1979.
- [90] Y. Martynova, M. Soldemo, J. Weissenrieder, S. Sachert, S. Polzin, W. Widdra, S. Shaikhutdinov, and H.-J. Freund, "CO oxidation over monolayer manganese oxide films on Pt(111)," *Catalysis letters*, vol. 143, no. 11, pp. 1108–1115, 2013.
- [91] H. Nishimura, J. Ogawa, and J. Nakamura, "Adsorption of CO on an $\text{MnO}/\text{Rh}(100)$ model catalyst," *Surface science*, vol. 482, pp. 215–219, 2001.
- [92] A. Michaelides, V. A. Ranea, P. L. de Andres, and D. A. King, "General Model for Water Monomer Adsorption on Close-Packed Transition and Noble Metal Surfaces," *Physical Review Letters*, vol. 90, no. 21, p. 4, 2003.
- [93] A. A. Phatak, W. N. Delgass, F. H. Ribeiro, and W. F. Schneider, "Density Functional Theory Comparison of Water Dissociation Steps on Cu, Au, Ni, Pd, and Pt," *The Journal of Physical Chemistry C*, vol. 113, no. 17, pp. 7269–7276, 2009.

- [94] J. Carrasco, J. Klimeš, and A. Michaelides, “The role of van der Waals forces in water adsorption on metals,” *The Journal of Chemical Physics*, vol. 138, no. 2, p. 024708, 2013.
- [95] A. Huzayyin, J. H. Chang, K. Lian, and F. Dawson, “Interaction of Water Molecule with Au(111) and Au(110) Surfaces under the Influence of an External Electric Field,” *The Journal of Physical Chemistry C*, vol. 118, no. 7, pp. 3459–3470, 2014.
- [96] M. Morgenstern, T. Michely, and G. Comsa, “Anisotropy in the adsorption of H₂O at low coordination sites on Pt(111),” *Physical Review Letters*, vol. 77, no. 4, pp. 703–706, 1996.
- [97] K. Morgenstern, “Scanning tunnelling microscopy investigation of water in sub-monolayer coverage on Ag(111),” *Surface Science*, vol. 504, pp. 293–300, 2002.
- [98] T. Mitsui, M. K. Rose, E. Fomin, D. F. Ogletree, and M. Salmeron, “Water diffusion and clustering on Pd(111),” *Science*, vol. 297, no. 5588, pp. 1850–1852, 2002.
- [99] H. Gawronski, K. Morgenstern, and K. H. Rieder, “Electronic excitation of ice monomers on Au(111) by scanning tunneling microscopy: Vibrational spectra and induced processes,” *European Physical Journal D*, vol. 35, no. 2, pp. 349–353, 2005.
- [100] N. Ikemiya and A. A. Gewirth, “Initial stages of water adsorption on Au surfaces,” *Journal of the American Chemical Society*, vol. 119, no. 41, pp. 9919–9920, 1997.
- [101] R. L. Wells and T. Fort, “Adsorption of water on clean gold by measurement of work function changes,” *Surface Science*, vol. 32, no. 3, pp. 554–560, 1972.
- [102] B. Rowland and J. P. Devlin, “Spectra of dangling OH groups at ice cluster surfaces and within pores of amorphous ice,” *The Journal of Chemical Physics*, vol. 94, no. 1, pp. 812–813, 1991.
- [103] D. Stacchiola, J. B. Park, P. Liu, S. Ma, F. Yang, D. E. Starr, E. Muller, P. Sutter, and J. Hrbek, “Water nucleation on gold: Existence of a unique double bilayer,” *Journal of Physical Chemistry C*, vol. 113, no. 34, pp. 15102–15105, 2009.
- [104] F. Mirabella, E. Zaki, F. Ivars-Barceló, X. Li, J. Paier, J. Sauer, S. Shaikhutdinov, and H. J. Freund, “Cooperative formation of long-range ordering in water ad-layers on Fe₃O₄ surfaces,” *Angewandte Chemie - International Edition*, vol. 57, no. 5, pp. 1409–1413, 2018.
- [105] X. Yu, P. Schwarz, A. Nefedov, B. Meyer, Y. Wang, and C. Wöll, “Structural evolution of water on ZnO(100): From isolated monomers via anisotropic h-bonded 2d and 3d structures to isotropic multilayers,” *Angewandte Chemie*, vol. 131, no. 49, pp. 17915–17921, 2019.
- [106] G. G. Kebede, P. D. Mitev, W. J. Briels, and K. Hermansson, “Red-shifting and blue-shifting oh groups on metal oxide surfaces-towards a unified picture,” *Physical chemistry chemical physics*, vol. 20, no. 18, pp. 12678–12687, 2018.
- [107] V. Buch and J. P. Devlin, “Spectra of dangling oh bonds in amorphous ice: Assignment to 2- and 3-coordinated surface molecules,” *The Journal of chemical physics*, vol. 94, no. 5, pp. 4091–4092, 1991.

- [108] P.-A. Chollet, "Determination by infrared absorption of the orientation of molecules in monomolecular layers," *Thin Solid Films*, vol. 52, no. 3, pp. 343–360, 1978.
- [109] Y. Lilach, I. Danziger, and M. Asscher, "Second order isothermal desorption kinetics," *Catalysis letters*, vol. 76, no. 1, pp. 35–39, 2001.
- [110] G. Herzberg, "Molecular spectra and molecular structure. vol. 1: Spectra of diatomic molecules," *New York: Van Nostrand Reinhold*, 1950.
- [111] G. Pacchioni, G. Cogliandro, and P. S. Bagus, "Characterization of oxide surfaces by infrared spectroscopy of adsorbed carbon monoxide: a theoretical investigation of the frequency shift of co on mgo and nio," *Surface science*, vol. 255, no. 3, pp. 344–354, 1991.
- [112] A. Soon, T. Söhnle, and H. Idriss, "Plane-wave pseudopotential density functional theory periodic slab calculations of co adsorption on cu₂o (111) surface," *Surface science*, vol. 579, no. 2-3, pp. 131–140, 2005.
- [113] E. E. Platero, D. Scarano, G. Spoto, and A. Zecchina, "Dipole coupling and chemical shifts of CO and NO adsorbed on oxides and halides with rock-salt structure," *Faraday discussions of the Chemical Society*, vol. 80, pp. 183–193, 1985.
- [114] J. Kim, E. Samano, and B. E. Koel, "Co adsorption and reaction on clean and oxygen-covered au (211) surfaces," *The Journal of Physical Chemistry B*, vol. 110, no. 35, pp. 17512–17517, 2006.
- [115] L. Piccolo, D. Loffreda, F. C. S. Aires, C. Deranlot, Y. Jugnet, P. Sautet, and J. Bertolini, "The adsorption of co on au (111) at elevated pressures studied by stm, raics and dft calculations," *Surface science*, vol. 566, pp. 995–1000, 2004.
- [116] M. I. Zaki and H. Knözinger, "Characterization of oxide surfaces by adsorption of carbon monoxide—a low temperature infrared spectroscopy study," *Spectrochimica Acta Part A: Molecular Spectroscopy*, vol. 43, no. 12, pp. 1455–1459, 1987.
- [117] M. A. Stranick, "Mn₂o₃ by xps," *Surface Science Spectra*, vol. 6, no. 1, pp. 39–46, 1999.